eman ta zabal zazu

Universidad del País Vasco
Euskal Herriko Unibertsitatea

Spin and charge control of single molecules for atomic scale quantum coherence

Dissertation to attain the title “Doctor of Philosophy”
by
Leonard Edens

Supervised by Prof. Dr. José Ignacio Pascual Chico

Donostia-San Sebastián on March 12, 2025

This thesis was conducted at the research centre CIC nanoGUNE BRTA under the tutorship of Prof. Dr. José María Pitarke de la Torre.

All text and figures within were produced solely by the author.

Abstract

The spin degree of freedom in individual molecules has been proposed as a platform for atomic-scale quantum computing. The required unpaired electrons are often encountered in metal-organic compounds, but also in fully organic species such as nanographenes, which can host radical states. Considerable progress has been made recently in the catalytic synthesis of such structures on noble metals, and the *a priori* design of spin states through tailor-made geometries. However, the quantum coherence of molecular spins is generally diminished when interfaced with conductive surfaces due to the Kondo effect, and magnetism can even be destroyed entirely by charge transfer. In this thesis, we explore several rationales for how the gas-phase electronic properties of isolated molecular spins can be protected from, or even enhanced by these interactions. To this end, we employ low-temperature scanning probe spectroscopy to study a several families of molecular spins supported by functional surfaces at the intramolecular scale.

As an archetypal example of π-radical system, we investigate chiral graphene nanoribbons. When spaced by a thin insulating MgO layer from a metallic substrate, a variety of electronically decoupled but highly negative charge states are realized, whose ionicity and spin state are tuned purely by geometry. The underlying mechanism, deriving from charge quantization and intramolecular Coulomb repulsion, also imbues the much smaller closed-shell phthalocyanine with a net spin. Conversely, a related organometallic molecule is found immune to charge transfer by virtue of specialized ligands. The chemical self-decoupling approach also effectively protects the spin state of vanadocene from magnetic scattering, even when in directly adsorbed on a metal.

We also investigate how charge neutrality in nanographene can be restored on metallic surfaces. The $GdAu_2$, a 2D ferromagnet, support on-surface synthesis of chiral graphene nanoribbons. Their pristine half-filled molecular state manifests in the emergence of two characteristic symmetry-protected topological zero modes with local moments. Employing a single nickelocene molecule as a spin probe, we map the substrate's exchange field atom-by-atom. This additional coupling favours alignment of π-radicals, forming a triplet state stabilized against spin flips with conduction electrons. By molecular manipulation across the substrate's moiré superstructure, we demonstrate that individual moments can also be reversibly quenched by accumulating a single electron.

To probe the quantum coherence of potential molecular spin, we augment a scanning tunnelling microscope with radiofrequency capability. As a benchmark, we perform electron spin resonance of an individual atom and obtain state-of-the-art energy resolution. In a theoretical study, we detail how a double-frequency driving scheme can coherently address the hyperfine structure between electronic and nuclear spins in single molecules.

In this work, several surface-adsorbed molecular spin qubit candidates are realized by rational choice of both chemical structure and supporting surface. The results motivate a hybrid approach for engineering single-molecule devices, wherein the microscopic interactions with electrodes are explicitly taken into account.

Resumen

El espín de moléculas individuales es considerado una plataforma ideal de computación cuántica a escala atómica. Electrones desapareados, que generan el espín, se encuentran en compuestos organometálicos, o también en hidrocarburos como el nanografeno, que puede formar configuraciones radicales. Se ha demostrado recientemente que estas estructuras se pueden sintetizar con precisión atómica en superficies metálicas, con propriedades electrónicas dado por la geometría. No obstante, la coherencia cuántica de espines moleculares soportados por una superficie conductiva se ve impactada por el efecto Kondo; además, el magnetismo puede ser sofocado íntegramente debido a transferencia de carga. En esta tesis, exploramos métodos que protegen espínes moleculares de dichas interacciones, o que las aprovechan. Para ello, exploramos distintas familias químicas sobre superficies funcionales con microscopia de sondas al nivel intramolecular.

Como sistema emblemático del magnetismo π, investigamos nanocintas de grafeno. Observams que capas atómicas del aislante MgO desacoplan el estado molecular del substrato metálico, y realizan configuraciones altamente iónicas con momentos magnéticos que se controlan por su geometría y tamaño. El origen de este fenómeno surge de la competición entre carga integral y repulsión electrostática intramolecular y dota ftalocianina, debido a su pequeñez, con un momento magnético. Funcionalizada con ligandos distintos, la misma clase de moléculas también soporta neutralidad eléctrica en MgO. El mismo efecto de autodesacople químico protege el espín de vanadoceno de *scattering* magnético en superficies metálicas.

Desarrollamos un enfoque alternativo a prevenir la transferencia de carga en nanografeno: la síntesis directa en capas de la aleación ferromagnética $GdAu_2$. En nanocintas quirales, resulta en una configuración neutra con estados de energía zero en sus bordes protegidos topológicamente por la simetría. Además, estudiamos la interacción de canje con el substrato atomicamente mediante una molécula de niqueloceno ligado con la punta. El acoplamiento al substrato estabiliza la alineación positiva entre los espines π, formando un estado triplete, y domina el efecto Kondo. Desplazando las nanocintas lateralmente, revelamos que la estructura moiré de la superficie puede donar electrones a los estados topológicos de manera reversible, pareando con radicales individuales, lo que modifica su magnetismo.

Para obtener acceso a la coherencia cuántica de espines moleculares, aumentamos el rango de operación del microscopio hasta el régimen de microondas. Nos permite detectar resonancia magnética en un sistema modelo: el espín electrónico de un átomo de titanio, que exhibe una resolución energética suprema. Investigamos teóricamente un esquema de resonancia para sistemas electro-nucleares que sondea sus interacciones intrínsecas aprovechando de dos frecuencias aplicadas.

En el contexto de este trabajo, encontramos varios espínes moleculares que muestran promesa de coherencia cuántica eligiendo tanto sus estructuras químicas que las superficies. Los resultados motivan la consideración de interacciones microscópicas con electrodos en la realización de dispositivos cuánticos basados en moléculas individuales.

Acknowledgements

First, I'd like to thank my *Doktorvater* Prof. Nacho Pascual for introducing me to this wonderful field, always having an answer to my questions, and for consistently sharing interest in what I've been up to.

I also want to emphasize the support and encouragement my colleagues have given me during the last four years; among others, all current and former members of the Quantum Probe Microscopy group at nanoGUNE, whose teamwork has always kept our labs running. I'd especially like to thank Dr. Danilo Longo, for the countless (but rewarding) hours of epitaxy and iron atom manipulation, and Dr. Stefano Trivini, Katerina Vaxevani, Dr. Jon Ortuzar and Dr. Dongfei Wang for the enthusiastic participation during the upgrades and repairs of "Berlino".

I've had the great privilege of extended research stays in several world-class groups working with scanning tunnelling microscopy. I'd like to thank the postdocs and PIs, and all other members, for welcoming me into their laboratories and sharing their expertise: Prof. Dr. David Serrate and Dr. Amelia Domínguez-Celorrio at INMA in Zaragoza, Prof. Dr. Andreas Heinrich and Prof. Dr. Yujeong Bae at QNS in Seoul, Prof. Dr. Harald Brune and Dr. Johannes Schwenk at EPFL in Lausanne, and Prof. Sander Otte and Dr. Cristina Mier at TU Delft.

Contents

Figures

Acronyms

AFM atomic force microscope
CC constant-current
CH constant-height
chGNR chiral graphene nanoribbon
Cp cyclopentadienyl
CW-ENDOR continuous wave ENDOR
DC direct current/voltage
DFT density functional theory
DOS density of states
ENDOR electron nuclear double resonance
ESR electron spin resonance
ESR-STM electron spin resonance STM
FWHM full width at half maximum
GNR graphene nanoribbon
HOMO highest occupied molecular orbital
IETS inelastic electron tunnelling spectroscopy
KPFM Kelvin probe force microscopy
LCPD local contact potential difference
LDOS local density of states
LT-STM low temperature STM
LUMO lowest unoccupied molecular orbital
MAE magnetic anisotropy energy
MFH mean-field Hubbard model
nc-AFM non-contact AFM
NIR negative ion resonance
NMR nuclear magnetic resonance
OSS on-surface synthesis
Pc phthalocyanine
PIR positive ion resonance
PU precursor unit
QPC quantum point contact
QW quantum well
RF radio frequency
SOMO singly occupied molecular orbital
SP-STM spin-polarized STM
SPTES symmetry-protected topological end state
STM scanning tunnelling microscope
STS scanning tunnelling spectroscopy
SUMO singly unoccupied molecular orbital
TF transfer function
TPP tetraphenylporphyrin
UHV ultra-high vacuum

Introduction

The recent advent of commercialized quantum computing is believed to be the beginning of an exponential race to integrate and miniaturize quantum devices to boost performance.[1–4] The logical unit of a quantum processor, the qubit, consists of two quantum states that can be controllably superposed. Much like in classical semiconductor-based computing, the laws of physics can impose limits on its dimensions. For instance, the currently leading architecture for qubits, the superconducting transmon, relies on circuit elements on the millimetre scale whose size is constrained by the operating frequency of its two-level system.

Here, we will anticipate the far end of qubit miniaturization - the atomic limit - where quantization arises naturally. Several qubit architectures are already based on single atoms, but suffer from similar scalability issues. Meanwhile, an entirely new qubit architecture has been proposed: single molecules.[5–7] Metal-organic compounds have been shown to exhibit quantized electronic spin states defined by their structure, which can be directly addressed via magnetic resonance.[8] By virtue of chemical synthesis, identical replicas of such molecular qubits can be created in arbitrary quantities. Many even naturally arrange into ordered patterns when condensed, aiding integration and entanglement. Organic coordination offers great tunability of the spin state: ligands are engineered to tune decoupling from the environment, self-assembly properties, level structure, and electrical addressability.[9] Additionally, a single such self-contained unit can host a higher electronic spin, or even nuclear spins, which gives a quantum multi-level system.[10]

Much of current research investigates ensembles of molecular spin qubits, in the form of crystals, by electron spin resonance. Recent experimental breakthroughs have made it possible to apply this technique also to single molecules by leveraging the extreme spatial resolution of the scanning tunnelling microscope.[11–14] The key property of any qubit is the duration for which a prepared quantum state can remain in superposition. For a molecular spin, this is given by the magnetic relaxation time T_1 and decoherence time T_2, which are critically determined by the degree of coupling to its environment. For scanning tunnelling microscopy, molecules need to be deposited onto a conductive surface. Here, no longer protected by a crystalline matrix, the spin of a single molecule is vulnerable to several interactions. These can be magnetic scattering with conduction electrons, which makes up T_1 and also constrains T_2. Another adverse effect is charge transfer, by which exchange of electrons between the substrate and the molecule can quench its spin.

In this thesis, we will cover several techniques to mitigate molecule-surface interactions by engineering both the surface, and the molecule. We will also consider ways in which these effects give new functionality, and in doing so, realize several potential single molecule spin qubits fully supported by surfaces. We will study three types of molecules: nanographene, which host π-radical states, metal-organic compounds, with transition metal moments, and phthalocyanine, a nonmagnetic compound. In Chapter 3, we will explore how ferromagnetic layers of $GdAu_2$ can support charge neutrality of nanographene and induce new magnetic ground states. We will then decouple single molecules from conduction electron scattering by placing them on insulating layers in Chapter 4, which also enables anionic spin states in otherwise closed-shell molecules. Finally, we will implement a state-of-the-art setup capable of performing spectroscopy and quantum-coherent manipulation of a single molecular spin, and theoretically model a resonance scheme that can enhance signal in coupled electron-nuclear systems in Chapter 5.

Chapter 1

Physical concepts

In the following section, we will outline the concept of magnetism in the context of individual atoms and molecules. Section 1.1.2 describes the emergence of π-radicals in graphene nanostructures. The electrostatic and magnetic interactions of spins adsorbed on surfaces are introduced in Section 1.2. Finally, Section 1.3 covers the microscopy methods that will be employed in the following experiments to spectroscopically probe at the intramolecular scale.

1.1 Magnetic moments in single atoms and molecules

1.1.1 Adatoms and metal-organic complexes

Many atoms and metal-organic complexes possess more than one unpaired electron spin, represented by a spin quantum number $S > 1/2$. The spin vector $\mathbf{S}$ is quantized into $2S + 1$ orientations as shown in Figure 1.1a. Heisenberg's uncertainty principle allows determining its projection only along one coordinate, termed the quantization axis, here $\mathbf{z}$. For an isotropic spin in the absence of magnetic fields, the the spin levels are energy-degenerate.[15] However, when subject to spin-orbit coupling, anisotropies arise and $\mathbf{S}$ gains a preferential orientation. This occurs because the spin-orbit interaction in heavy elements (i.e. transition and rare earth metals) can couple the electronic spin to a low-symmetry electrostatic environment. In isolated magnetic atoms in ionic crystals, this is constituted by the nearest lattice sites and known as the crystal field. In metal-organic molecules, the environment consists of the functional groups chemically bound to the central magnetic ion, and is termed the ligand field. The fields' effect is to lift the degeneracy of spin-carrying atomic states by hybridizing them with the environment, resulting in orbitals of lower symmetry.[8,16,17] If this perturbation is large compared to the spin-orbit coupling, the orbital angular momentum is said to be quenched such that $\langle \hat{L_z} \rangle = 0$ and we can define an effective spin (henceforth just

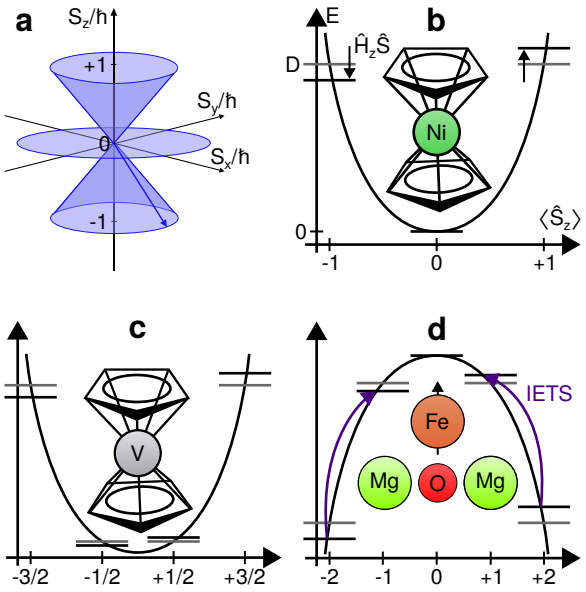

Figure 1.1: Electronic spin in individual molecules and atoms with magnetic anisotropy. **(a)** The quantization of the $S = 1$ spin vector. **(b)** Eigenvalues of the spin Hamiltonian for nickelocene ($NiCp_2$), which has $S = 1$ and an easy-plane anisotropy ($D > 0$). We plot energy over $\langle\hat{S}_z\rangle$. The Zeeman effect shifts the outer levels from the grey to the black positions. **(c)** The same in vanadocene (VCp_2), where $S = 3/2$. **(d)** Fe/MgO with $S = 2$ and easy-axis anisotropy $D < 0$. Inelastic electron tunnelling spectroscopy (IETS) probes the transitions shown with arrows.

S), with generally non-degenerate sublevels m_s. The Hamiltonian[18] of a single electronic effective spin is defined as

$$\mathcal{H} = \mathcal{H}_\mathrm{Z} + \mathcal{H}_\mathrm{D} \tag{1.1}$$

where the first term represents the Zeemann effect on the effective spin due to an external magnetic field **B**, and the second the zero-field anisotropy splittings. For the former, we have

$$\mathcal{H}_\mathrm{Z} = \mu_\mathrm{B}\mathbf{B}^\mathrm{T}\mathbf{g}\hat{\mathbf{S}} = g_\perp\mu_\mathrm{B}B_x\hat{S}_x + g_\perp\mu_\mathrm{B}B_y\hat{S}_y + g_\parallel\mu_\mathrm{B}B_z\hat{S}_z \tag{1.2}$$

where **g** is the 3×3 tensor of g-factors that reflects the energy cost of aligning the spin towards a certain direction due to the residual spin-orbit interaction. For uniaxially symmetric environments, as considered here, its principal values are $(g_\perp, g_\perp, g_\parallel)$. Importantly, these g-factors differ significantly from the free-electron value, g_e. Its effect is to split the $2S + 1$ spin levels according to the sign and magnitude of $\langle\hat{S}_z\rangle$, and the orientation of **B** with respect to the symmetry axis of **g**. The second term is written as

$$\mathcal{H}_\mathrm{D} = \hat{\mathbf{S}}^\mathrm{T}\mathbf{D}\hat{\mathbf{S}} = E(\hat{S}_x^2 - \hat{S}_y^2) + D\hat{S}_z^2 \tag{1.3}$$

where we have taken **D** to be uniaxial, with principal values $(E, -E, D)$ where $E < D$. If D is positive and E negligible, **S** is energetically favoured to form a large angle with z. This is called easy-plane anisotropy. If $D < 0$, one has an easy-axis anisotropy, which orients the magnetic moment along z in the absence of field. The transverse anisotropy E is small in all spins investigated here.

Spin anisotropy is found in the family of metallocenes. In these transition-metal sandwich compounds, a magnetic center is encased between two weakly bound cyclopentadienyl (Cp) ligands. Depending on the metal ion, different spin states can be found: $S = 0$ for $FeCp_2$, $S = 1/2$ for $CoCp_2$, $S = 1$ for $NiCp_2$ and $S = 3/2$ for VCp_2.[19] In Figure 1.1, we sketch

the spin Hamiltonian's eigenenergies for the two metallocenes studied in this thesis, $NiCp_2$ and VCp_2. The states are plotted with and without the Zeeman effect $\mathcal{H}_Z$, here acting along z. These two molecules exhibit easy-plane anisotropy ($D > 0$), such that the lowest-lying spin levels are $m_s = 0$ and $m_s = \pm 1/2$, respectively. They are separated from their respective excited states ($m_s = \pm 1$ and $m_s = \pm 3/2$) by the magnetic anisotropy energy (MAE), amounting to D and $2D$, respectively. The anisotropy axis derives from the linear arrangement of the metal-Cp bond.[20–22]

Single atoms can display similar effects when adsorbed on surfaces. Here, the intrinsically broken symmetry of such an adatom's binding site can give MAE of several tens of meV.[23–26] In this work we utilize Fe ($S = 2$) bound to the oxygen site of the insulator MgO,[27] and Ti adsorbed on the same surface, which possesses $S = 1/2$.[28] In the case of Fe, a large spin and easy-axis anisotropy stabilizes a magnetization along $\mathbf{z}$. Once magnetized and at low temperatures, its spin can remain in state $m_s = -2$ for relatively long durations due to the energy barrier $3D$ and momentum $4\hbar$ required to reverse it.[29,30] Large-spin systems with a large $D < 0$ and $E \approx 0$ are therefore referred to as single-atom[31–35] (or single molecule[8,36]) magnets. Ti, as a doublet, cannot exhibit a zero-field splitting; it can however show large g-factor anisotropy.[37–39]

In this thesis, we spectroscopically probe the magnetism of such atomic and molecular species with the scanning tunnelling microscope (STM). This is achieved in by inelastic electron tunnelling spectroscopy, which will be described in Section 1.3.2. We also employ magnetic resonance to probe Ti/MgO. This technique is introduced in Section 1.3.3.

1.1.2 Chiral graphene nanoribbons

Electronic spins can occur even in molecules without metallic ions. A particularly elegant example is given by the family of nanographenes, which we will introduce here. Bulk graphene, a single layer of carbon atoms arranged in a honeycomb lattice, hosts highly delocalized π-electrons. As such, it is a purely diamagnetic material.[40] However, when confined to nanoscopic dimensions, spin-polarized states can emerge on its edges and give rise to net magnetic moments.[41–45] Since these radicals occur as a consequence of the molecular geometry alone, great tunability is afforded.[46]

Simple counting rules allow predicting both the number of radicals, and the resulting magnetic ground states. The carbon atoms in graphene are distributed among two interwoven hexagonal sublattices, such that sites on sublattice A only neighbour those on B; this is known as a bipartite graph. The Ovchinikov-Lieb theorems[47,48] state that the total spin S of a nanographene must fulfil $2S = |N_A - N_B|$. An equal number of sites in either sublattice ($N_A = N_B$) thereby precludes a net magnetic moment. In this thesis, we study an intriguing nanographene geometry, which despite not possessing sublattice imbalance, exhibits highly localized spins due to its topologically non-trivial electronic structure.

The edges of a graphene flake are naturally formed by two segments called zigzag and

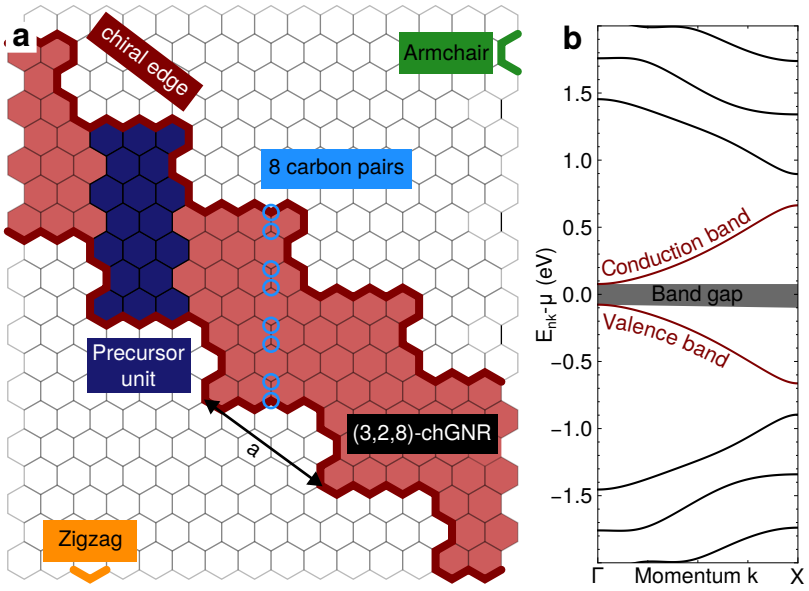

Figure 1.2: **(a)** Definition of the $(3, 2, 8)$-chiral graphene nanoribbon (chGNR), shown in red, within the graphene lattice. **(b)** Tight-binding band structure of the infinite length $(3, 2, 8)$-chGNR. We identify a gap delimited by two bands, which are localized on the chiral edge.

armchair, as indicated in Figure 1.2a in yellow and green. Cutting out a thin, infinite-length strip along these directions gives the mirror-symmetric armchair graphene nanoribbon (GNR) and zigzag GNR, respectively. The latter exhibits fully metallic edge-localized bands, whereas the former is fully gapped. The family of chiral graphene nanoribbons is instead obtained by cutting along low-symmetry directions, as that indicated in red.[41,45] We define their geometry by a chiral vector (m, n, w), where we denote by m the number of zigzag elements and by n the quantity of armchairs along the chiral edge, and by w the width given by the count of carbon pairs along the armchair direction as shown in Figure 1.2a. Their finite width gives rise to a small band gap, but maintains the zigzag-edge-localized character of the conduction and valence bands.[49] The band structure for chiral vector $(3, 2, 8)$, here obtained from a tight-binding description of the π electrons, is displayed in Figure 1.2b. For this particular width, the narrow band gap is in fact inverted, which gives $(3, 2, 8)$-chGNR a topological invariant $\mathbb{Z}_2 = 1$.[50]

In our experiments, chGNRs will be of finite length. We denote by L the number of precursor units (PUs) employed for their synthesis, which become the structure's rectangular motif as highlighted in Figure 1.2a. Quantum confinement of edge electrons between each end leads to the discretization of bands into molecular orbitals. In Figure 1.3a, we project the tight-binding density of states (DOS) of the quantized conduction band onto the carbon atoms forming the chiral edge, where it is largest. Evidently, these discrete states exhibit nodal planes, reminiscent of a particle trapped in a potential well. We therefore refer to them as quantum well (QW)-like states in the following discussions. Additional insight is gained by Fourier transformation of the DOS,[51,52] as seen in Figure 1.3b. We observe a series of parabolas surrounding the band gap. Each pertains to a Brillouin zone of width $2\pi/a$, where $a = 1.075$ nm is the real-space periodicity of the chiral edge. Clearly, these parabolas intersect at odd multiples of $\pi/2a$. It is precisely at this crossing that the number of nodal planes in real space no longer increases with energy, but begins to decrease. This is where the QW analogy breaks down, as the periodicity of the molecular orbitals approaches that

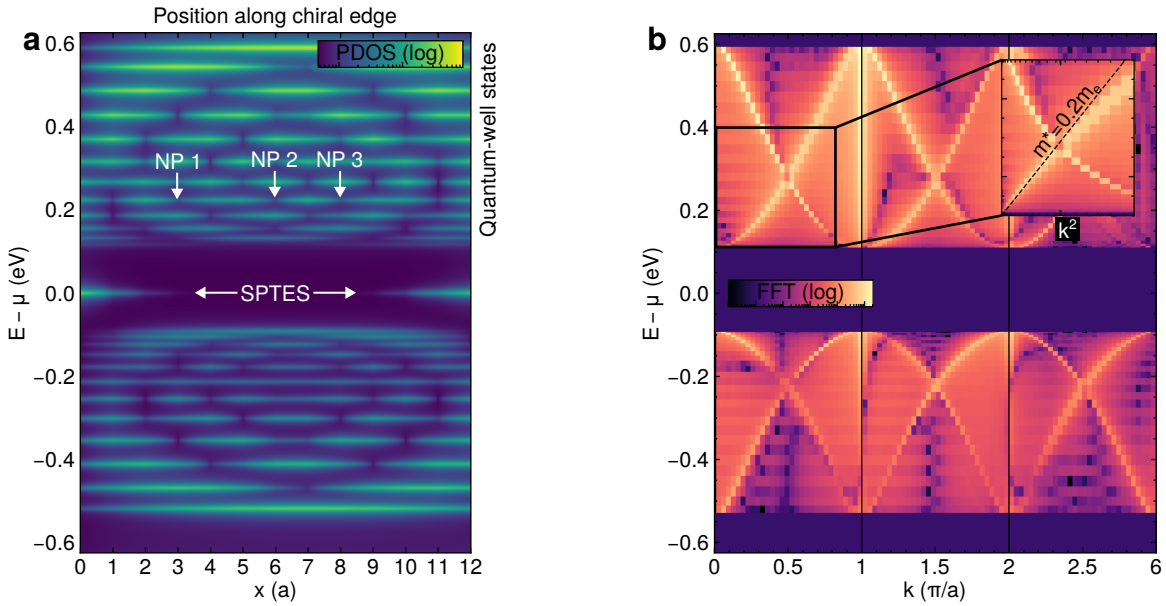

Figure 1.3: **(a)** Tight-binding orbitals of a finite chGNR. We plot the projection onto carbon atoms on the chiral edge, as a function of their position in units of its periodicity a. A pair of symmetry-protected topological end states (SPTESs) emerge in the energy gap, and discrete QW-like states form. They are enumerated by their number of nodal planes (NP). **(b)** Dispersion of the QW-like states. We show the Fourier transform of the data in **(a)**. The parabolic bands cross at the Brillouin zones marked vertically. In the inset, the effective mass m^* is determined by plotting against k^2.

of the carbon backbone. This inverted ordering will bear significance in Section 4.1.

Length confinement results in a secondary effect: the creation of two zero-energy modes, as seen in Figure 1.3a. They are imposed by the bulk-boundary correspondence between the topologically nontrivial chGNR and trivial vacuum[53–55] and as such are localized on opposing ends of the chiral edge. Their occurrence is protected by the symmetry of the conduction and valence bands,[50] and as such we will refer to them as SPTES. At half filling (one electron per carbon site, charge neutral), both SPTESs are occupied by a single electron each, and therefore constitute two local magnetic moments. To comply with the counting rule stated before, these radicals must align antiferromagnetically to give $S = 0$. We note at this point that for short lengths, the SPTESs will begin to overlap and open a secondary hybridization gap around zero energy. As long as $L \geq 3$ PU, this effect does not modify the magnetic ground state, but will be of use in Section 3.1.

The intramolecular spin-spin interaction that stabilizes the singlet configuration arises from the Coulomb repulsion among π electrons. The simplest framework reproducing such correlations is the Hubbard model:

$$\mathcal{H} = \varepsilon \sum_{i,\sigma} \hat{n}_{i\sigma} + t_k \sum_{i,j\in k\mathrm{NN},\sigma} \left(\hat{c}^\dagger_{i\sigma}\hat{c}_{j\sigma} + \hat{c}^\dagger_{j\sigma}\hat{c}_{i\sigma}\right) + U_\mathrm{H} \sum_i \hat{n}_{i\downarrow}\hat{n}_{i\uparrow} \tag{1.4}$$

Here, $\hat{c}^\dagger_{i\sigma}$, $\hat{c}_{i\sigma}$ and $\hat{n}_{i\sigma}$ are the creation, annihilation and number operators for π electrons

at lattice site i with spin $\sigma = \downarrow$ or $\uparrow$. The first term defines an on-site energy ε, which is commonly set to zero. The second term is the tight-binding Hamiltonian with hopping parameters t_k for k'th nearest neighbours (NN). Here, we use $t_1 = -2.7\,\text{eV}$, $t_2 = -0.2\,\text{eV}$ and $t_3 = -0.18\,\text{eV}$.[56] Inclusion of the second and third order hopping increases accuracy in reproducing bands and has been found to be essential in correctly reproducing intramolecular exchange in related systems.[57–59] Lastly, the interaction term produces electron-electron correlations by imposing an energy penalty for double occupancy of the same carbon site, and thereby distorts the tight-binding orbitals. Its magnitude is given by the Hubbard parameter U_H, which competes with the kinetic energy given by the hopping terms. If $U_\text{H} \gg t_k$, the atomic limit is reached, with each spin species fully confined to one of the sublattices. If $N_\text{A} = N_\text{B}$, as in our case, neither local nor net magnetic moments are found. Conversely, in the tight-binding limit $U_\text{H} = 0$, the π electrons of either spin are fully delocalized and equally distributed over A and B as hopping between carbon sites is spin-independent, and the SPTESs are arbitrarily aligned. However, if $U_\text{H} \approx t_k$, Coulomb repulsion will favour the separation of spin up and spin down electrons into SPTESs located in different sublattices to minimize double occupancy. This gives rise to antiferromagnetically oriented local moments. The large number of carbon sites (hundreds for chGNRs) makes the Hubbard Hamiltonian intractable. Its main features are however well reproduced in the mean-field approximation:[60–63]

$$\mathcal{H}_\text{U} = U_\text{H} \sum_i \langle \hat{n}_{i\uparrow} \rangle \hat{n}_{i\downarrow} + \langle \hat{n}_{i\downarrow} \rangle \hat{n}_{i\uparrow} - \langle \hat{n}_{i\uparrow} \rangle \langle \hat{n}_{i\downarrow} \rangle \tag{1.5}$$

The expectation values of the number operators in the first two terms are the spin densities across the molecule, which now only act as on-site energies for the opposing spin. The last term is a rigid shift in the energy spectrum proportional to U_H and the probabilities of double occupation. Since this is a single-particle Hamiltonian, we can solve it self-consistently. Starting from a qualitative guess for the mean field, wavefunctions for either spin are calculated, squared and summed to obtain new spin densities, and-reinserted. This process is iterated until the solutions of Equation (1.5) give the same spin densities as those used to produce them. This procedure is implemented in the `hubbard` package that has been made publicly available by Sanz Wuhl *et al.*[64].

We will outline a few solutions of the MFH model for finite $(3, 2, 8)$-chGNRs. At half-filling, the Hubbard term stabilizes the expected spin-singlet ($S = 0$) configuration as a ground state (Figure 1.4a). This manifests as the opening of a correlation gap between the four SPTES spin-orbitals such that the left terminus is occupied by a single electron, and the right by one of opposing spin, here spin-up. They may also be referred to as singly occupied molecular orbitals (SOMOs). The singly unoccupied molecular orbitals (SUMOs) in this case consist in a spin-up hole on the left and a spin-down hole on the right. We can also obtain a solution for the energetically unfavourable triplet state ($S = 1$), see Figure 1.4b. A similar gap opens, but the singly occupied orbitals are reordered such that both termini hosts a single spin-up electron.

In the following experiments, we will depart from half-filling by inducing anionic charge states. This acts analogously to n-type doping in shifting the chemical potential μ up in

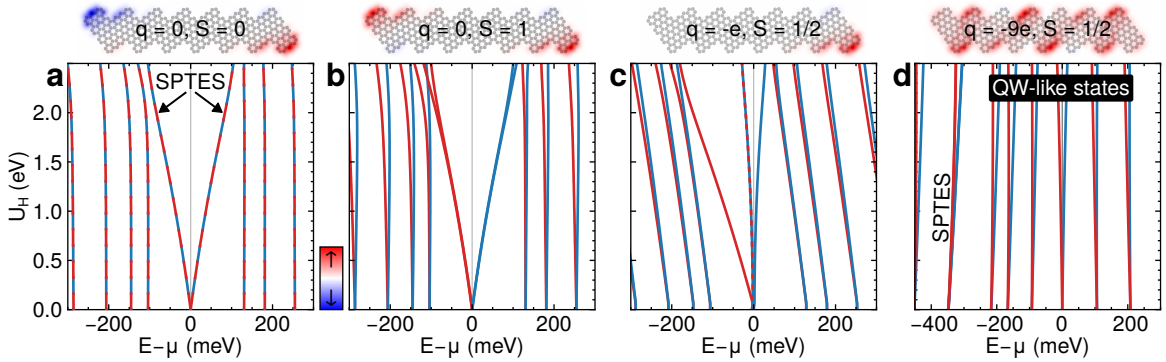

Figure 1.4: Mean-field Hubbard model (MFH) solutions for charge-neutral and anionic 7 PU (3, 2, 8)-chGNRs that exhibit local magnetic moments. We plot the evolution of energy levels as a function of U_{H}. We also show the mean-field spin polarization $\langle \hat{n}_{\uparrow} \rangle - \langle \hat{n}_{\downarrow} \rangle$ above. Red denotes spin-up, and blue spin-down. **(a)** The neutral singlet, **(b)** the neutral triplet, **(c)** the singly anionic doublet (q=-e), **(d)** the $q = -9e$ delocalized doublet.

energy. Figure 1.4c considers the charge state $q = -e$. The single excess electron here leads to double occupation of the left SPTES, which now remains spin-degenerate under the influence of U_{H} and constitutes the highest occupied molecular orbital (HOMO). The right terminus retains its localized spin-up π radical. Here, the Hubbard term opens a gap between SOMO and SUMO. The former lies below the HOMO. The resulting spin state is a doublet with broken inversion symmetry[1]. Lastly, if three or more surplus electrons are present, μ lies within the range of QW-like states introduced above. If q is odd, as shown in Figure 1.4c, one again has singly occupancy. In contrast to the previous cases, this SOMO is distributed along the whole molecule. Electron correlations open a gap also in this case, but it is much narrower as the spin-densities are smaller due to the delocalization of the unpaired electron.

1.2 Surface interactions of atomic and molecular spins

1.2.1 Charge transfer

Interfacing a single molecule with a metallic surface can severely modify its electronic state. We will here introduce dominant effects that occur in the limit of weak physisorption. To this end, we consider a closed-shell molecule, with two frontier orbitals around the chemical potential: the HOMO, and the LUMO, as shown in Figure 1.5a. In the gas phase, their energy, referred to the vacuum, is also known as the ionization potential (IP) and electron affinity (EA), referring to the cost of removing or adding a single electron, respectively. Intramolecular Coulomb interaction between a surplus hole or electron with the remaining particles causes the IP and EA to deviate from the neutral-state HOMO and LUMO energies.[65] Transferring an electron between vacuum and the bare metal's Fermi energy re-

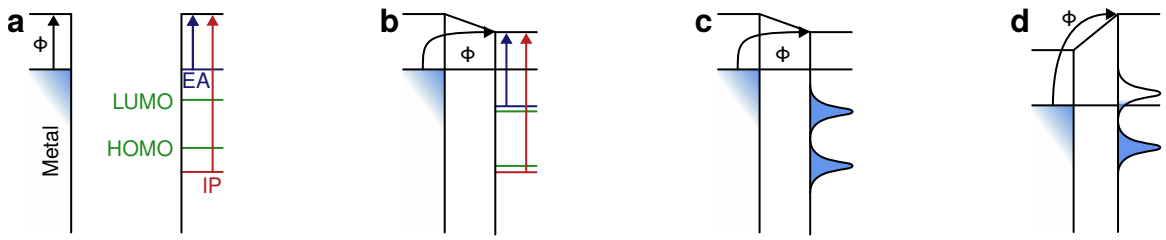

Figure 1.5: Electrostatics of the interface between a single weakly physisorbed molecule and a low work-function metal. Effects are added incrementally. **(a)** In the gas phase, EA and IP differ from the molecular orbital energy due to intramolecular Coulomb repulsion. **(b)** The pillow effect reduces the metal's work function ϕ. Electron-electron correlation are screened. **(c)** Wavefunction hybridization broadens molecular resonances. Charge is transferred into the molecule. **(d)** The interface dipole raises ϕ, emptying the hybridized lowest unoccupied molecular orbital (LUMO). In this final configuration, the charge state is fractional.

quires work ϕ. At large separations, the respective vacuum levels of molecule and metal are aligned.

As the molecule is approached towards the surface, the quantum mechanical spill-out of the metal's electrons is perturbed. In general, the exponential tails of the wavefunction are pushed back into the crystal by the Pauli repulsion with the molecular orbitals, which results in a lowering of its intrinsic surface dipole. The redistribution of charge, known as the pillow effect,[66] gives a locally decreased work function ϕ, as indicated Figure 1.5b. Due to screening of intramolecular Coulomb correlation, the energy required to add or remove electrons to and from molecular orbitals is lowered by metallic substrates. This results in an apparent gap decrease between frontier orbitals in tunnelling experiments.[65,67,68]

If the modified electron affinity lies below the Fermi level, electrons are transferred into the molecule. This is typical of metallic surfaces with small intrinsic work functions, such as Ag(100). The opposite occurs for surfaces with large ϕ such as Au(111).[69] At closer physisorption distances, the hybridization of the molecular wavefunction with the metal's will broaden its density of states; this allows for fractional charge states where the chemical potential lies within a molecular resonance.

The presence of a charge on the surface also sets up a secondary potential step called the interface dipole. For negative charges, as shown in Figure 1.5c, it results in an up-shift of the molecular vacuum level, and thereby an increase in the local work function. These competing effects are energetically balanced and determine the molecule's charge state, its spatial separation from the surface, and the local work function.[70]

1.2.2 The Kondo effect

Metallic surfaces act on atomic or molecular spins not only electrostatically, but also magnetically. If such a system is brought into close contact with a metal, i.e. placed on its surface, it constitutes an impurity with which conduction electrons can scatter. The Coulomb repulsion felt by a traveling electron as it approaches the impurity gives rise to an antiferromagnetic exchange coupling $J < 0$ between their spins. This interaction enables scattering events, as those shown in Figure 1.6, where angular momentum is exchanged as impurity and conduction electron swap their spin. The scattering electrons originate and end up close to the Fermi surface, where plenty filled and empty states are available in a narrow energy range. This spin-flip process is detrimental to the quantum coherence of a molecular spin, as it resets its magnetic state. We will explore several techniques by which these processes can be suppressed.

Magnetic scattering is not limited to a single electron. One can also envision events in which two electrons are involved, successively flipping the impurity spin back and forth. One example is shown in Figure 1.6. However, these processes are less likely to occur. This picture changes completely as the temperature is lowered. Below a critical point called the Kondo temperature T_K, the probability of two-electron events diverges logarithmically and dominates the ordinary process.[71–76] The scattering picture is then no longer applicable, and one must resort to a many-body description. Its central result is the formation of a correlated ground state, in which the impurity spin is entangled to the conduction electrons, forming a singlet-like state. In the electronic DOS, this manifests as a sharp peak of width $\propto k_B T_K$ at the Fermi energy, the Abrikosov-Suhl resonance.[77–82] We will refer to it simply as a Kondo peak.

In this thesis, we employ the Kondo effect as a spectroscopic probe of magnetism. Its observation implies both the existence of a molecular spin, and its coupling to a surface. From the peak width, the Kondo temperature, which is a measure of the exchange interaction between impurity and conduction electrons, can be determined.[79,83,84] Additional insight is gained by

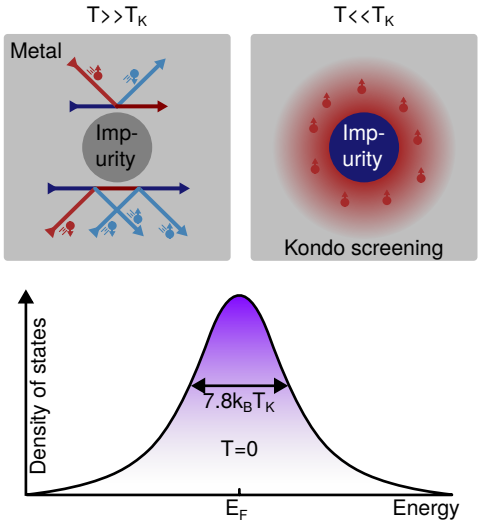

Figure 1.6: The Kondo effect of isolated magnetic moments in contact with metals. Above the critical temperature T_K, itinerant conduction electrons flip its spin via the scattering processes shown. At very small temperatures, the correlated Kondo screening cloud forms. In this instant, the impurity is drawn spin-down. Below, we sketch the Kondo resonance with its characteristic width at zero temperature.

observing its reaction to a magnetic field. Due to the Zeeman effect, the spin flips become inelastic, and the Kondo resonance splits apart.[85] Typically, the Kondo effect is considered only for $S = 1/2$ impurities, whose spin can be reversed by a single electron. However, for higher spins, such scattering can also occur in special cases. This will be addressed in Section 3.2.

1.3 Scanning probe microscopy

1.3.1 Scanning tunnelling microscopy and spectroscopy

The scanning tunnelling microscope has revolutionized the study of surfaces with its ability to visualize single atoms, molecules and atomic lattices in real space. Its spatial resolution relies on the tunnel effect - the ability of quantum particles to escape potential barriers - and piezoelectricity, the susceptibility of certain crystals' dimensions to electric fields. Figure 1.7a shows a typical arrangement of an STM. A metal wire (here tungsten) is electrochemically etched to produce a nanoscopically sharp tip, and attached to a piezoelectric tube. By applying a voltage to its electrons, the tip can be moved in three cartesian directions via piezoelectric contraction and extension. Crucially, this movement is extremely precise, down to the atomic scale.

When the tip is brought within nanoscopic distance to a conductive surface, electrons tunnel back and forth between them. With an additional voltage bias U, a net tunnelling current I can be measured using a high-gain amplifier. Due to the nature of quantum tunnelling, this signal decays exponentially with the tip-surface separation d. For instance, in this thesis, we measure currents ranging from 10 fA, at a distance of several nanometers, to 1 µA, at a few Ångstroms (Å). As the tip scans the surface in the two lateral dimensions x, y while z is fixed, the exponential characteristic allows recording changes in tunnelling current con-

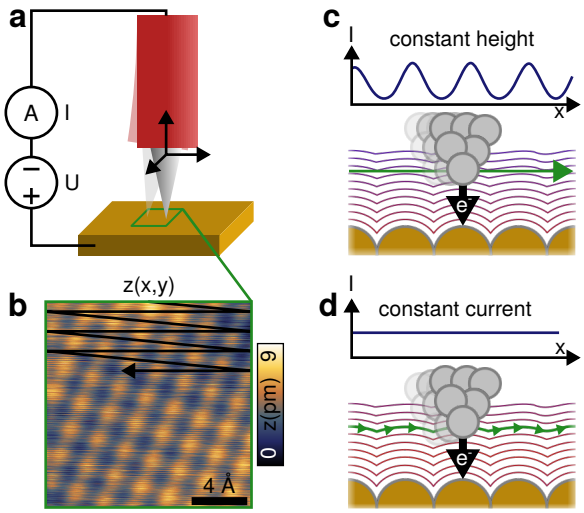

Figure 1.7: Operating principle of the STM. **(a)** A sharp tip is brought close to a conductive surface. With an applied voltage bias U, a net tunnelling current I flows. Piezo actuation in three dimensions allows scanning the surface. **(b)** Atomically resolved lattice of Ag(100) at $U = 10$ mV and 1 nA. The microscope can be operated with the tip **(c)** at a constant height z, recording changes in I. **(d)** Alternatively, the tip is guided along a constant-current trajectory by a feedback loop, which gives the topographic data as $z(x, y)$. This mode was used in **(b)**.

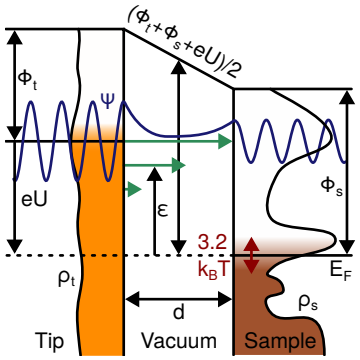

Figure 1.8: Energetics of the tunnelling junction. Tip and sample, with different work functions ϕ and densities of states ρ are separated by vacuum. The bias voltage offsets the electrochemical potentials by eU. The finite barrier height and width allows a travelling electron to tunnel from the tip's Fermi level to the sample's unoccupied states. Its wavefunction is sketched in blue. The integrand of Equation (1.6) is shown in green.

gruent with the sample's nanoscopic topography. This is the constant-height (CH) imaging mode. If the tip apex consists of a single atom, even individual atoms and molecules are resolved. Quantitative topographic information is obtained in the constant-current (CC) mode. Here, an electronic feedback controller continuously makes adjustments to z, such that the tip apex moves along contours of constant current (Figure 1.7b). The 3D data $z(x, y)$ is then, with some important limitations, an "image" of the surface at the atomic scale with a typical precision on the order of 1 pm. To resolve such detail, it is essential that the sample be flat and clean, and that no external vibrations perturb the tunnelling junction's separation.

The STM also provides spectroscopic information. The tunnelling junction is schematically shown in Figure 1.8. The tunnelling current, under several assumptions,[86,87] can be written in terms of the metallic tip and sample DOS $\rho_t(E)$ and $\rho_s(E)$, referred to the sample's Fermi level as $\varepsilon = E - E_F$:

$$
\begin{aligned}
I(U,d) &= \frac{4\pi e}{\hbar}\int_{-\infty}^{\infty}\left(f(\varepsilon-eU)-f(\varepsilon)\right)\rho_t(\varepsilon-eU)\rho_s(\varepsilon)\mathcal{T}(\varepsilon,U,d)\mathrm{d}\varepsilon \\
\mathcal{T}(\varepsilon,U,d) &\approx \exp\left(-2d\sqrt{\frac{2m_e}{\hbar}\left(\frac{\phi_t+\phi_s+eU}{2}-\varepsilon\right)}\right)
\end{aligned}
\tag{1.6}
$$

Here, $f(E)$ is the Fermi-Dirac distribution at the experimental temperature. Tip and sample wavefunctions decay exponentially in vacuum, but overlap due to the small separation of the tunnelling junction. The resulting finite tunnelling probability depends on the height and shape of the barrier, which is described by the transmission factor $\mathcal{T}(\varepsilon, U, d)$. We approximate the barrier as rectangular of height $(\phi_t + \phi_s + eU)/2$, with the tip and sample work functions ϕ_t and ϕ_s. It is the exponential dependence of the transmission factor on the barrier width d that enables the spatial resolution of STM discussed previously. However, if it is also sensitive to the barrier height; in this way, a locally lowered work function will give a larger tunnelling current. The topographic signal in CC mode is therefore better referred to as "apparent height". The transmission factor also depends on the energy of the tunnelling electrons: states near the tip's Fermi level experience the smallest barrier height and exponentially dominate the integrand of Equation (1.6). This makes the tunnelling current highly sensitive to the tip and sample DOS at $\varepsilon = -eU$, which allows for tunnelling spectroscopy. If one assumes ρ_t and $\mathcal{T}(\varepsilon, U, d)$ to be bias- and energy-independent, one can

write the differential conductance $\mathrm{d}I/\mathrm{d}U$ as

$$\frac{\mathrm{d}I}{\mathrm{d}U} = \frac{4\pi e}{\hbar}\mathcal{T}(d)\rho_{\mathrm{t}}\int_{-\infty}^{\infty} f'(\varepsilon - eU)\rho_{\mathrm{s}}(\varepsilon)\mathrm{d}\varepsilon \tag{1.7}$$

which is a convolution of $\rho_{\mathrm{s}}(E)$ with $f'(E)$, the peak-shaped derivative of $f(E)$. Therefore, $\mathrm{d}I/\mathrm{d}U$ is a direct measure of the DOS of surfaces, atoms and molecules, which we will exploit extensively. In a differental conductance spectrum, $U = 0$ represents the sample's Fermi level. Occupied states are probed at $U < 0$, and unoccupied states at $U > 0$. The energy resolution with which one samples ρ_{s} is given by the width $3.2k_{\mathrm{B}}T$ of f'. Therefore, the microscopes used in this thesis operate at cryogenic temperatures, which enables us to sense molecular orbitals with meV resolution. The spectroscopic signal is obtained by sinusoidal modulation of the tunnel bias such that $U = U_{\mathrm{DC}} + U_{\mathrm{AC}}e^{i\omega t}$. The component of the tunnelling current at frequency ω is then measured via lock-in detection as $I_{\mathrm{AC}} = U_{\mathrm{AC}}\,\mathrm{d}I/\mathrm{d}U$, and thereby the differential conductance is determined. Higher order derivatives are obtained at the harmonics $n\omega, n > 1$.

1.3.2 Spin-flip spectroscopy

We have seen how unpaired electrons in single atoms and molecules can give paramagnetic ground states. scanning tunnelling spectroscopy (STS) is an indispensable tool for probing these local magnetic moments via the Kondo effect at low temperatures. We now introduce another spectroscopic method which allows detecting magnetism even if no such coupling is present. The mechanism is simply understood: if the energy eU of the tunnelling electrons exceeds the energy needed to flip the spin of the system under study (the "impurity"), the differential conductance will show a sharp increase. This is because the exchange of angular momentum $\Delta m_s = \pm\hbar$ between the impurity and the tunnelling electrons constitutes a separate transport channel, in addition to the purely elastic current considered until now. This inelastic current is measured in spin-flip spectroscopy, first realized by Heinrich *et al.*[25]. Similarly, vibrational modes can be excited inelastically,[88] which is why we refer to spin-flip spectroscopy also by the broader term IETS.

We briefly re-state here the encompassing treatment given by Ternes[75] based on perturbation theory of the Kondo effect.[72,74,89,90] In this picture, the measured current is made up of Kondo-like scattering events between the impurity and both tunnelling and substrate electrons. These may be inelastic, when mediated by their exchange interaction, or elastic. For sufficiently decoupled magnetic impurities, the resulting simulated spectra have been shown repeatedly to give excellent agreement with experiments. We will use this model throughout this thesis to extract the magnetic parameters of our systems under study from their IETS curves. In Section 5.2, we will also employ it to quantify the effect of scattering in a proposed double-resonance scheme for molecular spin qubits.

In the scattering rate formalism, the sum of elastic and inelastic current at a given sample

bias voltage U can be written as

$$I(U) = e\sum_{i,f} p_i(U)\left(\Gamma_{if}^{\mathrm{TS}}(U) - \Gamma_{if}^{\mathrm{ST}}(U)\right) \tag{1.8}$$

where p_i are the populations of the spin levels, and Γ_{if}^{lk} are the transition rates between electrodes l, k (tip T or substrate S) scattering through states i, f. The rates depend on Fermi's golden rule matrix elements via $M_{if,2}^{lk}$ and $M_{if,3}^{lk}$ for second and third order, respectively, in an integral accounting for the thermal occupation probabilities in the electrodes. We have

$$\Gamma_{if}^{lk} = \frac{G_{\mathrm{TS}}}{G_0}\frac{1}{\hbar}\int_{-\infty}^{+\infty}\left(\left|M_{if,2}^{lk}\right|^2 + M_{if,3}^{lk}(E)\right) f(E+eU)\left(1 - f(E+E_i-E_f)\right)\mathrm{d}E \tag{1.9}$$

where $f(E)$ is the Fermi-Dirac distribution at the experimental temperature. The current is here simply scaled by the constant-height conductance G_{TS}, absorbing all parameters resulting from microscopic tunnelling theory. Analogously, we can define rates $\Gamma_{if}^{\mathrm{SS}}$ that describe the substrate-substrate scattering that give rise to the conventional Kondo effect. They are scaled by the conductance G_{SS}.

The dimensionless matrix elements are those of the antiferromagnetic Kondo exchange term $J\hat{\mathbf{S}}\cdot\hat{\boldsymbol{\sigma}}$ between the impurity spin $\hat{\mathbf{S}}$ and the tunnelling electrons $\hat{\boldsymbol{\sigma}}$. One also includes a potential scattering term P, which represents all non-magnetic elastic processes. We will set it to zero unless stated otherwise. To second order in J, i.e. scattering involving a single tunnelling electron, these matrix elements are

$$M_{if,2}^{lk} = \frac{1}{\hbar}\left(\sum_{d=xyz}\xi_d\langle f|\hat{S}_d|i\rangle + P\xi_1\langle f|\hat{1}|i\rangle\right) \tag{1.10}$$

where $\hat{1}$ is the identity spin operator. The coefficients ξ depart from unity if any of the electrodes l and k are spin-polarized in any arbitrary direction, which will be discussed in the following. They are defined as

$$\begin{aligned}\xi_d &= \frac{1}{\hbar}\sum_{ab}\sqrt{\lambda_a^{\mathrm{T}}\lambda_b^{\mathrm{S}}}\langle b|\hat{\sigma}_d|a\rangle\\ \xi_1 &= \frac{1}{\hbar}\sum_{ab}\sqrt{\lambda_a^{\mathrm{T}}\lambda_b^{\mathrm{S}}}\langle b|\hat{1}_d|a\rangle\end{aligned} \tag{1.11}$$

where $\hat{\sigma}_d$ are the Pauli matrices. The summation through a and b is over the two spin states of the tunnelling electron. The latter are eigenstates of the density matrix of the arbitrarily spin-polarized tip and sample, with eigenvalues λ corresponding to the degree of polarization. This quantity can be understood as the projection of the tip polarization vector onto the impurity quantization axis.

The third-order scattering amplitudes are calculated from the second-order matrix elements by

$$\begin{aligned}M_{if,3}^{lk} = J\rho\Re\sum_m & M_{fi,2}^{\mathrm{lk}}M_{mf,2}^{\mathrm{SS}}M_{im,2}^{\mathrm{lk}}F(E_m-E_i-E) + \\ & M_{fi,2}^{\mathrm{lk}}M_{mf,2}^{\mathrm{lk}}M_{im,2}^{\mathrm{SS}}F(E_i-E_m-E)\end{aligned} \tag{1.12}$$

where J is the Kondo exchange coupling between impurity and substrate conduction electrons. In these events, scattering between impurity and tunnelling electrons is accompanied by scattering with a substrate electron. We have omitted the additional interference terms scaling with the potential scattering P for clarity. Temperature broadening is captured by

$$F(E) = -\int_{-\infty}^{+\infty} \int_{-\omega_0}^{+\omega_0} \frac{f(\omega)}{\omega - \epsilon} \, \mathrm{d}\omega \, f'(\epsilon - E) \, \mathrm{d}\epsilon \tag{1.13}$$

which accounts for the occupation probabilities in the intermediate states, assuming a constant substrate density of states ρ in the finite energy interval $[-\omega_0, +\omega_0]$. The dimensionless parameter $J\rho$ is related to the Kondo temperature via

$$k_\mathrm{B} T_K = \omega_0 e^{1/J\rho} \tag{1.14}$$

In theory, $J\rho$ should also define the substrate-substrate conductance ($G_\mathrm{SS} \propto (J\rho)^2$) as both derive from the wavefunction overlap between substrate and adsorbate. In experiments, significant deviations from this relation are observed.[75,76] We therefore treat $J\rho$ as an independent quantity that simply scales the participation of third-order scattering processes.

From Equation (1.8), the $I(U)$ characteristic and thereby $\mathrm{d}I/\mathrm{d}U$ can be calculated. Usually this is done in the limit $G_\mathrm{TS} \to 0$, i.e. large tip-sample separations. Then, p_i tends towards the thermal equilibrium values and is independent of U. This is also valid for realistic values of $G_\mathrm{TS} < 1\,\mu\mathrm{S}$ for adsorbates on metallic substrates, which are rapidly thermalized by the substrate-substrate scattering. The differential conductance spectrum then consists of a series of symmetric steps, placed at the inelastic spin-flip threshold voltages and with a height proportional to the matrix elements $\left|M^{lk}_{if,2}\right|^2$. Inclusion of the third order processes places additional peak-like overshoots at these thresholds, proportional to $M^{lk}_{if,3}(E)$. Notably, it also produces a zero-bias peak if processes with $i = f$ through a degenerate intermediate state are allowed by conservation of angular momentum - a Kondo resonance. In Section 3.2, we will lock-in detect the signal $\mathrm{d}^2I/\mathrm{d}U^2$ as the second harmonic of the modulated tunnelling current. Then, inelastic transitions appear as peaks, with widths equal to $5.4 k_\mathrm{B} T$.

We will now consider the effect of a magnetic electrode on spin-flip spectroscopy,[91] as will be realized Section 2.2. In a magnetic field, the Zeeman effect magnetizes impurities by splitting levels according to $\langle \hat{S}_z \rangle$. Elastic tunnelling between such an atom or molecule and a spin-polarized electrode (usually the tip) will then depend on the relative alignment between them, regardless of bias. Following the Stoner model of ferromagnetism, we can consider the tip electronic states ρ to be spin-split at the Fermi level as shown in Figure 1.9a, such that the majority spin is "up". Since the tunnelling probability directly scales with the tip DOS, a larger current can flow if the impurity spin possesses the same polarization ("up"). The larger the Stoner gap of the tip and the Zeeman energy of the impurity, the more sensitive tunnelling will be to the impurity polarization. To quantify the spin selectivity, it is customary to define the parameter $\eta = \dfrac{\rho_\uparrow - \rho_\downarrow}{\rho_\uparrow + \rho_\downarrow}$ which ranges from -1 to 1 for fully spin-down to spin-up polarization. This effect is called elastic tunnel magnetoconductance

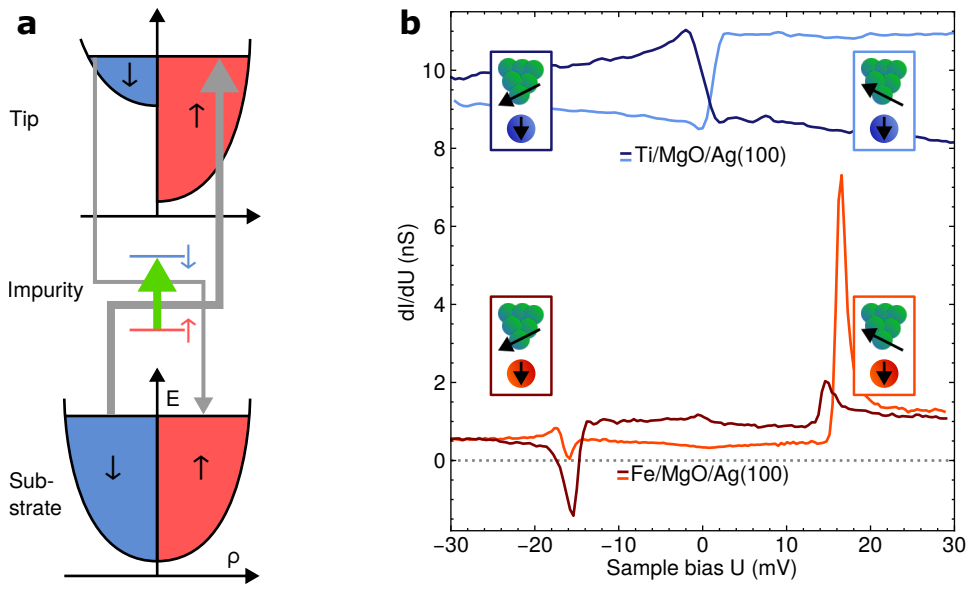

Figure 1.9: **(a)** Scheme of spin-polarized inelastic electron tunnelling. Shown are the dominant rates for either tunnel direction. **(b)** Examples of spin-polarized tunnelling into Fe and Ti atoms on MgO/Ag(100) for aligned and anti-aligned tip polarizations. Insets show orientations consistent with the inelastic step asymmetry. All curves were recorded with different tips and atoms at out-of-plane fields on the order of 0.5 T. Data on Ti has been shifted upwards for clarity.

(or magnetoresistance), and forms the basis of spin-polarized STM (SP-STM) which allows mapping the magnetization vector of surfaces with atomic resolution.[92,93] It will allow us to detect the magnetic state of a single atom without flipping its spin.

The inelastic tunnelling through the impurity is also modified by tip polarization. We consider the impurity and tip being polarized spin-up. In this case, the significant excitation is the transfer of an angular momentum quantum $\hbar$ to the tunnelling electron, in which the impurity is flipped into the spin-down state (Figure 1.9a)[2]. For sample-tip tunnelling, dominant at negative bias voltage, a large number of majority final states are available in the tip to accommodate the spin-up electron after this process. However, for positive sample biases, tip-sample tunnelling dominates. Since the density of initial states of spin-down electrons in the tip is small, the inelastic contribution to the total current will therefore be suppressed with respect to negative bias polarity. This manifests as an asymmetry in the differential conductance steps. The magnitude of the inelastic magnetoconductance effect is given by the coefficients ξ in Equation (1.11). If the quantization axes of tip and impurity spins are identical, ξ can be obtained from η. If the tip and impurity are oppositely aligned, this asymmetry inverts, which is often the case in STM experiments.[91]

In Figure 1.9b, experimental spin-polarized inelastic tunnelling spectra are shown for individual Ti and Fe atoms on MgO/Ag(100). Ti, being a $S = 1/2$, in principle allows to directly infer the tip polarization sign and magnitude η. Since the tip polarization is large

and the Zeeman energy small compared to the thermal broadening (here $T = 1.3\,\mathrm{K}$), only the dominant conductance step is resolved in these measurements. For the two magnetic tips shown, the larger step lies at negative and positive bias, which implies ferromagnetic and antiferromagnetic alignment between tip and atom, respectively.

In the easy-axis $S = 2$ case of Fe, the primary observation with highly spin-polarized tips are the peak-like features approximately at the inelastic threshold voltages $\pm 3D/e$ given by the magnetic anisotropy. These are the combination of two effects: spin-pumping and magnetoconductance. Due to the presence of a decoupling layer, the longitudinal relaxation time T_1 is large. The spin-polarized current then leads to changes in the magnetization of the probed system via its inelastic component.[94]

We can rationalize this by considering that in typical measurements with $I \approx 100\,\mathrm{pA}$, the mean time between sequential tunnelling events amounts to $e/I \approx 1.6\,\mathrm{ns}$. Fe/MgO and similar atoms exceed this value by far,[29,33] such that spin-polarized electrons can populate the excited spin levels faster than the impurity magnetization relaxes. While a spin-unpolarized current would just raise the effective electronic temperature, spin-polarized tunnelling can drive ("pump") the system far out of thermal equilibrium into a different magnetization state.[75,94]

The spin-pumping effect adds characteristic tails to the inelastic conductance steps since the ground-state population is diminished with increasing current (voltage).[94] An additional effect can occur: if the impurity magnetization is pumped away from the tip polarization, the elastic magnetoconductive current will decrease. In extreme cases, this manifests as a negative differential resistance feature[95] as in Figure 1.9b. Since the polarity of the dominant inelastic response is reversed for the two tips used, we anticipate that their magnetization has opposite projections onto the impurity's quantization axis, as shown in the inset sketches. Note that in these measurements, only the time-average magnetization of the atom is probed, as T_1 is still much smaller than the measurement's time constant.

To reproduce spin-pumping effects, we seek the steady-state populations p_i that arise in dynamic equilibrium between the tunnelling current and T_1 processes. The latter are conveniently given by the Kondo scattering rate $\Gamma^{\mathrm{SS}}_{if}$. If the density matrix of the magnetic impurity is diagonal, i.e. has no coherences, the populations follow the Pauli master equation:[75,94,96]

$$\frac{\mathrm{d}p_i}{\mathrm{d}t} = \sum_j \left(p_j \sum_{lk} \Gamma^{lk}_{ji} - p_i \sum_{lk} \Gamma^{lk}_{ij} \right) \tag{1.15}$$

which sums up the flows (population times rate) from all other states $|j\rangle$ to state $|i\rangle$, and subtracts those leaving $|i\rangle$ for $|j\rangle$, at all combinations of electrodes l, k. In this treatment, one neglects any eventual coherences due to short-lived superposition between the spin states. These would likely not be observable in our STM experiments, where current is continuously applied.[30,97] Together with the requirement $\sum_i p_i = 1$ we obtain a coupled system of ordinary linear differential equations whose solutions are the steady-state populations for a given bias voltage.

1.3.3 Electron spin resonance STM

The phenomenon of spin-flip tunnelling, as just introduced, allows initializing and reading out the electron spin of single molecules and atoms. This has been shown to enable storing and manipulating binary classical information in their magnetization direction.[98] To process quantum information, one must instead control superposition of quantum states. However, inelastic tunnelling is inherently quantum-incoherent, as each such event re-initializes the impurity's magnetization, destroying superposition.[30,97]

In spin qubits, coherent manipulation is made possible by the historically well established technique of magnetic resonance.[99] We will briefly re-state its principle.[17] An individual spin $S = 1/2$ in a static magnetic field $\mathbf{B}_0$ will experience a torque proportional to its gyromagnetic ratio $\gamma = g\mu_\mathrm{B}/\hbar$. If its vector of expectation values (the magnetization) forms an angle with the field, it will precess around it at its Larmor frequency $\omega_\mathrm{L} = 2\pi f_\mathrm{L} = \gamma B_0$. Interaction with the environment conversely tends to align $\langle\hat{\mathbf{S}}\rangle$ with $\mathbf{B}_0$. We choose a laboratory coordinate system with z along $\mathbf{B}_0$. The relaxation of the longitudinal (z) component towards its equilibrium value $\langle\hat{S}_z\rangle_0$ is phenomenologically captured by the time T_1. The decay of the transverse components (x, y) is parameterized by the generally shorter dephasing (decoherence) time T_2. The motion of the expectation value vector is given by the Bloch equations:

$$\begin{aligned}
\frac{\mathrm{d}}{\mathrm{d}t}\langle\hat{S}_x\rangle &= \gamma\big(\langle\hat{\mathbf{S}}\rangle \times \mathbf{B}\big)_x - \frac{\langle\hat{S}_x\rangle}{T_2} \\
\frac{\mathrm{d}}{\mathrm{d}t}\langle\hat{S}_y\rangle &= \gamma\big(\langle\hat{\mathbf{S}}\rangle \times \mathbf{B}\big)_y - \frac{\langle\hat{S}_y\rangle}{T_2} \\
\frac{\mathrm{d}}{\mathrm{d}t}\langle\hat{S}_z\rangle &= \gamma\big(\langle\hat{\mathbf{S}}\rangle \times \mathbf{B}\big)_z - \frac{\langle\hat{S}_z\rangle - \langle\hat{S}_z\rangle_0}{T_1}
\end{aligned} \tag{1.16}$$

Magnetic resonance can be observed with a small sinusoidal field $B_1 \ll B_0$ of frequency f applied orthogonally to $\mathbf{B}_0$. If its frequency matches f_L, the spin will undergo Rabi oscillation at the Rabi rate $\Omega = \gamma B_1$. Herein, the spin periodically inverts ("flops") while simultaneously precessing, giving a helical trajectory. This is shown for the dissipationless case $T_1 = T_2 = \infty$ in Figure 1.10a where we assume a single free electron such that the Hilbert space is represented by a Bloch sphere with poles $|-1/2\rangle$ and $|+1/2\rangle$. We now make the rotating wave approximation: the counter-rotating circularly polarized component of the linearly polarized field $\mathbf{B}_1$ is neglected. We can then define a rotating reference frame with x along $\mathbf{B}_1$ revolving about z at a rate f. In this frame, the dissipationless Rabi cycle corresponds to a simple circular motion on the meridian of the Bloch sphere's surface.

When the spin is allowed to exchange energy and phase with the environment via a finite T_1 and T_2, the Rabi flopping in no longer reversible. For $f \approx f_\mathrm{L}$, the Bloch vector will now instead tend towards a point within the Bloch sphere. When slowly sweeping through the resonance, we observe this steady-state point canting away from $|-1/2\rangle$ and dipping within

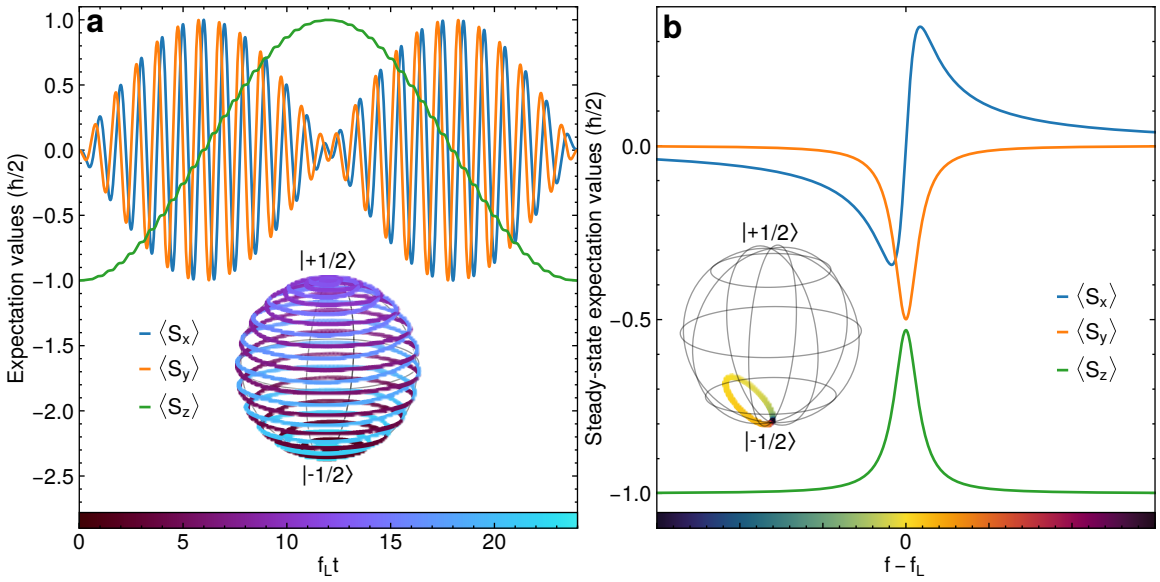

Figure 1.10: Single electron spin resonance. **(a)** Full Rabi cycle in the absence of relaxation and decoherence. Line plots show the time evolution of the spin expectation values; inset the trajectory on the Bloch sphere. **(b)** Steady-state magnetic resonance for finite $T_1 = T_2$. Curves and Bloch sphere path are shown as a function of frequency detuning.

the sphere, then returning.[100] For large B_1, the trajectory in the rotating reference frame always reaches the origin of the Bloch sphere - a phenomenon known as saturation. In this regime, increasing B_1 no longer enhances the signal and only leads to additional energy broadening.

To apply these concepts to single molecule or atoms in an STM junction, we require both a mechanism by which a transverse torque is exerted onto its spin (B_1) at radio frequencies, and a scheme with which the resulting change in magnetization can be read out. Crucially, B_1 needs to be sufficiently large to overcome T_1 and T_2 in order to observe such a signal. Baumann *et al.*[101], in 2015, were the first to successfully realize these requirements with a single-atom STM junction. The new technique, electron spin resonance STM (ESR-STM), has since become a vibrant area of research. It has enabled spectroscopy of magnetic nanostructures, single molecules and even nuclei with unprecedented energy resolution, as well as the implementation of quantum gates in single atoms. Comprehensive reviews of recent progress are given in references [102–105].

In the original ESR-STM arrangement, shown in Figure 1.11a, a single magnetic atom, spaced by a thin film of the insulator MgO from the metallic substrate, serves as a highly coherent quantum spin with sufficiently large T_1 and T_2. Due to the magnetic dipole selection rules, strong electron spin resonance (ESR) signals can only be observed between levels separated in angular momentum by $\pm\hbar$. This makes Ti/MgO, with $S = 1/2$, an ideal platform for ESR-STM which has been exploited numerously.[28,37–39,104,106–119] A spin-polarized tip is positioned above the magnetic atom under study and a constant external field B_0 is applied to obtain a Zeeman splitting. Such a tip is prepared by picking up individual mag-

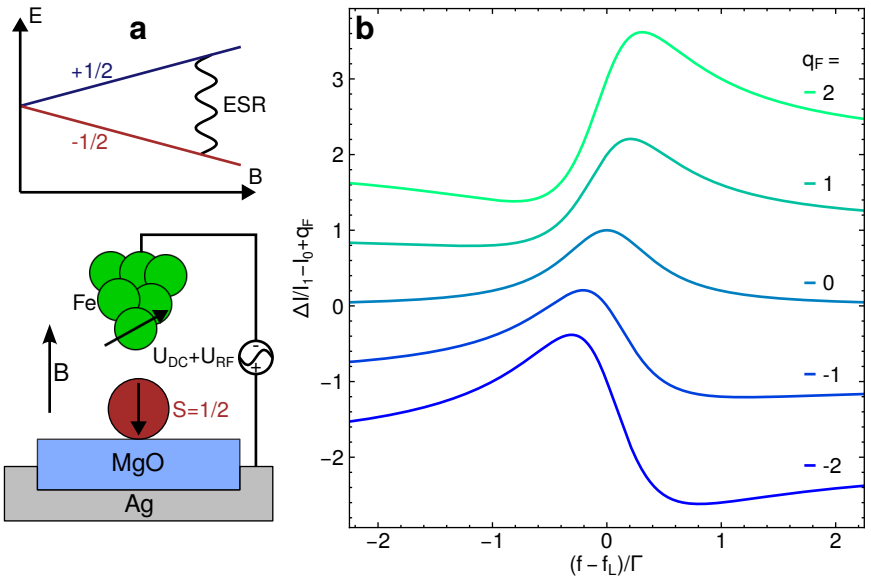

Figure 1.11: **(a)** The setup used for ESR-STM consists of a tunnelling junction formed between a spin-polarized tip and an atomic $S = 1/2$ decoupled by an insulator (here MgO). **(b)** The lineshape (Equation (1.17)) with varying asymmetry q_F. Curves are offset for clarity.

netic atoms off the surface, forming a cluster at the tip apex.[91,101] At low temperatures, this nanoparticle settles into a stable magnetization state, often forming an angle with B_0.[117,120] The degree of tip polarization can be assessed by IETS, as shown in Section 1.3.2. Finally, a radio frequency (RF) tone at frequency f is superimposed onto the usual DC tunnelling bias such that the junction voltage is $U = U_{DC} + U_{RF,J}$. Several mechanisms[101,102,115,120–128] can transduce this oscillating voltage to the AC magnetic field required to drive ESR. In the most widely accepted picture,[123] the tip spin is considered to be exchange-coupled to the atom under study.[108,129] The RF electric field, enhanced by the proximity of tip and surface, periodically distorts MgO piezoelectrically.[120] This vertically modulates the adatom's positions and thereby the exchange bias exerted by the tip.[129,130] If the polarization of the magnetic cluster is canted off-axis, an effective transverse field B_1 on the order of several mT[120] can be produced at the applied frequency f. In molecular systems, other driving mechanisms have been identified.[13,131]

As f is swept through f_L, magnetic resonance occurs and the atom's spin tilts away from B_0 in the rotating frame. The change in $\langle \hat{S}_z \rangle$ can be observed via the purely elastic tunnel magnetoconductance (Section 1.3.2) between the tip and atom, giving a change in current ΔI on the order of 100 fA. The transverse components rotate at a rate far beyond the detection bandwidth of STM. However, they also contribute to the magnetoconductive signal if the tip polarization has a transverse component. This occurs as a result of homodyne mixing of the RF bias voltage oscillating at f with the RF transverse magnetoconductance oscillating at f_L. The sign of the detected current depends on whether the beat frequency $f - f_L$ is positive or negative.[107,132] The resulting ESR-STM peak shape is a combination of the symmetric detection of the longitudinal change in magnetization and the asymmetric homodyne effect. It can be shown, by projecting the steady-state solution of the Bloch equations (Figure 1.10b)

onto the tip polarization, that the change in current follows[39,133]

$$\begin{aligned} \Delta I &= I_1 \frac{1 + q_F \epsilon}{1 + \epsilon^2} + I_0 \\ \epsilon &= \frac{f - f_L}{\Gamma/2} \\ \Gamma &= \frac{\sqrt{1 + \Omega^2 T_1 T_2}}{\pi T_2} \end{aligned} \tag{1.17}$$

This signal is equivalent in shape to a Fano resonance, as can be seen in Figure 1.11b. The peak amplitude and width depend on both T_1 and T_2. The asymmetry factor q_F is a measure of the angle that the tip polarization forms with $\mathbf{B}_0$. The scale factor I_1 depends, among others, on the Rabi frequency Ω and on the relative alignment of tip and adsorbate spins. I_0 is an offset stemming from RF rectification (Section 2.4). In the Lorentzian limit $q_F \to 0$, I_1 becomes equal to ΔI_{ESR}, the positive excursion of the peak. The Larmor frequency f_L can then be directly read out from the peak position.

Throughout this thesis, we will develop concepts relevant to implementing, and extending upon, the ESR-STM technique. In Section 2.2, we explore how the STM tip can be made spin-polarized by picking up single atoms. In Section 2.3, we modify a low temperature STM (LT-STM) to deliver microwave signals to the tunnelling junction. Section 2.4 detail how the amplitude and photon energy of this radiation is quantified in-situ. Chapter 4 provides new insight into the electronic decoupling effect of MgO. Finally, we demonstrate quantum coherence in our STM by performing magnetic resonance on a single titanium atom in Section 5.1. Lastly, we motivate further experiments Section 5.2 by studying the application of an electron nuclear double resonance (ENDOR) scheme to ESR-STM.

1.3.4 Atomic and Kelvin-probe force microscopy

Finally, we will briefly introduce the concept of force microscopy, which can probe mechanical and electrostatic interactions at the intramolecular scale. At nanoscopic separations d from a surface, an atomically sharp tip experiences a force:

$$F(d, U) = -\left.\frac{dV_{LJ}(z)}{dz}\right|_d - \frac{1}{2}\left.\frac{dC(z)}{dz}\right|_d (\mathrm{LCPD} - U)^2 \tag{1.18}$$

where the first term stems from the Lennard-Jones potential $V_{LJ}(z)$, shown in Figure 1.12a, which models interatomic attraction at large distances and and repulsion at close distances. The second term arises from the electrostatic energy stored on the tip-surface capacitance $C(z)$ by the potential difference across it. We will ignore it for now.

If the tip is mounted to a flexible cantilever with spring constant k, its bending moment balances F and leads to a stable deflection towards d. Due to the presence of the tip-surface force, a small amplitude harmonic oscillation around d will be shifted from its natural frequency f_0 by

$$\Delta f\,(d) = -\frac{f_0}{2k}\frac{\partial F(d, U)}{\partial d}. \tag{1.19}$$

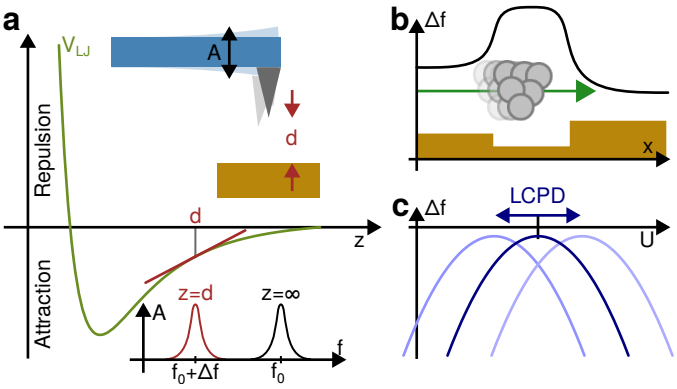

Figure 1.12: Frequency-modulated force microscopy. **(a)** The tip on a cantilever sees an attractive force, which modifies its resonance frequency by Δf. **(b)** In CH mode, Δf reproduces surface topography. **(c)** With a bias voltage, $\Delta f(U)$ forms a parabola. Its vertex reflects the sample's local work function.

This forms the basis of the frequency-modulated atomic force microscope (AFM), in which the cantilever is always excited at its resonant frequency $f_0 + \Delta f$, and Δf recorded. The oscillation amplitude A is kept constant by a second feedback loop. In a CH frequency shift scan, one images the force gradient $\partial F(d, U)/\partial d$, which is highly dependent on d, and therefore provides topographic information as sketched in Figure 1.12b. In our experiments, we use the qPlus sensor, which combines the functionality of STM and AFM in a single probe.[134] The highest spatial resolution can be obtained by attaching a single upright CO molecule to the tip at low temperatures. When d is lowered to lie within the repulsive regime, its orientation can be tilted by the local electron density. This results in a sharp peak in Δf when scanning over chemical bonds.[135] We will use this bond-resolved technique to image the chemical structure of nanographenes.

The second term in Equation (1.18) also leads to a frequency shift via Equation (1.19). Its magnitude depends on the applied bias voltage U, and the local contact potential difference (LCPD), which arises from unequal tip and local sample work functions. If the bias voltage precisely equals the LCPD, the junction is said to be compensated and Δf derives purely from the interatomic potential. Away from this point, the cantilever frequency decreases parabolically with U, as seen in Figure 1.12c. By recording such curves over a 2D grid at constant height, the LCPD can be determined from the parabolas' vertices.[136] The LCPD signal is highly sensitive to the presence of local charges, which alter the surface work function.[86]

Chapter 2

Experimental methods

In this chapter, we describe the practical aspects of investigating the spin of single atoms and molecules. This includes the preparation of substrates to be studied in the STM, deposition and manipulation of the adsorbates under study, how RF signals are brought to the tunnel junction and characterized, and how to detect the ESR-STM signal.

2.1 Single atoms and molecules on functional substrates

Accessing the single molecule level with the STM level requires atomically clean surfaces. This is achieved by placing the LT-STM within an ultra-high vacuum (UHV) environment. Due to the extremely low pressures below 1×10^{-9} mbar, pristine surfaces can be prepared in the same vacuum chamber, transferred to the microscope and imaged indefinitely without contamination.[137] All experiments are conducted on metallic single crystals. Their surfaces are polished to the nanometer level, but are not atomically flat and contaminated by air molecules. Once introduced into UHV, we cyclically expose them to an accelerated ion beam (Ar^+, Ne^+ or Xe^+ at ≈ 2 keV) followed by heating to temperatures within two thirds of their melting point. The first step leads to sputtering of several atomic layers, revealing the pure substrate.[138] The annealing step allows diffusion and the formation of large terraces bordered by atomic steps,[139] as shown in Figure 2.1. Once this is achieved, a thin functional

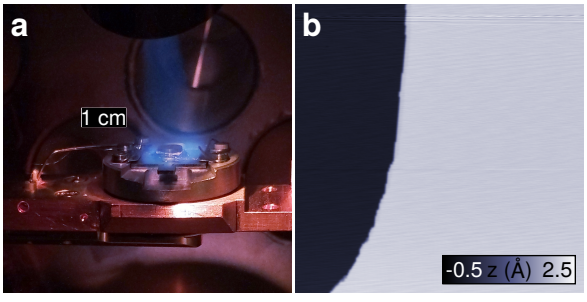

Figure 2.1: Preparation of atomically clean metal surfaces in UHV. **(a)** Long-exposure photograph of a Xe^+ plasma beam accelerated towards the Ag(100) single crystal in the centre. **(b)** After annealing, the surface shows wide, featureless terraces and undecorated monoatomic steps. $60 \times 60\,nm^2$, 100 mV, 20 pA.

surface can be synthesized epitaxially. In this thesis, we study the rare-earth intermetallic compound $GdAu_2$ and the insulator MgO. We will cover here the practical aspects of their growth. We also describe how single atoms and molecules are deposited on top of these layers.

Preparation of $GdAu_2$

At elevated temperatures, the intermetallic lattice of $GdAu_2$ has been shown to form directly on the Au(111) surface upon adsorption of a submonolayer of Gd.[140] In our experiment, we hold the single crystal at a temperature between 250 to 300 °C, as measured by an infrared pyrometer, and expose it to a beam of Gd for approximately 15 min. The latter is obtained by electron-beam evaporation from a solidified Gd droplet contained in a tungsten crucible. We find it essential to degas the Gd source above its melting point for several hours to rid it of gettered contaminants. After evaporation, the crystal is let to cool off naturally. This process gives a uniform surface coverage of Gd. We find that with a subsequent annealing step to a similar temperature as that used during growth, one recovers patches of bare Au(111). The structure and properties of $GdAu_2$ will be discussed further in Chapter 3.

Preparation of MgO islands

To form an epitaxial film MgO atop a metallic substrate, we require the stoichiometric reaction of Mg and O. For our experiments, it must also be thin enough to allow electrons to tunnel through. Additionally, we seek a growth mode in which few but extended and defect-free islands are separated by stretches of bare metal, which is essential for preparing the STM tip. Such ultrathin MgO films have been prepared by sublimation of Mg, under a small atmosphere of O_2, onto heated Ag(100) which closely matches the lattice constant of the oxide's rocksalt structure.[141–155] We find the growth mode to be highly dependent on the combination of Mg sublimation rate, substrate temperature and oxygen pressure. Overall, the best results are achieved at moderate growth rates, intermediate to high temperatures and large oxygen pressures. The sample prepared in Section 4.1 was exposed to Mg flux for 3 min at a measured temperature of 410 °C and an oxygen pressure of 1×10^{-6} mbar. In Section 2.2 and Section 4.2, the duration was 5 min at 365 °C and 5×10^{-6} mbar. In Section 4.3 and Section 5.1, we sublimated for 3 min at 390 °C and 5×10^{-6} mbar. After the Mg beam is interrupted, we maintain the same sample temperature for 10 min. This post-annealing has been found to reduce the number of defects.[156] We then slowly cool the crystal to room temperature by regulating the heater power over a time period of 30 min, which was also found to improve film quality.[153]

The island thickness is the most crucial property of our films as it dictates the separation of a molecular adsorbate to the underlying metal. MgO typically occurs either as a monoatomic layer, or in a bilayer (i.e. one unit cell). Distinguishing between them proves difficult for two reasons: both types can grow embedded into the Ag(100) substrate, and MgO modifies the tunnel barrier, falsifying the topographic contrast in STM.[152] MgO bilayers, but not monolayers, exhibit a characteristic pair of surface states localized to the top and bottom faces, respectively, that allows their differentiation by STS. At tunnel bias voltages below

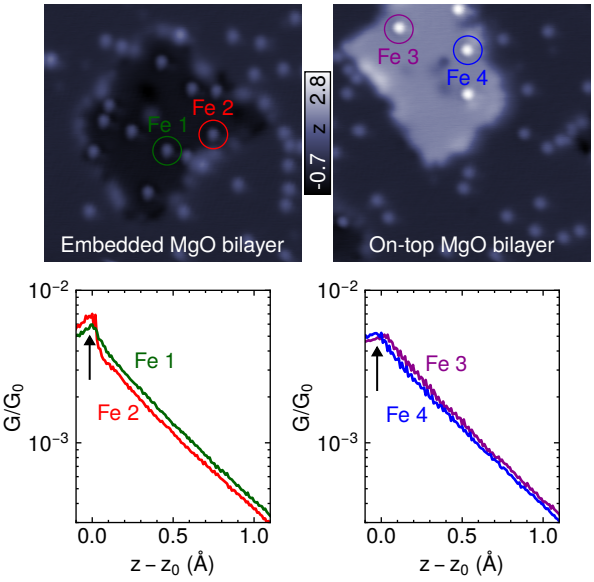

Figure 2.2: Measuring the tunnel conductance of MgO islands to determine their thickness. Top row: STM scans showing embedded (left) and on-top (right) MgO patches surrounded by Ag(100) and covered with Fe atoms. Bottom row shows conductance as a function of tip displacement, which rises exponentially until mechanical contact is formed between the adatoms indicated above by circles and the tip at $z = z_0$. Scan parameters: $15 \times 15\,\mathrm{nm}^2$, 100 mV, 20 pA. Approach curves taken at 10 mV.

these states ($U < 1$ V), MgO possesses no DOS and electrons tunnel directly to the interface formed with silver. In topographic scans, embedded bilayer (and monolayer) patches then appear darker than the surrounding metal, while on-top islands seem elevated compared to Ag due to the lowered tunnel barrier. Paul *et al.*[29] developed a method with which the thickness is determined independently. By bringing the STM tip into direct contact with single atoms (e.g. Fe) adsorbed on MgO, one can measure the tunnel resistance through the layer directly. Its value increases exponentially with the MgO thickness and allows direct comparison. As illustrated in Figure 2.2, both "bright" and "dark" bilayer islands are revealed by this method to be of the same thickness, but only the former is embedded into Ag. In all experiments except Section 4.1, we investigate bilayer islands of MgO.

In-situ deposition of single atoms onto MgO

Adatoms are highly mobile at room temperature and readily assemble into clusters.[157] To study their properties in isolation, their diffusion must be suppressed by lowering the temperature. In a LT-STM, one can directly expose the sample thermalized to cryogenic temperatures to atomic or molecular beams. Ti and Fe are sublimated from pellets in a Mo crucible and a solid rod, respectively, by electron beam heating. Opening a specially designed mechanism within the heat shields[158] for several seconds allows the atomic beam to reach the sample. The flux is quantified by recording the electric current between the sample and ground that compensates the ionized fraction. In-situ sublimation results in randomly distributed isolated Fe and Ti atoms across both Ag and MgO, as shown in Figure 2.2, Figure 2.4 and others.

In-situ sublimation of molecules

Due to the small sublimation enthalpy of metallocenes at room temperature[159] and thereby large vapour pressure, these molecules requires cryogenic temperatures for stable physisorp-

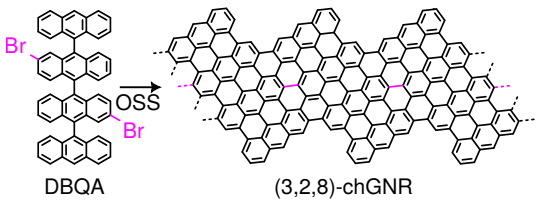

Figure 2.3: Scheme of the on-surface reaction of the 2',3"-dibromo-quateranthracene precursor to form a $(3, 2, 8)$-chGNR. Ullman coupling occurs at the sites marked in pink.

tion in UHV. We achieve this by exposing the single crystal in-situ to a molecular beam from a room-temperature Knudsen cell for several minutes.[160] The flux is controlled by placing a constriction on the opening of its quartz crucible. As metallocenes do not stick to the ambient temperature UHV chamber walls, the vacuum pressure is a good indication of the flux. Adsorption of tetrapyrroles onto MgO/Ag(100) as shown in Section 4.2 and Section 4.3 also requires in-situ sublimation to prevent their diffusion off the insulator. This is done identically to metallocenes, but from a heated crucible facing the cryogenically cooled sample surface.

On-surface synthesis of chiral graphene nanoribbons

ChGNRs are synthesized from specifically designed brominated quateranthracene molecular precursors[50] via on-surface synthesis,[161] as shown in Figure 2.3. They are deposited, by sublimation from powder form in quartz Knudsen cells at 300 to 320 °C, onto room-temperature single crystal surfaces. Here, we employ Au(111), covered with $GdAu_2$ and Ag(100), with MgO patches. Heating to a moderate temperature leads to the Ullmann coupling at the bromine sites via the catalytic action of the metallic substrate. The positioning of Br determines the chiral vector of the nanoribbons. We denote their length L by the number of precursor unit needed to form them. In a second heating step, cyclodehydrogenation occurs, closing all six-membered rings. In Section 3.1, 240 °C is held for 20 min, then 360 °C for 10 min. In Section 4.1, 200 °C for 20 min, and 300 °C for 10 min.

2.2 Atomic and molecular manipulation

To sense the magnetization of a single atom or molecule by tunnelling, one requires a spin-polarized electrode, as introduced above. However, a tip made of a bulk magnetic material will often lead to large dipolar stray fields at the nanoscale and offers little in-situ tunability.[93] Loth *et al.*[94] succeeded in producing a tip polarization by functionalizing an otherwise nonmagnetic Ag-coated tungsten tip by vertical manipulation of individual atoms.[162] The mechanical action can be understood as a combination of the intermolecular pair potential between tip apex and adsorbate,[163] and the inelastic excitation of desorption through the voltage bias.[164] A cluster of few iron atoms makes up a nanoparticle with significant magnetic anisotropy. At low temperatures and/or an external field, a stable magnetization is formed.[117] Here, we briefly show how this is achieved practically, following the procedure of Baumann *et al.*[101].

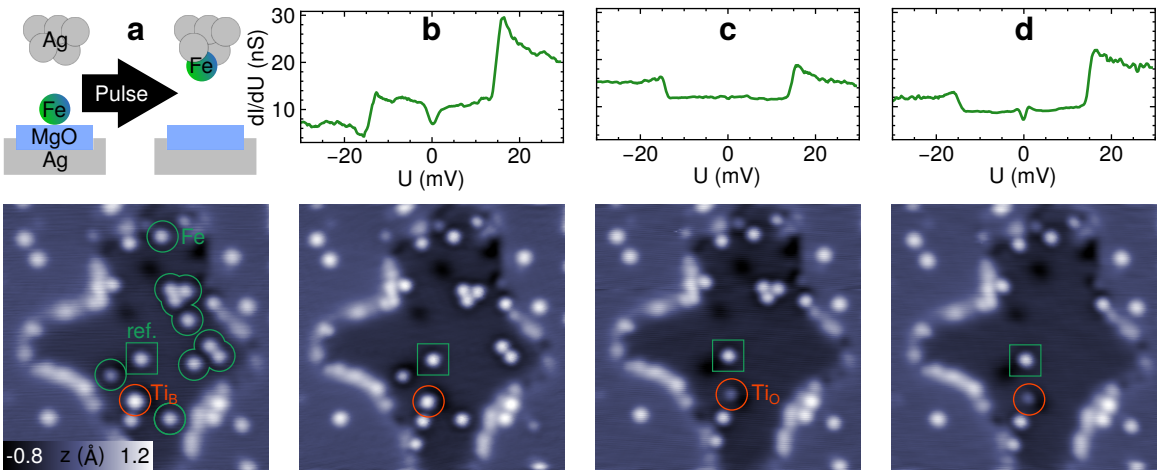

Figure 2.4: Tip polarization by vertical manipulation of Fe atoms on MgO/Ag(100). Scheme **(a)** shows the pick-up process. Below, topographic scans of Fe and Ti atoms naturally adsorbed on a MgO bilayer (13 × 13 nm^2, 100 mV, 15 pA.). In columns **(b-d)**, nine Fe atoms are picked up successfully, see scans in the bottom row. In the top row, inelastic tunnelling spectra taken on the reference Fe atom (green square) show the evolution of spin polarization throughout the process. The titanium atom marked in red is inadvertently pushed to an alternate adsorption site. An out of-plane-field on the order of 0.5 T is applied.

Figure 2.4 shows a cross-shaped bilayer island of MgO embedded into Ag(100). Individual Fe (green) and Ti (red) atoms have also been sublimated. Starting from a sharp Ag-coated tip, prepared by controlled contact formation with the substrate, individual Fe atoms are picked up. This is done by approaching the tip towards the atom down to a junction resistance of several MΩ and applying a voltage pulse on the order of 500 mV. The reverse process is also possible by applying a negative voltage pulse[3]. The successful transfer to the tip apex manifests in two ways. For one, the image contrast is typically enhanced as expected for a single-atom apex. Second, with several (usually more than three) iron atoms picked up, spin-polarized tunnelling starts to manifest in conductance spectra. For small polarizations, we obtain an asymmetry of the inelastic conductance steps of Fe/MgO. At larger polarizations, spin pumping occurs, as described in Section 1.3.2. The evolution of the tip polarization with the number of atoms is not monotonous. In fact, the three additional Fe atoms picked up in Figure 2.4c decreased the already substantial tip magnetization of Figure 2.4b.

We will also employ the vertical manipulation mode to transfer single CO (Section 3.1) and metallocene molecules (Section 3.2) to the tip. Larger molecules, such as chGNRs, cannot be desorbed as a whole. Instead, they must be dragged[156,165] and/or lifted.[166] For this, the tip is approached close enough to attract part of the molecule, and the slowly moved towards the desired position. During this process, the tunnelling current (or z) will show characteristic jumps that correspond to the atomic corrugation of the surface.[163] This technique is employed in Section 3.1 and Section 4.1.

2.3 radio frequency upgrade of a scanning tunnelling microscope

Quantum-coherent measurements on individual spin qubits in the STM require relatively large driving signals of several mV in the GHz range to be introduced to the tunnelling junction. This is not possible in most LT-STM setups, where wiring has typically been designed to specifically filter out RF radiation.[167] Here, we upgrade a commercial instrument with such capability by adding in a custom-made coaxial transmission line (coax) to the microscope, similar to the work of others.[111,168–174] Over its length of approximately 2 m, the cable must transition from ambient conditions at the RF source to cryogenic temperatures at UHV pressures in the mechanically decoupled microscope. In this section, we outline how the stringent thermal, electrical and mechanical requirements are satisfied in our design.

The fundamental challenge in bringing RF signals to a low-temperature STM is that the tunnelling junction presents a large input impedance, in the range of tens of kΩ to several TΩ. Since coax has a standard characteristic impedance of 50 Ω, this means almost all of the introduced RF power gets reflected at the tunnelling junction. If an additional impedance mismatch is present along the cable, a standing wave forms within that section. Transmission will be strongly suppressed for multiples of a resonant wavelength, which is known as frequency-domain ripple.[175]

One practical difficulty is making the connection to the tunnelling junction within the actual microscope. Peters *et al.*[176] pioneered the use of a stripped coaxial cable, which capacitively couples to the STM junction similarly to an antenna. This reduces complexity since one does not need to guide the cable through the piezo motor assembly, while giving similar performance to a direct connection. We have followed this approach.

The setup we upgraded with RF capabilities, the JT-SPM as sold by Specs GmbH, is shown schematically in Figure 2.5. The cryostat is fully contained within the UHV chamber held by a frame equipped with pneumatic isolators. The latter is placed on a several ton heavy similarly isolated concrete block. The STM itself is suspended by springs from the bottom of the cryostat. This construction greatly lowers the coupling of building vibrations to the STM. Low temperatures are achieved with a cylindrical bath of liquid helium (boiling point 4.2 K) surrounded by another vessel filled with liquid nitrogen (77 K). The LHe reservoir is protected from thermal radiation by baffles B1 to B3 cooled by the gaseous He exhaust. A third volume is mounted to the bottom of the LHe tank. Here, pressurized helium gas is cooled via the Joule-Thomson effect. The vapour of the resulting liquid is continuously pumped away to achieve temperatures on the order of 1 K, cooling the STM to a base temperature below 1.3 K. A superconducting magnet encloses the microscope unit, providing a vertical magnetic field of 3 T.[158]

The coaxial feedline from the RF generator to the antenna termination is subject to several mutually conflicting constraints. We require:

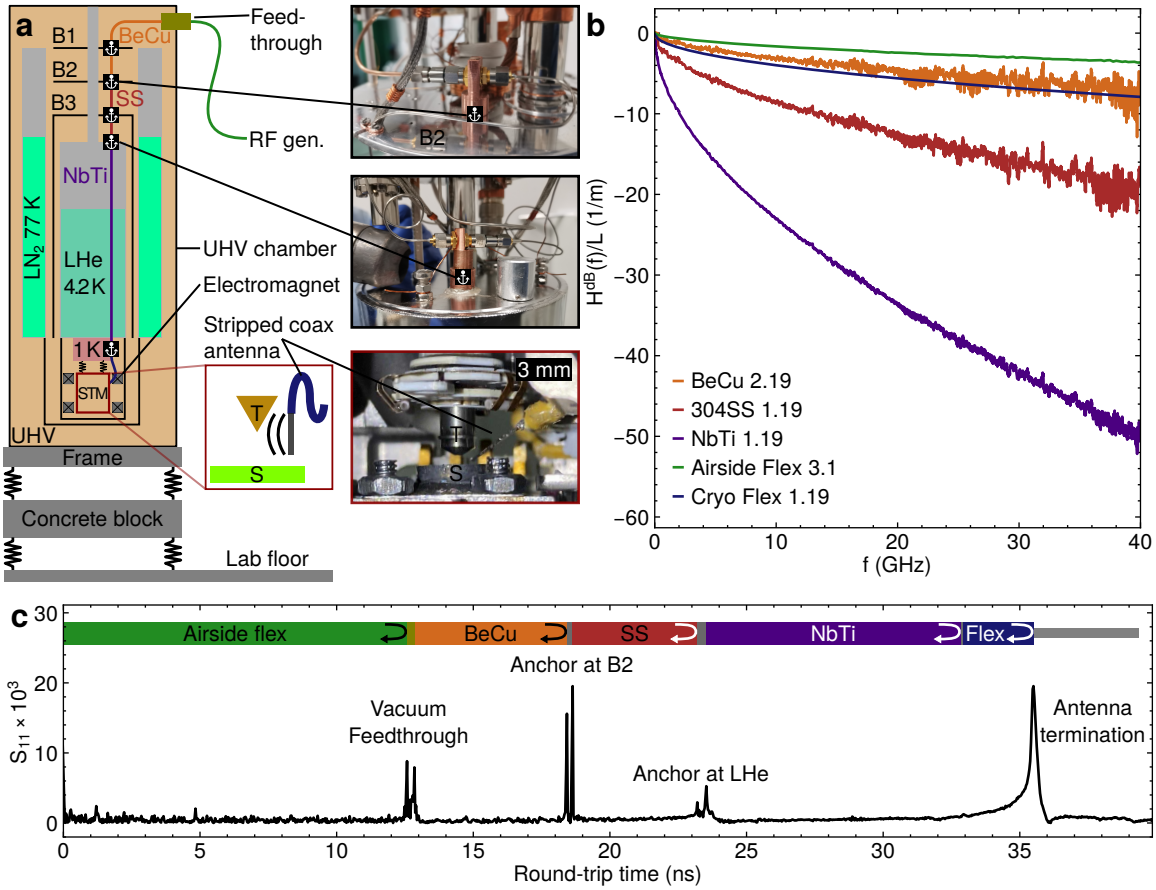

Figure 2.5: **(a)** Simplified cross section of the LT-STM setup with RF capability we developed. See text for details. Photographs show the two coax thermal anchoring points and the stripped coax antenna near the tip-sample (T-S) junction. **(b)** transfer functions $U_{\mathrm{out}}/U_{\mathrm{in}}$ of the coaxial cable assemblies as received measured at room temperature. The curves are coloured according to the diagram. The last trace is an empirical fit given by the manufacturer. **(c)** Time-domain impulse reflectometry of the feedline. We assign each reflection to impedance discontinuities of RF connectors and the antenna termination.

1. Small signal attenuation to allow operation at small input powers, minimizing heat load. RF signals decay exponentially in transmission lines due to resistivity and dielectric loss.[175] Short lengths of large-diameter semi-rigid coax composed of low-resistance materials such as copper are therefore best suited for this requirement.
2. Low thermal conduction through the coax. This is best achieved by coiling large lengths of small-diameter coax made of high thermal resistance materials such as stainless steel.
3. Small frequency-domain ripple. This necessitates using as large as possible bend radii and as few as possible RF adapters between cable sections.
4. A large operating frequency range. This is limited by the cable's cut-off frequency, which scales inversely with its radius.[175]
5. Mechanical complacency, to not allow vibrations to bypass the seismic isolation measures in place. This favours thin and flexible coax.
6. The UHV environment not to be compromised. In particular, a hermetic vacuum feedthrough is required to interface with the airside section. All parts also need to have negligible outgassing. This is possible with a PTFE dielectric.

Since these requirements are difficult to fulfil by a single cable, we construct our feedline from staggered sections of flexible and semirigid coax (Coax Co., Ltd.) of different dimensions and materials joined with 2.92 mm series SMA-type connectors, which allow for operation up to 40 GHz. Semirigid cable has superior RF performance, whereas flexible cable allows for mechanical decoupling. At several positions, the cable is thermalized to minimize the heat load between successive temperature stages.

A 50 cm section of flexible cable of diameter 3.1 mm (Koaxis) links the RF generator to the vacuum feedthrough (Allectra GmbH). A narrow gauge is chosen to not transmit vibrations. The first semirigid in-vacuo section is placed between the feedthrough and baffle B2. This 60 cm stretch experiences the most significant temperature difference, which is maintained here by the nitrogen reservoir and helium exhaust. Since the available cooling power is large, we can choose a diameter of 2.19 mm to enhance transmission. Silver-plated BeCu coax performs as well as pure Cu electrically, but has a smaller thermal conductance and can block some of the parasitic heat flow from the feedthrough.

From baffle B2 onwards, we run a 50 cm segment of 1.19 mm diameter stainless steel (type 304) semirigid coax. This material has a very small thermal conductivity, which minimizes the parasitic influx of heat at the expense of increased RF attenuation. To ensure temperature equalization of the feedline with the surroundings, we mount two additional thermal anchors using bolts and heat-conductive epoxy (Epotek GmbH) at B2 and on top of the LHe tank. Female-female bulkhead adapters provide a solid contact for thermalization. The photographs in Figure 2.5 also show attenuators which improve thermal contact to the inner conductor;[171] these were later removed for increased transmission.

The last section of semirigid coax runs through a tube in the LHe tank up to the 1 K pot.

The latter has a small cooling power and needs to be thermally isolated from the LHe reservoir above. A 1 m long 1.19 mm superconducting NbTi segment is perfectly suited. Below a transition temperature of $\approx$ 10 K,[177] its purely phononic thermal conductivity is negligible,[178] and neither does it resistively attenuate RF. Thermal anchoring at the LHe reservoir and good contact with the liquid ensures this segment remains superconducting.

The last connection is a flexible 1.19 mm normal metal coax (Samtec) of $\approx$ 20 cm length anchored at the 1 K pot. For maximum vibration isolation, we remove its jacket and shape it into a meander to act as a spring between the cryostat and microscope. From the same cable, we fashion the antenna termination by simply cutting away the outer conductor and dielectric. The stripped section is made as short as possible, but long enough to come close to the tip-sample junction. It is held in place by two-component adhesive (Loctite) to suppress acoustic modes. It is positioned such that samples and tips of different dimensions can be used. We place a DC block (Pasternack) at the RF generator output to protect it in the unlikely event of the antenna coming into contact with the DC-biased sample.

The feedline performance at cryogenic temperature can be assessed by time domain reflectometry. To this end, the signal returned to the feedthrough U_{ret} is measured, and thereby the reflection coefficient $S_{11} = U_{\mathrm{ret}}/U_{\mathrm{in}}$. A broadband frequency domain trace thereof, obtained using a vector network analyser, can then be Fourier transformed into the time domain. This simulates the transient response to sending a sharp pulse down the cable. The result is shown in Figure 2.5c. As expected, due to the large impedance mismatch, the signal is rejected by the antenna termination and returns to the source after travelling down and up the line for approximately 35 ns. During this round trip, significant signal is lost, hence why S_{11} only amounts to a few percent of the excitation signal. We observe further reflections, whose spacing perfectly coincides with the length of the interconnected coaxial cable segments. Due to their spatial extension, each RF connector produces two tightly spaced reflections, corresponding to its two mating interfaces. It is important to remember that due to signal loss, these peak amplitudes are to be weighed exponentially with increasing travel time. Consequently, the reflection at the interface between stainless steel and NbTi segments is much more severe than that at the vacuum feedthrough. This is also why the reflection between NbTi and the second flexible cable is not registered.

2.4 Quantifying radio frequency transmission

While feedline losses can be compensated by increasing the RF power, it is the frequency-domain ripple introduced by impedance mismatches and imperfect antenna coupling to the tip that presents a challenge for RF measurements in the STM. Due to the non-ohmic nature of tunnelling, RF voltages are partly rectified and give significant DC offsets ΔI in current. Since the transmission to the junction strongly depends on frequency, so does the rectification current. In an ESR-STM experiment, one must therefore disentangle these transmission artefacts from actual magnetic resonance peaks. This is done by measuring the transfer function (TF) between the RF generator and the tunnelling junction. One can then compensate

for ripple by adjusting the RF source amplitude at each frequency in accordance with the TF such that the RF amplitude in the junction remains constant.

The TF is defined as $H(f) = U_{\mathrm{RF,J}}/U_{\mathrm{RF,0}}$ and relates the zero-to-peak voltage amplitude in the junction $U_{\mathrm{RF,J}}$ to that supplied by the RF source $U_{\mathrm{RF,0}}$. When expressed in decibels as $H^{\mathrm{dB}}(f) = 20\log_{10} H(f)$, we can decompose it into two parts:

$$H^{\mathrm{dB}}(f) = H^{\mathrm{dB}}_{\mathrm{FL}}(f) + H^{\mathrm{dB}}_{\mathrm{AJ}}(f) \tag{2.1}$$

The first term is the TF of the feedline up to the antenna; the second part describes its capacitive coupling to the tip-sample junction. Measured TFs of the individual feedline sections at room temperature are shown in Figure 2.5. We can estimate $H^{\mathrm{dB}}_{\mathrm{FL}}(f)$ at 20 GHz to be no higher than −15 dB (neglecting the superconducting coax). The ripple of $H^{\mathrm{dB}}_{\mathrm{FL}}(f)$ lies below 3 dB in this frequency range.

The RF amplitude $U_{\mathrm{RF,J}}$ can be obtained by exploiting inelastic tunnelling. As we have seen, this phenomenon gives rise to differential conductance steps, which are non-linearities in the tunnelling current $I(U)$ in the form of kinks. We will now combine the RF with the usual DC bias voltage, such that $U(t) = U_{\mathrm{DC}} + U_{\mathrm{RF,J}}\sin(2\pi f t)$. This occurs naturally in our antenna setup via the in-situ capacitive coupling. If one records a $\mathrm{d}I/\mathrm{d}U$ trace under these conditions, the small detection bandwidth of STM averages the signal in the interval $U_{\mathrm{DC}} \pm U_{\mathrm{RF,J}}$ out. Therefore, the step is broadened and eventually replicated, giving two steps.[179] The voltage spacing of the two corresponding maxima in $\mathrm{d}^2I/\mathrm{d}U^2$ equals[4] $2U_{\mathrm{RF,J}}$. This is shown in Figure 2.6a, where we have positioned the tip above a titanium atom adsorbed to the oxygen site of the MgO/Ag(100) surface, which exhibits a large conductance step at bias voltages ranging from −60 to −80 mV.[28] The same measurement can be carried out using any non-linear current-voltage curve, provided the features are sufficiently sharp, step-like, and located at voltages much larger than $U_{\mathrm{RF,J}}$. Since the applied amplitude $U_{\mathrm{RF,0}}$ is known, the TF at this frequency is determined. Since we require $H(f)$ over a wide frequency band with high resolution, it its not feasible to measure $U_{\mathrm{RF,J}}$ at each frequency using this method.

Paul *et al.*[179] devised of an efficient scheme that makes use of another consequence of non-linearities. Consider a current-voltage characteristic like that shown in the inset of Figure 2.6b with two kinks. With the DC bias tuned to one of the non-linearities and $U_{\mathrm{RF,J}} = 0$, only the expected current $I_{\mathrm{DC}}(U_{\mathrm{DC}})$ is measured. With an added RF voltage, the resulting RF current does not oscillate around I_{DC}, but produces an additional offset ΔI called the rectification current. It occurs as during the positive half-cycle of the RF voltage the differential conductance is larger than during the negative half-cycle. Since the fast RF current is averaged out, we observe ΔI as an offset in the tunnelling current when RF is applied. It is lock-in detected by chopping the RF voltage, as will be described in Section 2.5.

Since $\Delta I(U_{\mathrm{RF,0}})$ is a bijective function, one can determine $U_{\mathrm{RF,0}}$ from ΔI by evaluating the polynomial fit $S(\Delta I)$ shown in Figure 2.6b. At the same frequency, $U_{\mathrm{RF,0}}$ obtained in this way is then referred to $U_{\mathrm{RF,J}}$ by multiplying with a calibration factor $C = U_{\mathrm{RF,J}}/U_{\mathrm{RF,0}}$ that results from the spectroscopic method shown in Figure 2.6a. In a frequency-swept measurement of the rectification current, where $U_{\mathrm{RF,0}}$ is held constant, this procedure allows

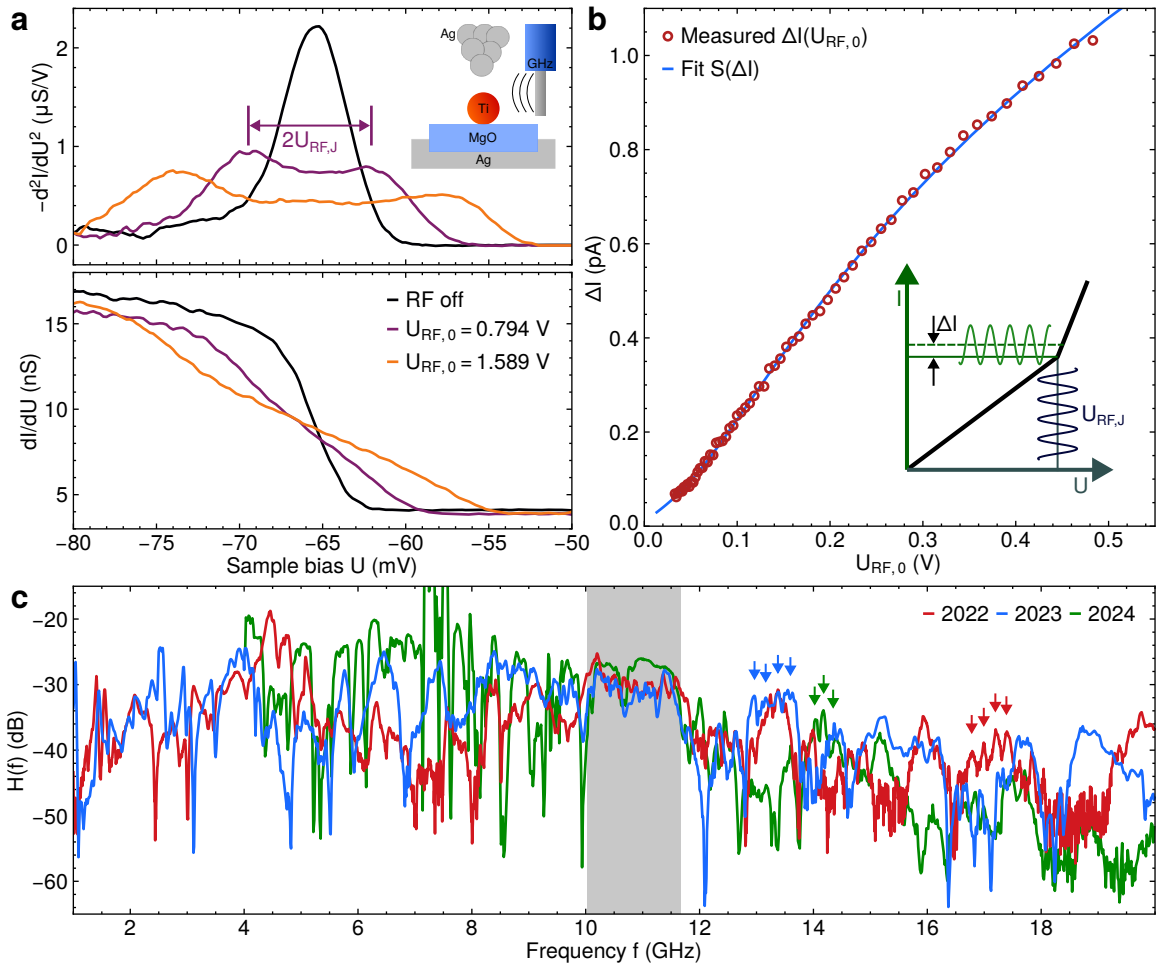

Figure 2.6: Measurement of the RF transfer function using inelastic tunnelling features. **(a)** shows the effect of RF emitted from the antenna on the conductance step of Ti_O/MgO/Ag(100) for two amplitudes. Top inset shows the experimental setup. Bottom panel shows $\mathrm{d}I/\mathrm{d}U$, top panel $\mathrm{d}^2I/\mathrm{d}U^2$. **(b)** Extraction of the function $f(\Delta I)$ by measuring the rectified current, here using Fe/MgO/Ag(100). Inset sketch shows the applied voltages and measured currents on the inelastic $I-U$ curve. Setpoint 100 pA, 15 mV. **(c)** evolution of $H^{\mathrm{dB}}(f)$ throughout maintenance periods.

the TF to be calculated directly as:

$$H(f) = C \cdot S(\Delta I(f))/U_{\mathrm{RF},0} \tag{2.2}$$

whereby C has to be determined only at one frequency: the same at which $S(\Delta I)$ was fitted to the measurement $\Delta I(U_{\mathrm{RF},0})$. For each f, only one data point needs to be recorded which allows for high-resolution characterization of the TF in reasonable time. Once the TF is known, the RF generator power can be varied to compensate for ripple. To have a constant RF amplitude $U_{\mathrm{RF,J}}$, the now frequency-dependent generator power must be

$$P_0(f) = \frac{U_{\mathrm{RF,J}}^2}{2Z_0 H(f)^2} \tag{2.3}$$

where $Z_0 = 50\,\Omega$ is the RF source's output impedance. One should now measure $\Delta I(f)$ under the same conditions as before to be a flat line. Usually, some small residual excursions occur. These are corrected by again applying Equation (2.2) with $U_{\mathrm{RF},0}(f) = \sqrt{2Z_0 P_0(f)}$ to obtain a new TF. In this iterative procedure, the ripple in $\Delta I(f)$ can be compensated to be far smaller than the typical height of an ESR-STM peak.

Figure 2.6c shows three TF measurements in the system we upgraded, at different points in time, from 1 to 20 GHz. Its average value is −30 dB below 12 GHz, where it rolls off to −45 dB up to 20 GHz. More than 90 % of the generated RF voltage is lost on its way to the junction, as in other setups.[111,168–174] We have estimated the feedline attenuation to be $H_{\mathrm{FL}}^{\mathrm{dB}} \approx -15\,\mathrm{dB}$ at 20 GHz. Therefore, the antenna-junction coupling dominates the signal loss with $H_{\mathrm{AJ}}^{\mathrm{dB}} \approx -30\,\mathrm{dB}$.

During unrelated maintenance on the microscope, the antenna termination was modified several times to be positioned closer to the STM junction. The remainder of the feedline was left as installed. This seems to have improved transmission below 10 GHz, but also has exacerbated the quantity and depth of sharp resonances where virtually no RF reaches the junction. These changes must derive from $H_{\mathrm{AJ}}^{\mathrm{dB}}(f)$ alone.

The frequency-domain ripple above 10 GHz, indicated by arrows, occurs in all measurements. Its spacing of 250 MHz indicates a reflection period on the order of $\approx$ 8 ns.[175,180] From the time domain reflectometry measurements presented previously, we can attribute this to the NbTi coaxial cable, which forms cavity modes in which signal repeatedly bounces back and forth between the connectors and/or the antenna termination.

From 10 to 12 GHz, ripple is minimal at 6 dB. The largest attenuation in this interval is at 10.5 GHz with −35 dB. Since the generator output is limited to $U_{\mathrm{RF},0} = 2.3\,\mathrm{V}$, we can perform constant amplitude RF sweeps up to $U_{\mathrm{RF,J}} = 40\,\mathrm{mV}$ in this range, sufficient to observe magnetic resonance. In Chapter 5, we will use this range (marked in Figure 2.6c) as our primary measurement window for ESR-STM. Detection of $U_{\mathrm{RF,J}}$ using tunnelling nonlinearities fails when the rectification current falls below the noise floor of the measurement (50 fA in Figure 2.6), which makes correct reproduction of deep antiresonances in the TF such as that at 12 GHz challenging.

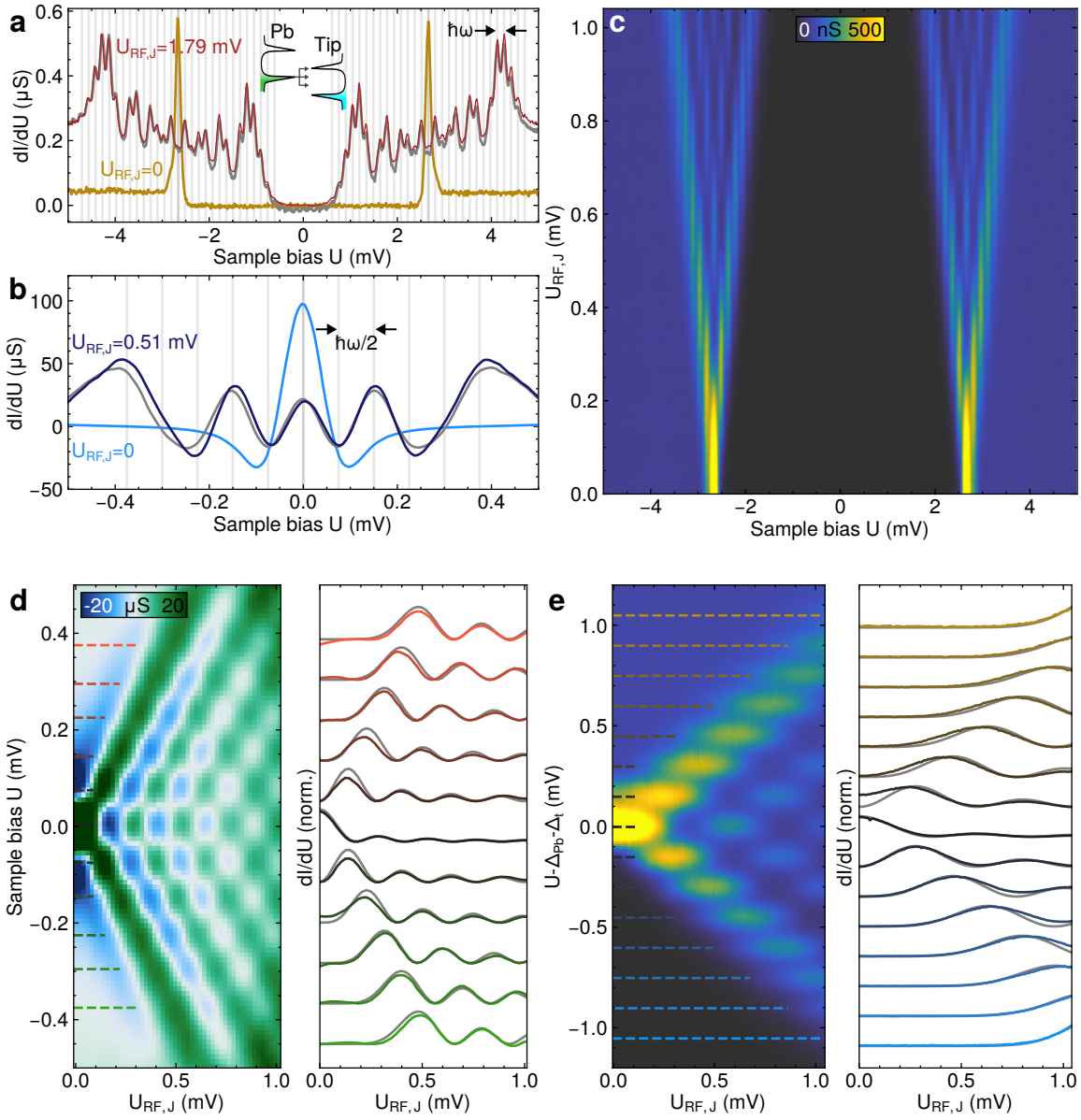

Figure 2.7: Determination of $H(f)$ via photon-assisted tunnelling of quasiparticles **(a,c,e)** and Cooper pairs **(b,d)** in a superconducting tunnelling junction formed between Pb(111) and a Pb-coated superconducting tip. Details are given in the text. The RF amplitude is represented by the calibrated value $U_{\mathrm{RF,J}}$. Irradiated curves in **(a)** and **(b)** have been scaled by 8 and 4, respectively. The best fits of Equation (2.4) are shown as grey lines. Junction resistance 10 MΩ in **(a,c,e)** and 25 kΩ in **(b,d)**. $f = \omega/2\pi = 35.375$ GHz in **(a)** and 36.270 GHz elsewhere. Data courtesy of Dr. Stefano Trivini.

Tunnelling between superconductors on the other hand is highly sensitive to RF radiation, even at very small amplitudes.[181–183] In the STM, such a SIS arrangement is naturally given for superconducting (S) tip and substrate, and vacuum (I). We choose here Pb(111) for its large superconducting gap $\Delta_{\mathrm{Pb}} \approx 1.4\,\mathrm{meV}$.[184] By controlled indentation into the surface,[185] a superconducting cluster can be formed on the STM tip. At large junction resistances, tunnelling through vacuum occurs via the conversion of Cooper pairs into electron quasiparticles. These excitations are represented by sharp peaks in the DOS around the Fermi energy (inset of Figure 2.7a) separated by the pairing energy $2\Delta_{\mathrm{Pb}}$, for the surface, and $2\Delta_{\mathrm{t}}$ for the tip.

If the DC bias is tuned to the threshold voltage $U_t = \Delta_{\mathrm{Pb}}/e + \Delta_{\mathrm{t}}/e$, quasiparticle tunnelling occurs.[186] Figure 2.7a displays such a spectrum (orange line), characterized by an absolute gap of $2U_{\mathrm{t}}$ and two peaks of widths $\approx 100\,\mu\mathrm{eV}$. At smaller junction resistances, also Cooper pairs may tunnel directly between tip and sample. This supercurrent manifests as a sharp zero-bias Josephson peak in $\mathrm{d}I/\mathrm{d}U$, as seen in Figure 2.7b (light blue line).

Application of RF drastically modifies the conductance spectrum for both quasiparticle and Cooper pair tunnelling. Tien and Gordon[187] described the effect of RF as a sinusoidal modulation of the quantum-mechanical phase of the quasiparticle wavefunction. This yields harmonics n of $\hbar\omega = hf$ in the density of states, with amplitudes described by squares of the n-th Bessel functions[5] of the first kind, which we denote as $\mathcal{J}_n^2$. A very similar treatment was found accurate for Cooper pair tunnelling in STM, which is believed to be explained by the small tip-substrate capacitance.[173,176,188–190] The differential conductance modified by RF irradiation thereby becomes

$$\left(\frac{\mathrm{d}I}{\mathrm{d}U}\right)'(U, U_{\mathrm{RF,J}}) = \sum_{n=-\infty}^{+\infty} \mathcal{J}_n^2\left(\frac{qU_{\mathrm{RF,J}}}{\hbar\omega}\right)\frac{\mathrm{d}I}{\mathrm{d}U}\left(U + \frac{n\hbar\omega}{q}\right) \tag{2.4}$$

Where $q = e$ for quasiparticles and $q = 2e$ for Cooper pairs, and $\mathrm{d}I/\mathrm{d}U$ is the conductance in the absence of radiation.

The modification of $\mathrm{d}I/\mathrm{d}U$ is commonly interpreted as the result of photon-assisted tunnelling processes: by absorbing or emitting discrete numbers of energy packets, quasiparticles can tunnel below and above the threshold voltage. Since the photon energy is on the same order as the coherence peak width, this places replica resonances at integer multiples of $\hbar\omega/e = hf/e$ around U_t. In the same picture, Cooper pairs absorb or emit an energy packet $hf/2$ due to their double charge. Experimental measurements for either case are shown in Figure 2.7a (dark red line) and Figure 2.7b (dark blue line).

The junction RF amplitude can be obtained from photon-assisted tunnelling in three ways. First, the irradiated conductance spectrum can be fitted to by inserting a non-irradiated reference $\mathrm{d}I/\mathrm{d}U$ spectrum into Equation (2.4). This directly yields $U_{\mathrm{RF,J}}$. Another measurement is possible when sweeping the applied RF amplitude. A false colour plot of $\mathrm{d}I/\mathrm{d}U$ as a function of $U_{\mathrm{RF},0}$ is shown in Figure 2.7c. The coherence peaks split open linearly, as the most dominant terms in the sum of Equation (2.4) fulfil $|n|\hbar\omega \approx eU_{\mathrm{RF,J}}$. From the opening angle, the transfer function $H(f)$ can be determined even if the individual har-

monics are not resolved. The third, and most precise, method is to directly fit the traces $(\mathrm{d}I/\mathrm{d}U)'\left(U_0 + \frac{n\hbar\omega}{q}, H(f)U_{\mathrm{RF},0}\right)$ with $H(f)$ as a shared parameter for all n. In this way, we can determine the junction RF amplitude with a precision on the order of 50 µV, as shown in Figure 2.7d,e for quasiparticle and Cooper pair tunnelling, respectively. Note that if single harmonics are well resolved, neither f needs not be known for the procedure. This allows simultaneous calibration and RF amplitude and frequency versus the voltage standard of the STM biasing circuit.

2.5 Detection of radio frequency-induced signals

Since ESR-STM gives changes in current of only tens of fA at typical tip-surface distances, we employ lock-in detection by square-wave modulating the RF amplitude (chopping) with a 50 % duty cycle. If this is done at a frequency above the bandwidth of the STM feedback loop ($\approx$ 200 Hz), the RF sweep can be performed in constant-current mode to eliminate vertical thermal and piezo drift. Here we use $f_{\mathrm{mod}} = 517$ Hz, chosen to lie below the tunnel current amplifier's roll-off frequency at gain settings 1×10^9 V A^{-1} and 1×10^{10} V A^{-1}. The signal's in-phase component is then additionally passed through a digital boxcar filter. The same technique is applied to detect the rectification current when calibrating the TF. The acquisition of TF and ESR-STM data often takes on the order of 1 h. To counteract lateral drift, the tip is periodically re-positioned on top of the atom under study by a gradient ascent algorithm.[191]

Other detection schemes are in principle possible. One may modulate f as in ensemble ESR,[13] but the resulting lineshape in $\mathrm{d}I/\mathrm{d}f$ will be narrow and requires finer sweeps. One may also sweep the magnetic field magnitude B at constant f.[13,120,192] Since one does not need to correct for ripple in the TF, this has the advantage of being able to pick a frequency with minimal attenuation. However, one risks surpassing the magnetic tip's coercive field, altering its polarization. Furthermore, ramping B can lead to drift via magnetic induction and is often linked to mechanical noise, which is a source of spin decoherence. In coupled systems, B also does not independently control energy splitting, but it also directly alters the character of the eigenstates. Sweeping and chopping the RF frequency is thereby the approach taken in Chapter 5.

Chapter 3

Sensing fields and charges with molecular spins

Molecular spins are affected by surfaces electrostatically and magnetically. We will show in this chapter how these mechanisms can be mitigated to protect intrinsic properties, but also that they can extend the functionality in such systems. In Section 3.1, we investigate the exchange bias mechanism in topological end states of chiral graphene nanoribbons synthesized on the ferromagnetic surface $GdAu_2$. We exploit our findings to sense such magnetic interactions at the atomic scale. By attaching a single nickelocene molecule to the STM tip, we directly map the exchange field of the same substrate in Section 3.2. Lastly, we investigate the magnetometric sensitivity of a novel, potentially quantum-coherent, metallocene probe in Section 3.3.

An article manuscript describing the results of Section 3.1 is under preparation:

> L. Edens, F. Romero Lara, T. Sai, K. Biswas, F. Schulz, M. Vilas Varela, D. Peña, S. Sanz Wuhl, T. Frederiksen, J. I. Pascual. "Spin and charge control of topological end states in chiral graphene nanoribbons on a moiré ferromagnet" (2025).

Data included in Figure 3.1d and Figure 3.4 was contributed by the co-authors Dr. Fabian Schulz and Trisha Sai.

3.1 Spin and charge control in graphene nanoribbons on a 2D ferromagnet

The counting rules presented in Section 1.1.2 predict radical states in nanographene at half filling. However, the metallic catalyst required for their synthesis can induce charge transfer, whereby radicals are either paired by excess electrons if anionic, or lost to the substrate if cationic. The latter occurs in chGNRs supported by the electronegative (large work function) surface Au(111), where a transfer of two electrons out of the SPTESs quenches their local magnetic moments.[50] On the other hand, with electropositive (small work function) metals, anionic charge states were found.[193,194] The effect derives from a work function mismatch across the large planar interface formed between the substrate and graphene. To restore the local magnetic moments, we seek a metallic surface that catalyses the formation of nanographene, but is electrostatically matched to the electron affinity of chGNRs. Alloys of rare earth metals with gold were previously shown to have a lowered work function on the order of that of graphene.[195,196] To this end, we investigate thin films of the intermetallic compound $GdAu_2$ directly grown on Au(111),[140] which were recently shown to be catalytically active.[197] Since this surface is also a 2D in-plane ferromagnetic at low temperatures, we will also study its effect on the magnetic configuration of chGNRs.

We exposed a clean Au(111) single crystal surface to Gd as described in Section 2.1. Figure 3.1a shows the resulting surface. Since the $GdAu_2$ lattice is rotated against that of

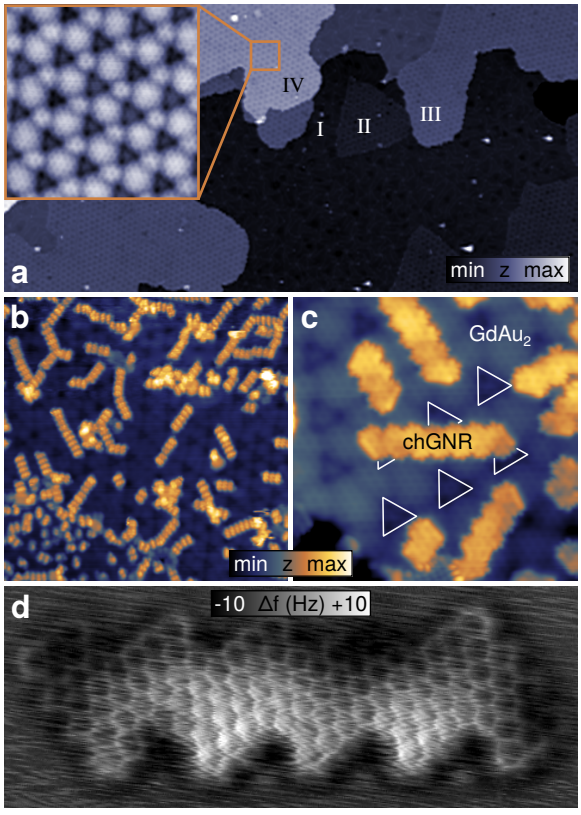

Figure 3.1: On-surface synthesis (OSS) of $(3,2,8)$-chGNRs on $GdAu_2$. **(a)** is a large-scale STM scan showing the layer-by-layer growth mode $GdAu_2$ (1 V, 10 pA, $300 \times 150\,nm^2$, scale −3.5 to 5.5 Å). Roman numerals mark the four stages. Inset is a close-up of a stage IV layer (0.2 V, 0.5 nA, $16 \times 16\,nm^2$, scale −0.80 to 0.15 Å). **(b)** shows the Ullmann-polymerized precursor after the first annealing step (0.2 V, 50 pA, $50 \times 50\,nm^2$, scale −1 to 6 Å). **(c)** displays the cyclodehydrogenated product obtained in a second heating cycle (0.4 V, 1 nA, $15 \times 15\,nm^2$, scale −2.5 to 0.9 Å). White triangles highlight the natural alignment of chGNRs with respect to the moiré structure. **(d)** is a bond-resolved AFM scans of a defectless 5 PU nanoribbon. Oscillation amplitude 60 pm.

Au(111), a moiré pattern is formed. We observe continuous terraces of this crystalline phase in regions III and IV, and a disordered reconstruction of Au(111) with residual dissolved Gd in I. Patches of an intermediate layer are also visible (II). We attribute II-IV to successive layers of $GdAu_2$, as evidenced by the increasingly pronounced and regular moiré pattern, and I to the previously described "trigon" phase.[140] All experiments are carried out on layers of stage IV or higher. The moiré superstructure consists of a hexagonal array of triangular minima. At positive tunnel biases, individual Gd sites are imaged as regularly spaced dark spots.

$(3, 2, 8)$-chGNRs were synthesized directly on the $GdAu_2$ surface from a molecular precursor (Section 2.1) by incremental heating. After the first annealing step, Ullmann coupling occured, which leads to the formation of polymeric chains, as seen in Figure 3.1b. Subsequent annealing enables cyclodehydrogenation, resulting in fully planar and isolated chGNRs with a natural distribution of lengths. As resolved in Figure 3.1c, they are naturally aligned along high-symmetry directions of the Gd lattice. Successful on-surface synthesis is confirmed by bond-resolved AFM imaging using a CO-functionalized qPlus tip, which shows regular six-membered rings across the whole molecule.

To determine whether the chGNRs on $GdAu_2$ are charge-neutral, we probe their electronic properties by STS at a temperature of 5 K. Figure 3.2a displays differential conductance spectra taken on the boundary of a 7 PU chGNRs using a metallic tip. Both termini exhibit a sharp zero-bias anomaly, whereas the local density of states (LDOS) on the chiral edge only displays the characteristic gap between edge-localized bands. We attribute the former features to Kondo resonances arising from screening of π-radicals by conduction electrons. This indicates a half-filled chGNR, with two local magnetic moments, consistent with single occupancy of the SPTESs. Charge neutrality is also supported by the symmetric positioning of the Fermi level within the band gap. Notably, the closely related $(3, 1, 8)$-chGNRs were previously found to be in a doubly anionic state on the same substrate.[197] This hints at a possibly lower electron affinity in $(3, 2, 8)$-chGNRs due to the increased number of armchair elements along the chiral edge, and is testament to the high sensitivity of π radicals in GNRs to charge transfer.

Higher-resolution spectra often reveal split resonances, which suggests a magnetic coupling. Its origin will be addressed in below. The outset spectrum in Figure 3.2a also shows two shoulders accompanying the Kondo resonances spaced approximately at ±40 mV, which we attribute to the respective SOMO and SUMO split off by intramolecular Coulomb repulsion U_{H}, as shown in Figure 1.4a. The opening of a correlation gap with near-symmetric spacing is yet another indication of single occupancy of both SPTESs and the stabilization a magnetic ground state.

A completely different class of structurally identical chGNRs is found in other adsorption geometries atop the moiré superstructure (Figure 3.2b). Here, a (split) Kondo feature is encountered only at one of the termini, whereas the other displays a much broader resonance located well below the Fermi level. We attribute this second feature to a doubly occupied SPTES, thereby the HOMO. In this singly anionic charge state ($q = -e$), a surplus electron

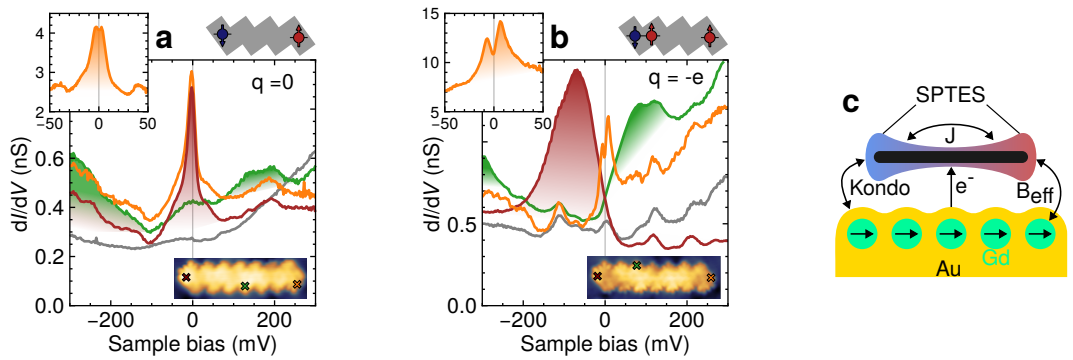

Figure 3.2: Characterization of $(3, 2, 8)$-chGNRs on $GdAu_2$. **(a-b)** display tunnel spectra taken on the two termini (red, orange), the chiral edge (green) and bare $GdAu_2$ (gray) for two 7 PU chGNRs in different adsorption configurations. The first case corresponds to a the charge-neutral molecule, displaying two Kondo resonances. In the second, an excess electron gives double occupation of the left terminus, as evidenced by the broad resonance at negative sample bias. Outsets are high-resolution spectra, where a splitting of the Kondo feature can be resolved. In **(c)** we sketch the interactions affecting the SPTESs: intramolecular exchange J, Kondo screening, charge transfer and exchange bias B_{eff}.

resides within the left terminus and quenches the π-radical. This is corroborated by the Fermi level residing closer towards the edge conduction band, which remains localized to the chiral edge. The MFH solution for this charge state is a $S = 1/2$ spin state we refer to as the charged doublet. As discussed in Section 1.1.2, under the influence of U_{H} the SPTESs forming the HOMO remain degenerate, while SOMO and SUMO, localized on the singly occupied terminus, split off (Figure 1.4c).

The occurrence of two different charge states suggests differing degrees of substrate interactions. To test this hypothesis, we laterally manipulate a chGNR into several adsorption positions using the STM tip. We find reversible switching from the anionic configuration to the neutral case. The 7 PU chGNR investigated in Figure 3.3 is initially encountered with a doubly occupied SPTES on terminus T2 and a split Kondo resonance on the other. After repositioning by a few nanometers, the excess electron switches sides. Now, the HOMO is located on T1, and the local moment on T2. By another manipulation, the molecule transitions into to the charge-neutral state, with split Kondo resonances on either side. In the final position (Figure 3.3d), a pair of zero-bias peaks with no resolved splitting is detected, again indicating perfect half-filling. Clearly, $GdAu_2$ supports charge neutral chGNRs only in certain adsorption geometries.

To sense the local character of charge transfer, we employ KPFM to map the local contact potential difference of the moiré superstructure (Figure 3.4a). Indeed, we find the triangular features to exhibit a decreased LCPD over the rest of the unit cell by around 80 meV, indicating a locally smaller substrate work function, and hence an electropositive character. When a chGNR terminus lies in its proximity, transfer of a single electron is facilitated, resulting in double occupation of one SPTESs. The triangular features therefore act as a local gating potential.[198] KPFM has also been applied to map charge distribution at the intramolecular

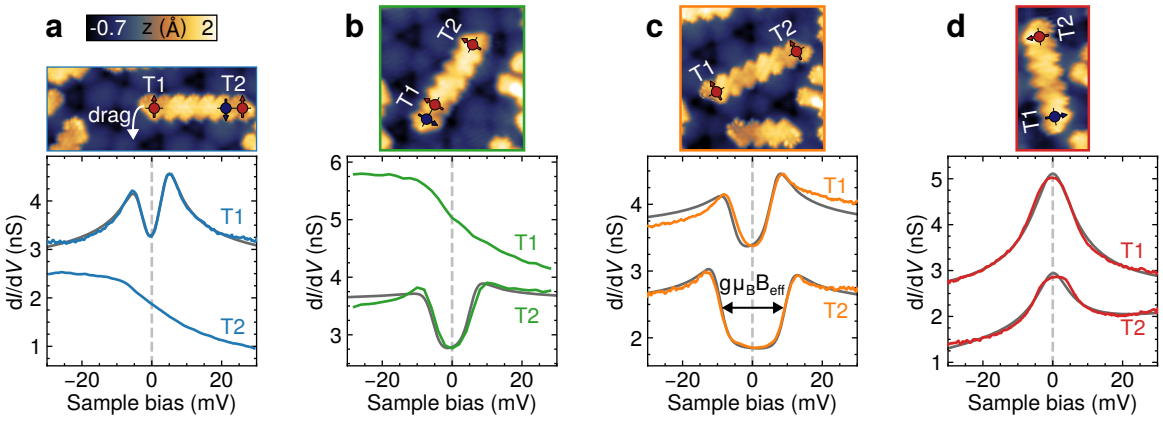

Figure 3.3: Controlling charging and exchange biasing of a 7 PU chGNR on $GdAu_2$. By lateral manipulation of the same molecule into four different positions, we observe the excess electron switching sides from terminus T2 to T1 **(a-b)**. The neutral case is realized in **(c)** with large a large exchange bias. In the last position **(d)**, B_{eff} is smaller than the Kondo coupling on either termini and the zero-bias resonance is restored. Fits of the inelastic tunnelling theory **(a-c)** and Frota lineshapes **(d)** are shown in gray.

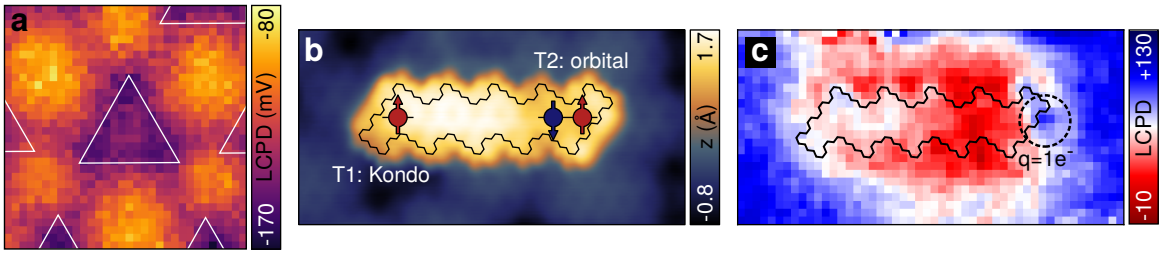

Figure 3.4: Visualizing the localized charging effect. Kelvin probe force microscopy (KPFM) of bare $GdAu_2$ **(a)** reveals a decreased local work function in the triangular moiré minima by tens of meV (junction resistance 140 MΩ, oscillation amplitude 50 pm, 5 × 5 nm^2). The chGNR in **(b)** exhibits a doubly occupied orbital on terminus T2, and is adsorbed above a moiré minimum (0.5 V, 1 nA, 9 × 4.5 nm^2). The right SPTES shows localized increase in LCPD **(c)**, consistent with a single excess electron residing in T2 (junction resistance 865 MΩ, oscillation amplitude 50 pm, 9 × 4.5 nm^2).

level.[199–202] Here, we will attempt to sense the spatial extent of the excess electron residing in terminus T2 of the charged doublet chGNR shown in Figure 3.4b. The KPFM scan Figure 3.4c reveals two features. For one, the pillow effect the molecule has on $GdAu_2$ results in a decreased work function (decrease in LCPD) in a wide perimeter around its boundary. Second, there is highly localized increase in LCPD at the upper section of T2, consistent with the expected negative charge. The associated local potential is strong enough to negate both the pillow effect, and that of the moiré minimum lying underneath T2. Terminus T1, with a singly occupied SPTES, exhibits no such feature.

As seen in Figure 3.3, the splitting of the Kondo features also depends strongly on adsorption geometry. We attribute this effect to the exchange bias[108,129,203] exerted onto chGNRs by $GdAu_2$ which is a known 2D in-plane ferromagnet at low temperatures.[197,204,205] Due to their direct proximity, the radicals thereby experience an effective magnetic field. From fits of the third-order inelastic tunnelling mode, shown as grey lines in Figure 3.3, we obtain B_{eff}, assuming $g = -2$, to be as large as 84 T.

By their spatial extension, the π-radicals interact with several Gd^{3+} $4f$ moments of the underlying surface. This coupling may either be direct, homogeneously falling off with separation, or of the indirect Ruderman–Kittel–Kasuya–Yosida type, decaying in an oscillatory manner.[206] The latter has been suggested as the coupling mechanism in $GdAu_2$.[204] Considering that the Gd lattice is spaced relatively far at 5.5 Å,[140] it is plausible that for different positions of the termini the net exchange coupling varies. In long chGNRs such as in Figure 3.3, B_{eff} can even differ in magnitude between the two termini. We will also show in Section 3.2 that $GdAu_2$ has a magnetic texture congruent to its moiré structure.[197,205]

In the gas phase and at half filling, Coulomb repulsion favours antiferromagnetic alignment between π-radicals, especially at short lengths. When interfaced with $GdAu_2$ however, each spin residing in each SPTES is exchange-coupled to both its counterpart at the other end, as well as to the magnetic surface. We will parametrize these competing interactions as J and B_{eff}. If B_{eff} is smaller than J (as in Figure 3.3d), the singlet state persists. If, however, B_{eff} dominates over J, the triplet state is favoured over the singlet state, and both radicals align with the substrate magnetization. For any given number of PUs, there must be a critical value of the effective magnetic field at which the cross-over between charge-neutral singlet and triplet occurs. Likewise, there must be a critical local substrate work function deviation at which one SPTES becomes doubly occupied, giving the charged doublet, again for any length and effective field.

Due to the extended nature of nanoribbons, the contribution of intramolecular coupling to the net exchange splitting is small in our experiment. We find that in any molecule with $L \geq 5$ PU the zero-bias resonance, without any splitting, can be restored by reorientation of the nanoribbon on the substrate. J/k_{B} therefore must be smaller than the Kondo temperature T_{K} which can be calculated to be 23 K on terminus T2 in Figure 3.3d[6]. Under the influence of Kondo scattering, the singlet ground state is therefore not well defined for long chGNRs. The triplet state, on the other hand, is stable against these fluctuations if $2\mu_{\mathrm{B}}B_{\mathrm{eff}} > k_{\mathrm{B}}T_{\mathrm{K}}, J$.[207] In this way, an exchange field can protect magnetic moments from

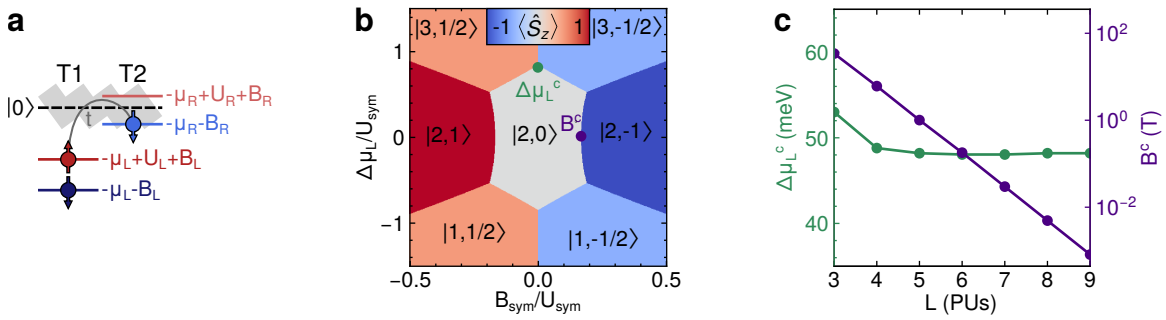

Figure 3.5: Modelling chGNRs with the asymmetric Hubbard dimer. The definition of the four levels representing the two termini T1 and T2 are shown in **(a)** for the state $\hat{c}^{\dagger}_{\mathrm{L}\uparrow}\hat{c}^{\dagger}_{\mathrm{L}\downarrow}\hat{c}^{\dagger}_{\mathrm{R}\downarrow}|0\rangle$. The general phase diagram for symmetric fields and repulsions **(b)** at $\mu_{\mathrm{R}} = U_{\mathrm{sym}}/2$ and $U_{\mathrm{sym}}/t = 3$ exhibits two critical points in the left chemical potential $\mu_{\mathrm{L}} = U_{\mathrm{sym}}/2 + \Delta\mu_{\mathrm{L}}$ and Zeeman energy B_{sym}. Colour denotes the total spin projection $\langle S_z\rangle$ in units of $\hbar$. U_{sym} and t are obtained from tight-binding theory of $(3,2,8)$-chGNRs. The resulting values for $\Delta\mu_{\mathrm{L}}^{\mathrm{c}}$ and the critical field B^{c} are shown in **(c)** as a function of length L.

scattering, even if in contact with a fully metallic surface.[208]

To capture the intricate competition between π-delocalization, electron-electron repulsion, local gating, and exchange bias, we map chGNRs onto a modified Hubbard dimer model, in which each site represents one terminus.[46,209,210] This approximation provides a good description of the system in the limit of small to intermediate U_{H}, where the spin-polarized active space is limited to only the SPTES, which remain energetically well separated from the quantized edge-localized states (Figure 1.4). Working in the grand canonical ensemble, we gate both sites with different chemical potentials and apply magnetic fields. The Hamiltonian in the second quantization formalism is:

$$\begin{aligned}\hat{\mathcal{H}} = &-t\sum_{i\neq j}\sum_{\sigma}\hat{c}^{\dagger}_{i\sigma}\hat{c}_{j\sigma} + \sum_{i}U_i\hat{n}_{i\uparrow}\hat{n}_{i\downarrow} \\ &-\sum_{i}\sum_{\sigma}\mu_i\hat{n}_{i\sigma} + \sum_{i}B_i\left(\hat{n}_{i\uparrow} - \hat{n}_{i\downarrow}\right)\end{aligned} \tag{3.1}$$

The first and second term are the conventional Hubbard dimer, with i, j as the site indices L and R, with hopping t and Coulomb repulsion parameter U_i. The third term includes the chemical potentials μ_i. A site-specific Zeeman effect is represented by the last term, with B_i in units of energy. To facilitate the interpretation of this model, we will assume symmetric repulsion (U_{L}=U_{R}=U_{sym}) and fields (B_{L}=B_{R}=B_{sym}) as well as half-filling of the right site $\mu_{\mathrm{R}} = U_{\mathrm{sym}}/2$. We introduce $\Delta\mu_{\mathrm{L}} = \mu_{\mathrm{L}} - U_{\mathrm{sym}}/2$, the departure of site L from half filling, to capture the observed deviations from work function matching in $GdAu_2$. Exact diagonalization of Equation (3.1) gives 16 states denoted $|N, S_z\rangle$, where N is the number of electrons and S_z is the net spin in units of $\hbar$. There are nine possible ground states. The occupation $N = 2$ gives the neutral singlet $|2,0\rangle$ and triplet states $|2,\pm1\rangle$, which split under B. For $N = 3$, we identify the charged doublet $|3,\pm1/2\rangle$, which also splits with B, and whose separation from $N = 2$ is determined by μ_{L}. The singly occupied $N = 1$ and closed-shell states $N = 0, 4$ are not relevant to our experiment.

Figure 3.5b shows the ground-state phase diagram as a function of field and gating potential. We identify two critical points along the two axes. The critical field $B_c = J/g\mu_B$ marks the transition from neutral singlet to neutral triplet. At the critical local gating potential $\Delta\mu_L^c$, the charged doublet becomes favourable over the neutral singlet.

To quantify these points, we performed tight-binding calculations of chGNRs in order to extract effective parameters. The dimer hopping is extracted from the small hybridization splitting between SPTESs amounting to $2t$, and drops exponentially with the length L. The Coulomb repulsion U_{sym} is equal to $U_H = 3$ eV times the self-overlap integral of the SPTESs orbital, and is mostly length-independent. L thereby controls U_{sym}/t, which dictates electron localization. For instance, increasing the length from 3 to 9 PU, the critical field B_c decreases from 34 T to below 1 mT. This is expected in the limit of large localization, where $J = 4t^2/U_{sym}$.[46,57,210]

Based on the small value obtained for B_c in this model, we hypothesize that the neutral 7 PU-chGNR in Figure 3.3c resides in a stable triplet state, as the exchange bias here far exceeds both the critical field and the Kondo coupling energy. The observed inelastic excitations are therefore from the triplet to the singlet state. Due to the localized nature of the SPTES, this change in equilibrium magnetic configuration does not modify the remaining molecular orbitals, as can be seen from the MFH solution of the full molecule in the triplet state presented in Figure 1.4b.

The critical gating potential $\Delta\mu_L^c$ on the other hand is only weakly length-dependent and approaches a constant value of $U_{sym}/2 = 48$ meV for $L > 5$ PU. In this limit, the bond formed within the dimer, mediated by t, becomes insignificant and $\Delta\mu_L$ must only overcome Coulomb repulsion (and B_{sym}, if present) to doubly occupy the left site. The work function depression in the moiré minima (Figure 3.4a) is therefore sufficient in magnitude to explain the charged double state.

From our model, we expect the intramolecular exchange to overcome $k_B T_K$ only for $L \leq 3$ PU. However, in this limit, the bulk-edge correspondence breaks down as the hybridization splitting between SPTES approaches the bulk band gap,[50] and the π-radical state is destroyed. Singlet-to-triplet excitations are therefore most likely not observable in chGNRs on metallic substrates, where the Coulomb repulsion U_H that determines J is screened by conduction electrons.[52]

3.2 Mapping exchange fields with a single-molecule probe

To further our understanding of the exchange bias between the in-plane ferromagnet $GdAu_2$ and adsorbed molecular spins, a spin-sensitive probe is required to map the magnetic order with atomic precision. SP-STM measurements on $GdAu_2$[197,205] showed a change in the sign of spin polarization in the triangular moiré minima. This method however provides no information about the actual exchange field emanating from magnetic surfaces.

It has been recently shown that both cobaltocene ($CoCp_2$) and nickelocene ($NiCp_2$) can be stably bound to STM tips.[22,211–213] Since the metal spin is localized to the central ion in metallocenes,[214] generally only weak Kondo coupling was observed in $CoCp_2$ and $NiCp_2$, which in the case of $NiCp_2$ allows for exceptionally efficient spin-flip scattering. It manifests as dominant steps in differential conductance spectra, both when adsorbed on the tip and on a surface. Proximity to other spins or magnetic surfaces then leads to an exchange splitting of these features, enabling the spatial mapping of effective magnetic fields with atomic resolution.[160,215–220]

We show here that $NiCp_2$ can sense the collective ferromagnetism of $GdAu_2$. By attaching the molecule to the STM tip, we map out the surface magnetization across the moiré pattern. We then bring $NiCp_2$ into controlled mechanical contact with $GdAu_2$, enabling us to observe the exchange bias atom-by-atom as it would be felt by a naturally adsorbed molecule. In this quantum point contact (QPC) arrangement, we also find indications of an exotic high-spin Kondo state. We introduce a simple model based that describes the evolution of spectral features as the magnetic QPC is formed.

$NiCp_2$ was deposited onto $GdAu_2$ by in-situ sublimation as detailed in Section 2.1. It is imaged as individual circular protrusions of approximately 5 Å apparent height randomly distributed on the moiré superstructure, as seen in Figure 3.6a. Upon closer inspection, a hexagonal outline and a six-fold symmetric internal structure is revealed. We attribute this to the "donut"-like appearance of $NiCp_2$ and $CoCp_2$ observed on (100) surfaces (cf. Section 3.3), but here under the influence of fast switching between degenerate tilted adsorption configurations on a hexagonal symmetry site.

Approaching an atomically sharp Au-coated tip at small negative sample bias leads to a transfer of $NiCp_2$ to the tip. Other $NiCp_2$ molecules then appear with central protrusions (Figure 3.6b,c). At close tip-surface distances, a striking atomic contrast emerges, as seen in Figure 3.8c. Each hexagonal cell coincides with a Gd lattice site. The particularly sharp borders indicate that probe-particle imaging[221] takes place: the $NiCp_2$ experiences Pauli repulsion and skips instantaneously from one Gd atom to the next, leading to a discontinuity in current. The highest spatial resolution with functionalized tips is obtained with nc-AFM.[135] Scanning a $NiCp_2$-decorated qPlus tip across the surface within the negative force gradient regime, we can additionally resolve the Au sites as spots with positive frequency shifts of around 10 Hz (Figure 3.6d).

At a temperature of 5 K, $NiCp_2$ exhibits sharp conductance steps in tunnel spectra due to the

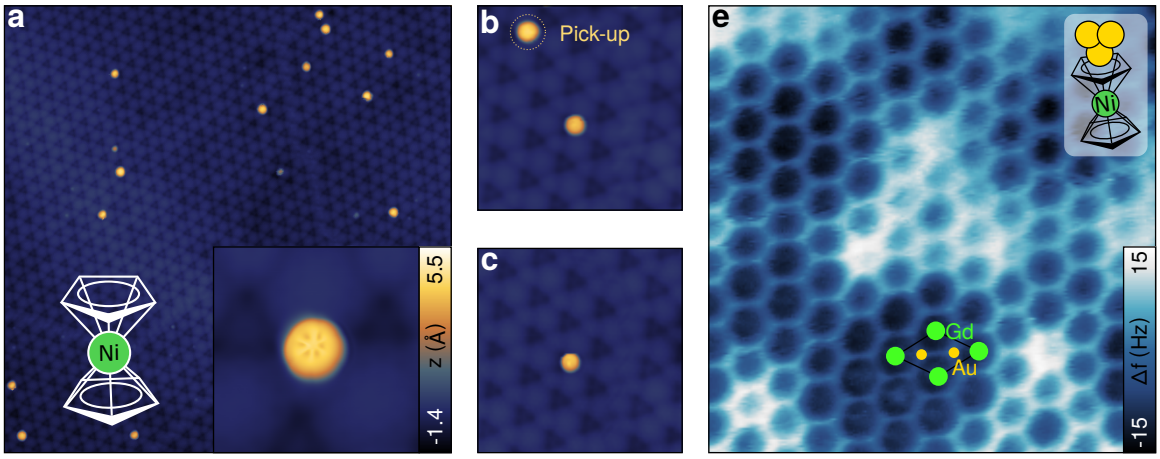

Figure 3.6: Low-temperature sublimation of $NiCp_2$ onto $GdAu_2$. **(a)** STM scan (−300 mV, −10 pA, 100 × 100 nm^2) showing predominantly intact vertically adsorbed molecules. Inset shows a close-up resolving the internal structure of Cp (30 mV, 30 pA, 5.8 × 5.8 nm^2). **(b,c)** show the vertical molecular manipulation of a single $NiCp_2$ and the subsequent change of contrast of another $NiCp_2$ molecule (−100 mV, −10 pA, 19 × 19 nm^2). **(d)** is a CH non-contact AFM (nc-AFM) image taken with a $NiCp_2$-functionalized tip in the repulsive regime, resolving the atomic structure of $GdAu_2$ (0 V, 50 pm, 6 × 6 nm^2).

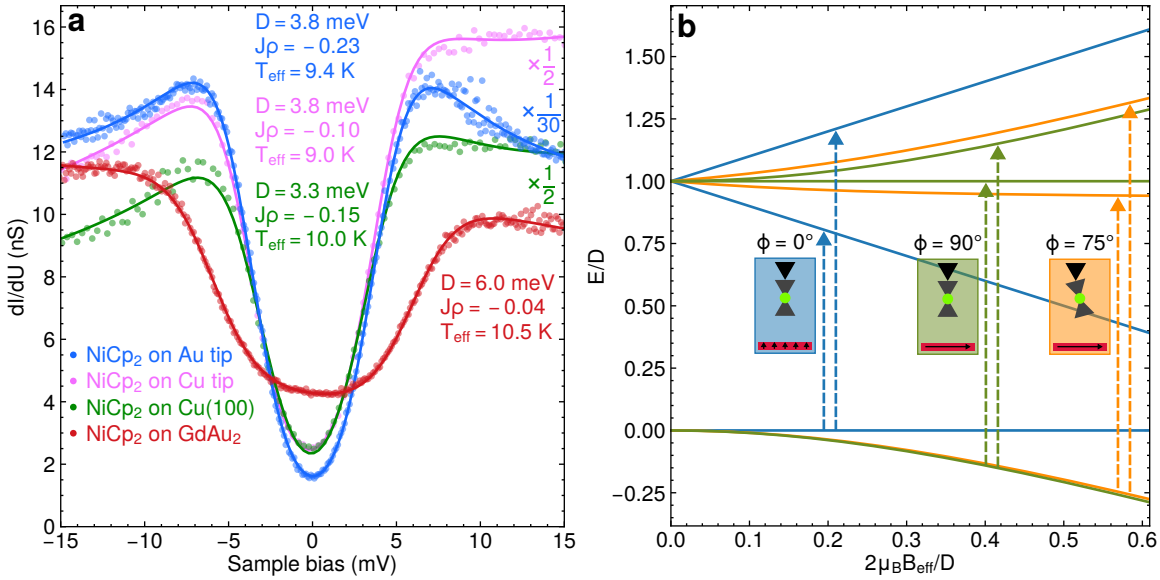

Figure 3.7: **(a)** IETS of $NiCp_2$ in four different environments: adsorbed on $GdAu_2$ and Cu(100) surfaces, and on Au and Cu tips. Fits are shown as lines, with the parameters given. Three curves have been scaled by the factors on the right hand side. **(b)** Zeeman diagrams of $NiCp_2$ for three scenarios of exchange bias sensing: experiencing an out-of-plane (effective) field (blue), an in-plane one (green), and an oblique one corresponding to a tilted adsorption on the tip (yellow). We define ϕ as the angle formed between the magnetic field and the molecular symmetry axis. The probed inelastic transitions in each case are shown with arrows at three different B_{eff}.

spin-flip from $m_s = 0$ to $m_s = \pm 1$ (Figure 3.7). The measured curves are well described by the third order spin-flip scattering model. When attached to Au and Cu-coated tips, the inelastic gap amounts to 6.6 meV. When $NiCp_2$ is instead physisorbed onto the Cu(100) surface, it shows a smaller gap.[211] In stark contrast, $NiCp_2$ atop the $GdAu_2$ shows a much larger gap, and broadened conductance steps. In this case, the fit yields an increased anisotropy and increased effective temperature. This is a first indication that $NiCp_2$ is exchange-coupled to the ferromagnetic surface. The in-plane magnetization of $GdAu_2$[204] acts as an exchange field B_{eff} and leads to a non-linear splitting of the excited states $m_s = \pm 1$ and a downshift of the ground state $m_s = 0$, as seen in Figure 3.7b. Due to the competition of easy-plane anisotropy and the in-plane Zeeman effect, the level splitting due to in-plane fields is weaker than that of an out-of plane fields. Therefore, we do not resolve a splitting of the spin-flip transition in our experiments, but instead an opening of the gap and a broadening. Molecular distortion[222] and coupling to magnetic continua[223] may manifest similarly, but would be inconsistent with the observations that follow.

The precise adsorption geometry of $NiCp_2$ on Au tips is presently unknown. Density functional theory (DFT) calculations indicate a slightly tilted adsorption geometry on Cu tips.[160] This effect would in principle aid in splitting the spin-flip transitions as the effective field would gain a component along the molecule's magnetic hard axis. We do encounter evidence of tilted adsorption in the form of asymmetric probe-particle imaging (for example in Figure 3.12f) for some tips. However, we find the contribution of a 15° off-axis tilt to be small compared to the thermal energy (Figure 3.7b) and will disregard it in the following.

We now study the spatial dependence of the exchange bias across the moiré superstructure. We transfer a $NiCp_2$ molecule to the tip and record a two-dimensional STS grid, as shown in Figure 3.8. The junction conductance is chosen high enough to obtain a measurable exchange bias, but low enough to be in the tunnelling regime. We localize the boundary formed between the $GdAu_2$ layer and the Au(111) substrate to compare magnetic and non-magnetic surfaces. The latter shows the herringbone reconstruction characteristic of mostly pure Au, which we use as a non-magnetic reference.[140,224] Spectra recorded with the $NiCp_2$ tip placed above $GdAu_2$ exhibit an augmented inelastic gap and broadened transitions compared to probing bare Au(111), which confirms the magnetic sensitivity of the molecular probe. This is most evident in the second harmonic signal $\mathrm{d}^2I/\mathrm{d}U^2$ (Figure 3.8b). As before, the inelastic model agrees exceptionally well with the recorded spectra for almost all positions on the grid.

From the opening and broadening of the inelastic gap , we obtain a two-dimensional map of the in-plane exchange field acting on $NiCp_2$ adsorbed on the tip. We remark that the pixel-to-pixel corrugation in B_{eff} is not an artefact, but as will be shown later, is due to variations between individual Gd sites which are not sufficiently resolved here. We can make out two patterns: diagonal stripes along the {<}11> direction, and maxima coinciding with the triangular depressions. Magnetic stripe domains regularly occur in unmagnetized thin film ferromagnets[225] and are the result of a periodic canting of the magnetization vector. The stripe spacing has also been shown to decrease strongly towards the Curie temperature.[226] Considering that we apply no external magnetic field in our experiments, and $GdAu_2$ has a

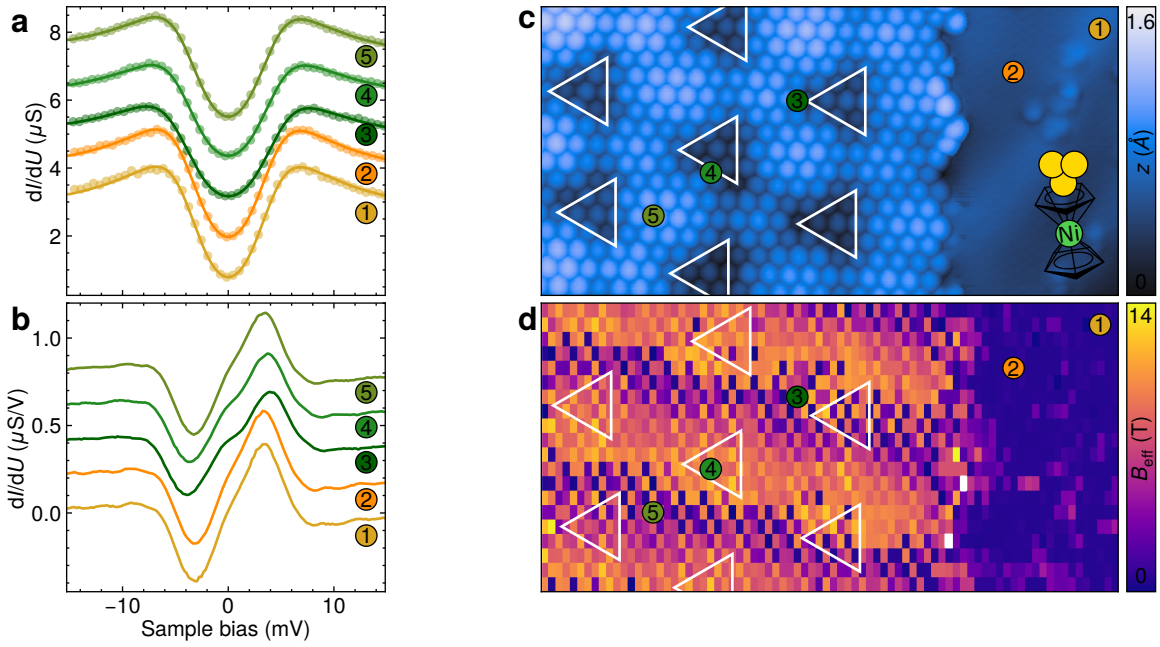

Figure 3.8: Mapping the exchange field of $GdAu_2$ using a $NiCp_2$-functionalized tip in the tunnelling regime. At each tip position, we fit the third order spin-flip scattering model with a fixed electronic temperature and anisotropy, and a varying fully in-plane magnetic field. We also include a linear background conductance, linear scaling and offset. **(a,b)** show the (normalized) differential conductance $\mathrm{d}I/\mathrm{d}U$ (with fit) and inelastic signal $\mathrm{d}^2I/\mathrm{d}U^2$, respectively, at selected locations both on both Au(111) (1,2) and $GdAu_2$ (3-4). **(c)** is a STM scan of the corresponding area taken with the same tip. **(c)** plots the effective magnetic field obtained from the fit to the 2D grid (−2 mV, −1 nA, 16 × 8 nm^2, 1 $mV_{0\text{-}p}$, 473 Hz). Note the absence of B_{eff} on Au(111), and the striped order with maximal values in the triangular depressions.

low Curie temperature of around 19 K,[227] this may offer an explanation for the occurrence of stripes. As their periodicity does not coincide with that of the surface, they cannot be caused by a topographic effect. To quantify the vertical decay of the exchange field, one needs to establish an absolute reference point for the tip-sample separation z. Remarkably, tip-adsorbed $NiCp_2$ can be brought into direct mechanical contact with metallic surfaces.[211] Under these conditions, if only one transport channel is available at the Fermi energy, the conductance amounts to $G = G_0 = 2e^2/h$, the conductance quantum. For an atomically sharp tip and an elongated molecule like $NiCp_2$, this is a reasonable assumption. At these low junction resistances, a significant ohmic voltage drop occurs in the resistive bias line with $R = 1\,\mathrm{k}\Omega$ due to the large tunnelling current I. We obtain the actual bias voltage as $U_{\mathrm{J}} = U_0 - IR$, where U_0 is the externally applied potential.

Before sensing the $GdAu_2$ exchange bias with this method, we will first study $NiCp_2$ QPCs formed with an Au-coated tip against bare Au(111). Figure 3.9 shows false color plots of the differential conductance $\mathrm{d}I/\mathrm{d}U$ and a line plot of the ohmic junction conductance G over the course of the approach up to QPC. We find that the contact is formed continuously with-

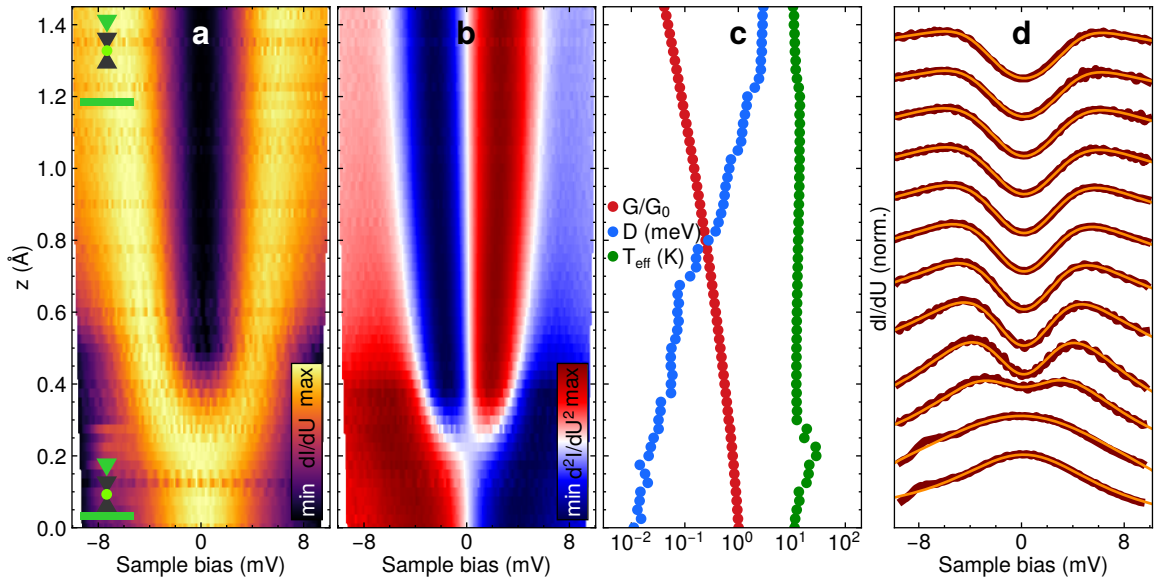

Figure 3.9: Evolution of the inelastic gap in an approach of a $NiCp_2$-functionalized tip against Au(111) up to molecular QPC. **(a,b)** are false color plots of the normalized differential conductance $\mathrm{d}I/\mathrm{d}U$ and inelastic signal $\mathrm{d}^2I/\mathrm{d}U^2$, respectively, against the tip-sample distance z and bias voltage U. **(d)** shows fits to selected obtained conductance spectra with the parameters given in **(c)** at selected z . **(c)** also includes the elastic conductance extracted from $I(U)$.

out the abrupt conductance jumps reported previously in the case of Cu electrodes.[211,228] G increases exponentially in the tunnelling regime, before tapering off as G_0 is reached.[229] We also observe a gradual closing of the inelastic gap as the tip-sample distance z is decreased. Fits of the perturbative third order spin-flip scattering model allows us to track the evolution of the effective anisotropy D, which continuously tends towards zero as the contact is formed. In the QPC regime, the gap has closed completely and gives place to a zero-bias Kondo resonance.

In this control experiment, the Kondo interaction experienced by the molecule is composed of two exchange energies: J_1, the coupling to the Au tip's electrons, and $J_2(z)$, the coupling the surface conduction electrons (see inset of Figure 3.10). At large junction resistances, J_1 dominates. The Kondo temperature estimated from $J\rho$ (see Figure 3.7a) via Equation (1.14) here amounts to 10 K and the perturbative treatment is accurate. When a QPC is formed, as demonstrated in the following, the $NiCp_2$-surface interaction J_2 will be much stronger than J_1. Then, a correlated Kondo state emerges, and conductance spectra can be reproduced only by nonphysically allowing T_{eff} to vary. This inadequacy of the perturbation model is an indicator of strong Kondo screening.[75,76,207] Along the trajectory of z, we thus cross over from the weak-coupling regime into the strong-coupling regime. The transition occurs when the sum of the two Kondo temperatures, dominated by $J_2(z)$, significantly exceeds the experimental temperature.

Several line shapes are commonly employed to estimate Kondo temperatures, among which

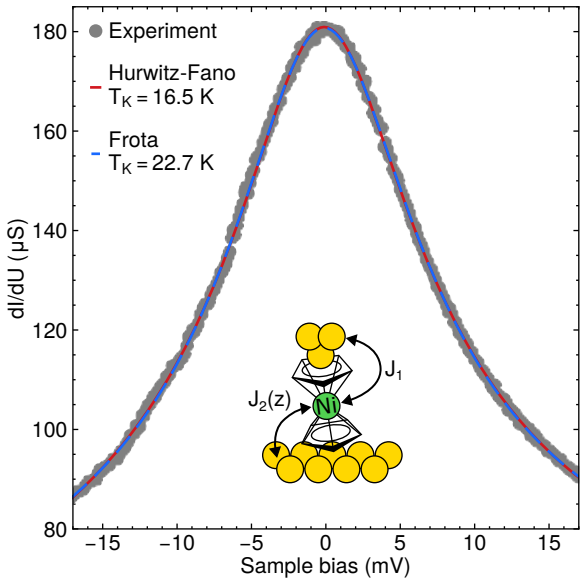

Figure 3.10: Zero bias peak of the $NiCp_2$ QPC ($z = 0$) on Au(111) shown in Figure 3.9. Fits of the Frota and Hurwitz-Fano peak functions are shown. They allow inferring the Kondo temperature T_K. The inset sketch shows the two Kondo coupling energies considered.

are the Frota function[83] or the recently developed Hurwitz-Fano function.[84,230] Figure 3.10 shows fits of the two line shapes to the differential conductance at $z = 0$. Under the assumption that $T_K >> T$, the fit of the Frota function gives $T_K = 22.7$ K. The Hurwitz-Fano theory rigorously includes the effect of thermal broadening and allows a more direct determination of the Kondo temperature. From it, we obtain $T_K = 16.5$ K. At our experimental temperature of 5 K, we can thereby confirm the $NiCp_2$ QPC as a strongly coupled Kondo system. This is at variance with $NiCp_2$ QPCs with copper electrodes, where $T_K < 4.5$ K.[211]

Considering the gradual spectral evolution towards a broad zero-bias Kondo peak, we hypothesize that in our experiments $NiCp_2$ retains its $S = 1$ even in QPC. We do not consider the charge transfer effect that has been proposed for the case of Cu electrodes[211,228,231] where $NiCp_2$ discontinuously snaps to contact. Since compression of $NiCp_2$ was found to increase D[232] we also discard any structural effect.[211,222,232,233] This $S = 1$ scenario was also entertained in recent studies.[228,234] Unfortunately, due to the large Kondo coupling strength, discerning between a $S = 1/2$ and $S = 1$ by temperature or external magnetic field studies is experimentally unfeasible.

Anisotropic $S = 1$ impurities such as $NiCp_2$ may exhibit a Kondo effect only in the case $D < 0$ and $E = 0$, as a degenerate ground state is required.[235,236] In order to explain the zero-bias peak characteristic of an isotropic $S = 1$, the Kondo coupling to the surface $J_2(z)$ has to be strong enough to overcome the magnetic anisotropy D in a process known as renormalization.[76,237,238] This is feasible in our $NiCp_2$ QPCs where we observe large Kondo temperatures on the order of D. The stability of our junction allows us to vary z continuously and observe the anisotropy renormalization directly (Figure 3.9).

The proposed triplet Kondo-screened state of $NiCp_2$ in QPC can fall into two categories. For $S = 1$ impurities on surfaces, one typically considers only one scattering channel available to screen the impurity to an effective $S = 1/2$ surrounded by a Fermi liquid - the "underscreened" Kondo effect.[239] In the present case, as there are two electrodes, the $S = 1$ may

instead be fully screened to a Kondo singlet distributed on both tip and surface.[240] As the respective couplings are asymmetric, this has been called a "two-stage" Kondo effect, referring to the successive order in which screening occurs as the temperature is lowered.[235,241]

Regardless of the spin multiplicity of the correlated state, the Kondo peak is expected to split under a strong exchange bias, which acts as an effective field B_{eff}. In the $S = 1/2$ case, the Zeeman effect will have to overcome the Kondo energy $k_{\mathrm{B}}T_K$ and the temperature broadening $5.4k_{\mathrm{B}}T$ in order to induce an observable gap.[242] In the underscreened $S = 1$ picture, the resonance has been shown to split linearly starting at lower fields.[239]

To sense the exchange interaction with $GdAu_2$ as experienced by chGNRs, we now approach a $NiCp_2$ tip on top of individual Gd atoms in the $GdAu_2$ lattice until a QPC is formed. False-color plots of the inelastic signal $\mathrm{d}^2I/\mathrm{d}U^2$ are displayed in Figure 3.11. In two positions (Figure 3.11b,c), we do indeed observe a remnant inelastic gap at $z = 0$. We attribute it to the in-plane exchange bias of the underlying surface sensed by $NiCp_2$, acting as an isotropic $S = 1$ impurity due to the large Kondo renormalization. In Figure 3.11a we instead measure an unsplit zero-bias peak at QPC, similarly to the control experiment on Au(111) and our study of chGNRs on $GdAu_2$ in Section 3.1. In this position, B_{eff} is smaller than the Kondo energy and no exchange gap is resolved.

As found before (Figure 3.8), the exchange field is highest in the triangular moiré minima. We can exclude any topographic effect as an absolute height reference has been established. In Figure 3.12, we measure the QPC exchange gap Δ for several Gd atoms along high-symmetry directions of the $GdAu_2$ superstructure. The largest splitting amounts to 6 meV. Assuming a linear Zeeman effect and $g = -2$, this corresponds to B_{eff}=52 T, very much in line with the exchange bias we observed in chGNRs.

We will now investigate the nature of Kondo renormalization in the presence of an exchange bias, which has so far not been studied in the STM. These effects have been addressed theoretically in the context of the underscreened $S = 1$ Kondo effect.[243,244] Experimentally, coupling to magnetic electrodes has been achieved in $S = 1/2$ quantum dots[206,245–247] and single atoms.[130]

To this end, we track the spin-flip spectrum during a full approach of tip-adsorbed nickelocene from the tunnelling regime to QPC on $GdAu_2$, see Figure 3.13a. The inelastic gap first opens and broadens due to the exchange field, which we exploited in Figure 3.8. After reaching a maximum, it then closes due to the renormalization of the magnetic anisotropy D. At contact, there remains a small splitting Δ we have identified as the exchange interaction with the surface.

We follow here a simple phenomenological treatment based on perturbation theory to model the effects of Kondo screening and an in-plane exchange field. The total Kondo coupling $J\rho$, where $J = J_1 + J_2(z)$, leads to a renormalization of the magnetic anisotropy D[76] and of the g-factor g, known as Knight shift.[248] We also consider the exchange coupling to the nearest Gd site, $J_3(z)$, that gives rise the exchange field B_{eff} (Figure 3.12c). We make the

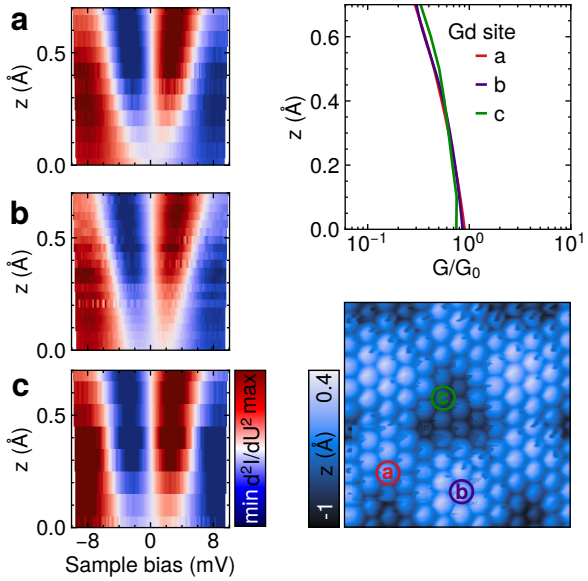

Figure 3.11: Sensing exchange bias with $NiCp_2$ QPCs $GdAu_2$. **(a-c)** show d^2I/dU^2 in the final 90 pm of contact formation with three different Gd sites and the same $NiCp_2$-functionalized tip. The magnitude of the exchange splitting at $z = 0$ increases from top to bottom. On the right side, the conductance traces are displayed. The bottom right shows the probed positions.

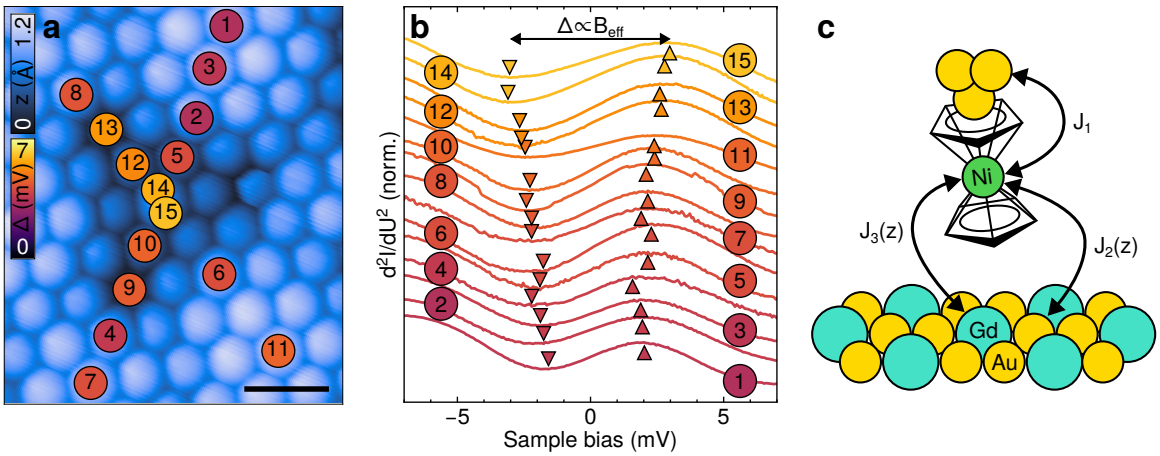

Figure 3.12: Analysis of the residual splitting of the Kondo feature of $NiCp_2$ in QPC with $GdAu_2$. **(a)** shows the Gd atoms on top of which the molecular tip was approached to form QPCs. They lie along the surface lattice's basis vectors. **(b)** shows the corresponding d^2I/dU^2 traces, sorted and colored by gap magnitude. The arrows mark the inelastic thresholds. **(a)** is a sketch of the exchange coupling acting on the $NiCp_2$ molecule.

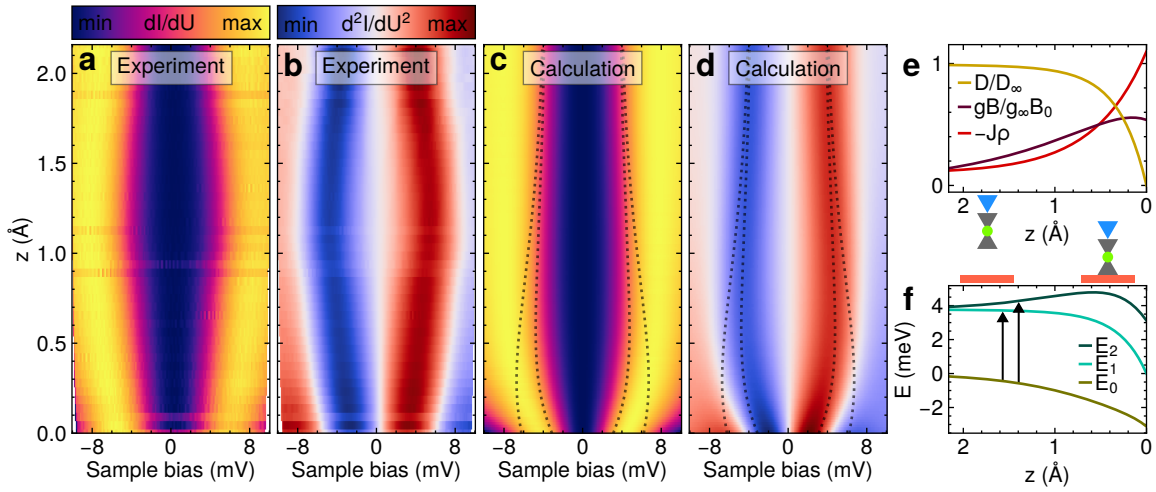

Figure 3.13: Modelling Kondo renormalization and exchange splitting of a $NiCp_2$ QPC on $GdAu_2$. **(a,b)** display the experimental dI/dU and d^2I/dU^2 signals. **(c,d)** is the best fit of the perturbative model to the experiment. Dotted lines mark the renormalized inelastic threshold voltages **(e)** shows the modelled evolution of Kondo coupling strength $J\rho$, renormalized anisotropy D and Zeeman effect gB with the tip-sample distance z. **(f)** are the renormalized state energies obtained from the parameterization. Arrows show the inelastic transitions.

assumption that J_2 and B_{eff} decay exponentially with z. We define their decay constants as α_J and α_B, respectively, and obtain:

$$J\rho = (J\rho)_\infty + (J\rho)_0 \, e^{-\alpha_J z} \tag{3.2}$$

$$B_{\text{eff}} = B_0 e^{-\alpha_B z} \tag{3.3}$$

$$D = D_\infty \left(1 - \alpha_D \, (J\rho)^2\right) \tag{3.4}$$

$$g = g_\infty \left(1 + \alpha_g J\rho\right) \tag{3.5}$$

where the quantities with subscript ∞ denote their values in the limit $z \to \infty$, i.e. far into the tunnelling regime. $(J\rho)_\infty = J_1\rho$, the anisotropy D_∞ and the effective temperature T_{eff} have already been obtained experimentally (Figure 3.7). We furthermore set $g = -2$, the bulk value.[249] The Zeeman effect is quantified by the product $(gB)_{\text{eff}}$ and leads to an opening of the inelastic gap and broadening of the inelastic transitions. For $z > 2\,\text{Å}$, this effect is not resolved at our temperature and we can set $(gB)_\infty = 5.4 k_B T/\mu_B$, where we used the IETS thermal broadening to obtain a lower bound for the decay of B_{eff}. We also require that $D(z = 0) = 0$, which is our assumption of an isotropic $S = 1$ in QPC. This fixes $\alpha_D = (J_0 + J_\infty)^{-2}$. Lastly, we set $(J\rho)_0 = -1$, since increasing beyond this value no longer affects the spectral shape as the spin-flip scattering model diverges. B_0 can be chosen freely as it will be compensated by g_{eff}. Here, we set $B_0 = 50\,\text{T}$. This leaves α_D, α_g and α_B as independent variables. With this parameterization, the eigenvalues and differential conductance can be calculated at each z using the third order spin-flip scattering model, and be fitted to the data.

The fit reproduces the general spectral features of the QPC formation (Figure 3.13c,d): the opening due to the far-distance exchange field, closing due to renormalization of D and g via the exponential rise of $J\rho$ and the remnant exchange splitting at $z = 0$. The evolution of the magnetic levels is plotted in Figure 3.13f. As the anisotropy tends to zero, the magnetic ground state E_0 transitions from $m_s = 0$, quantized along the vertical molecular axis, to $m_s = -1$, now quantized along the in-plane magnetization of $GdAu_2$. The larger of the two transitions (not thermally resolved) then requires a change in angular momentum of $2\hbar$ and becomes forbidden. In our $NiCp_2$ QPC we therefore observe only one set of inelastic conductance steps.

The maximum of the inelastic gap at $z = 1.3$ Å in this model arises from the competition between the renormalization of D and g and the exponential rise of B_{eff}. In the fit, this occurs at much closer distances (Figure 3.13f). Inclusion of higher than second order terms may be required to match the experiment better. Additionally, the assumptions of exponential decay of B_{eff} is a crude approximation considering it arises from the detailed wavefunction overlaps between the ensemble of nearest Gd sites and $NiCp_2$. The magnetization of the surface also gives polynomial dipolar terms that may be become appreciable at small distances, which we have neglected here.[218]

3.3 Vanadocene: a potential molecular spin qubit

Above, we have shown that a single nickelocene molecule can be attached to a STM tip with remarkable resiliency to sense magnetism at the atomic scale. To achieve this, we employed the inelastic spin-flip excitations of $NiCp_2$. Naturally, the question arises whether tip-adsorbed metallocenes could also be read out via quantum-coherent magnetic resonance, allowing not only higher resolution magnetometry,[250] but also to study spin entanglement with picometer precision. Metallocenes thus hold large promise for atomic-scale quantum sensing in the STM.

Unfortunately, both metallocenes proven to have magnetic moments, $CoCp_2$ and $NiCp_2$, also show significant Kondo coupling, especially when transferred to the tip.[22,160,211] Their spin coherence is thereby severely limited even at low temperatures. One must turn to molecular engineering to improve the decoupling of the electronic spin, localized on the central ion, from the metallic tip. This can be achieved by replacing the Cp ligands with larger macrocycles to increase the spatial separation,[251] or to find a central ion whose spin is even more localized.

Here, we study vanadocene (VCp_2) as a potential candidate for quantum-coherent magnetometry. Like Co, vanadium's 3d shell has a total spin quantum number $S = 3/2$. In $CoCp_2$, the ligand field then leads to a $S = 1/2$ configuration.[160] In contrast, VCp_2 retains its atomic spin and exhibits a $S = 3/2$ ground state, as predicted by quantum chemistry calculations and confirmed by ESR experiments.[19–21,252] Similarly to $NiCp_2$, it also has an easy-plane anisotropy, albeit with a much smaller MAE, as D amounts to only 525 µeV in bulk crys-

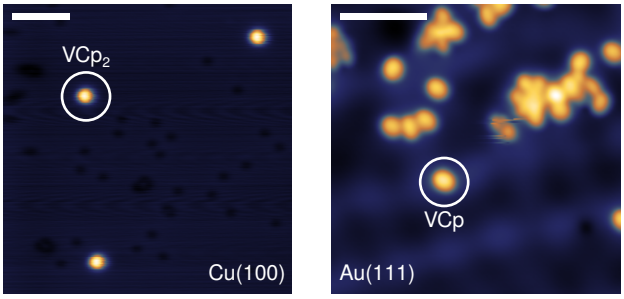

Figure 3.14: Topographic STM scans of VCp_2 adsorbates on Cu(100) (left) and Au(111) (right). Scale bar 3 nm. Imaging parameters 300 mV, 20 pA and −10 mV, −15 pA.

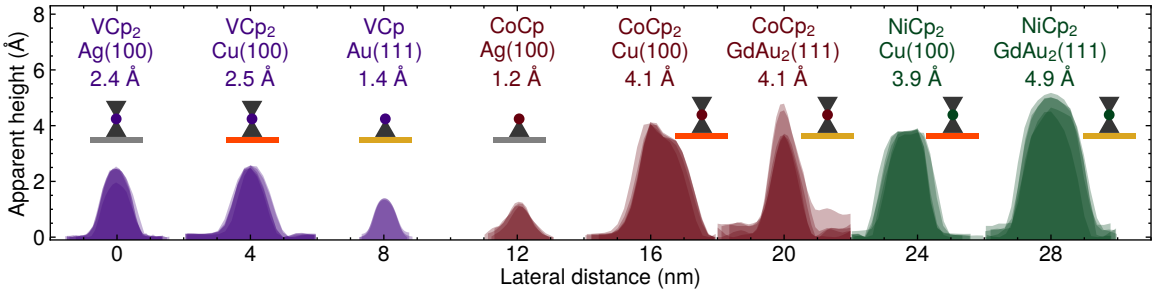

Figure 3.15: Sets of several topographic STM cross-sections through isolated adsorbates of three metallocenes on four different metallic surfaces taken at small tunnel voltages. Above, the averaged height is shown. VCp_2 is consistently imaged smaller than $CoCp_2$ and $NiCp_2$ and fractures into VCp on Au(111). The tip displacement has been calibrated against the monoatomic step height for each substrate.

tals.[21] Consequently, the lowest lying magnetic levels are the $m_s = \pm 1/2$ Kramers pair, which may undergo Kondo screening if such a channel is present.[236] Its spin is localized almost entirely on the V ion,[253] and is thereby decoupled from the environment by virtue of the Cp ligands.

We deposited VCp_2 via in-situ sublimation from room-temperature powder onto Au(111), Cu(100) and Ag(100) surfaces held at cryogenic temperatures. The adsorbate consists of randomly distributed circular protrusions as seen in Figure 3.14. Sets of topographic cross-sections are shown in Figure 3.15. We also include profiles of $CoCp_2$ and $NiCp_2$ on Cu(100), Ag(100) and $GdAu_2$ for comparison. The apparent height of the VCp_2 adsorbate is significantly reduced on Au(111) compared to Cu(100) and Ag(100). Likewise, $CoCp_2$ is imaged to be less than half as high on Ag(100) than on $GdAu_2$ and Cu(100). $NiCp_2$, on the other hand, appears identically on two substrates. The VCp_2 adsorbate is consistently less prominent than both $NiCp_2$ and $CoCp_2$ on all substrates. The dependence of apparent height on the metallic support suggests a decomposition of $CoCp_2$ and VCp_2 metallocenes on some surfaces, even at low temperatures.

Braun *et al.*[254] studied the adsorption of ferrocene on Au(111) and detected breakage of the η_5 bond between Cp ligands and the metal ion. The products are isolated Cp and the fragment FeCp, where the latter has approximately 40 % of the apparent height of the intact molecule. Evidently, this also occurs with $CoCp_2$ on Ag(100) and VCp_2 on Au(111), but we cannot unequivocally assign whether these adsorbates are pure cyclopentadienyl or the

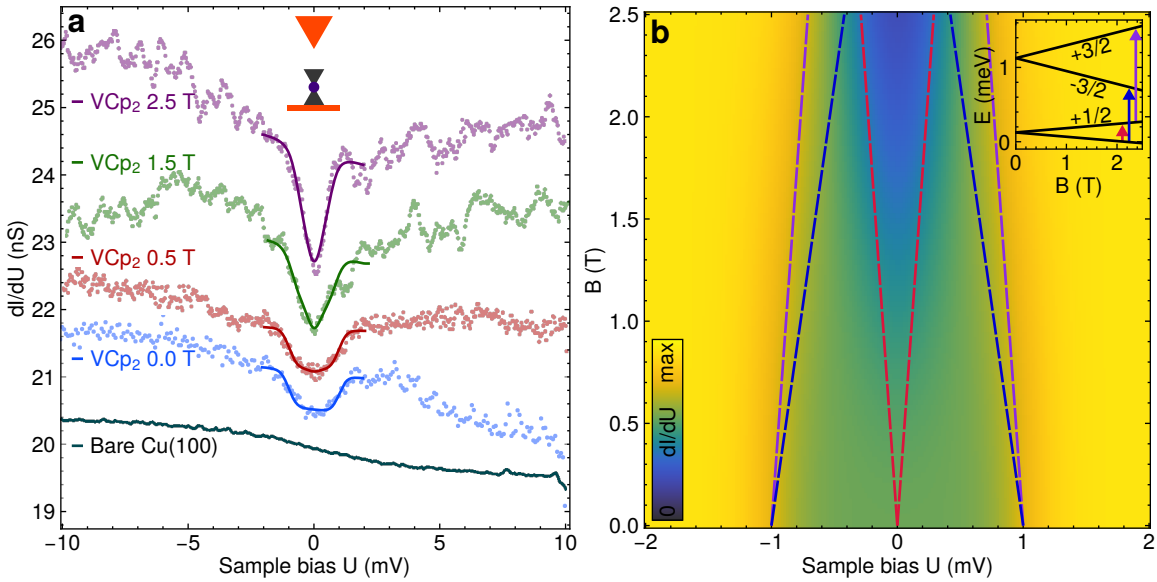

Figure 3.16: **(a)** IETS of VCp_2 on Cu(100) as a function of applied out-of-plane magnetic field. Solid lines are the global fit of the second-order spin-flip model. Spectra have been taken at 50 MΩ with a metallic tip. $D = 750\,\mu eV$. Curves are shifted for clarity. **(b)** Evolution of magnetic excitations in VCp_2 with magnetic field at 1.3 K using the anisotropy parameter obtained by the fit to the experimental data.

partial fragments CoCp and VCp.

Here, we choose to interpret the data as follows. We assign the $CoCp_2$ fragment to CoCp, which is is identical in height to the VCp_2 adsorbate on Au(111), which must then be the fragment VCp. Thereby, the adsorbate on Cu(100) and Ag(100), approximately twice as tall, must in fact be the full VCp_2 molecule. Its smaller topographic prominence in STM compared to $CoCp_2$ and $NiCp_2$ derives from a more confined frontier orbital with little LDOS on the ligands.

To prove the preservation of vanadocenes's chemical structure upon adsorption on Cu(100), we probe its magnetic state. The spin anisotropy, constituted by the ligand field, would likely be strongly altered in fragments. In Figure 3.16a we display differential conductance spectra of VCp_2 adsorbed on Cu(100) at increasing out-of-plane magnetic fields. We observe a dip around zero bias which continuously deepens. Considering the spin state and easy-plane anisotropy of VCp_2, we expect to observe three inelastic transitions, as shown in the inset of Figure 3.16b. At zero field, the transition $\pm 1/2 \rightarrow \pm 3/2$ gives an inelastic gap of width $2D$. The out-of plane field splits this conductance step into $-1/2 \rightarrow -3/2$ and $+1/2 \rightarrow +3/2$. Furthermore, a second inelastic gap opens around zero bias corresponding to the excitation $-1/2 \rightarrow +1/2$ and eventually emerges with the outer conductance steps.

At our experimental temperature of 1.3 K, these Zeeman effects cannot be resolved due to thermal broadening. The opening of the gap between $m_s = \pm 1/2$ therefore manifests only as a decrease in the zero-bias conductance. Still, we can draw conclusions from the exper-

imental data by simultaneously fitting all traces with the second-order spin-flip scattering model, which yields $D = 750\,\mu eV$ as a shared parameter. The accuracy of the fit indicates that the field evolution is indeed fully compatible with that of a $S = 3/2$ with easy-plane anisotropy. For comparison, a false colour plot of the calculated conductance as a function of B at 1.3 K using the best-fit value for D is displayed in Figure 3.16b. The measured anisotropy of a single VCp_2 on Cu(100) is slightly larger than what has been reported for bulk VCp_2 crystals in ensemble measurements.[21] Such differences are readily caused by slight molecular distortion.[222,232] We have already observed such a change in anisotropy in $NiCp_2$, depending on whether it was adsorbed on the tip or on the surface (Figure 3.7).

Summary of Chapter 3

In this chapter, we explored the interaction of the in-plane ferromagnetic surface $GdAu_2$ with single molecular spins. Our study of (3, 2, 8)-chGNRs revealed three physical effects. For one, the alloying of Au(111) with Gd finely tunes its work function to be in the range of the electron affinity, allowing for a half-filled configuration. This has enabled direct observation of local magnetic moments hosted by their topological zero modes, which on all other catalyst metals investigated were fully quenched by charge transfer. Second, we found that the electrostatically inhomogeneous moiré superstructure of $GdAu_2$ facilitates localized doping with a single electron, as confirmed by KPFM. This mechanism could be reversibly controlled by lateral molecular manipulation. The resulting singly anionic chGNRs are thereby imbued with a net magnetic moment.

Third, the substrate was found to exert a large adsorption position dependent exchange bias onto the π-radicals. By modelling the singlet-triplet splitting of chGNRs, we could anticipate that its magnitude leads to the formation of a stable $S = 1$ state in neutral chGNRs, in which both SPTESs are aligned with the in-plane magnetization of $GdAu_2$. This effect was also demonstrated to be sufficiently large to counteract Kondo screening, which should lead to an enhanced spin lifetime T_1 protected from conduction electron scattering, even on a metallic surface.

In Section 3.2, we succeeded in mapping out the exchange field emanating from $GdAu_2$. To this end, we employed tip-adsorbed $NiCp_2$ as a magnetometric probe in two regimes. In the tunnelling domain, we sensed the surface magnetization on the scale of the moiré superstructure. In quantum point contacts formed with single Gd^{3+} sites in the surface lattice, spin-flip excitations of the Kondo-screened state allowed us to infer the magnitude and atomic variation of the exchange field as experienced by physisorbed molecules. The measured splittings and atomic-scale magnetic textures agree well the position-dependent inelastic gaps encountered in chGNRs supported by the same surface.

Lastly, we investigated the metallocene VCp_2 as a potential magnetometric probe. By tracking the field evolution of its spin-flip excitations, we could confirm the robustness of its gas-phase multiplicity $S = 3/2$ when in direct contact with a metallic surface. We also

found Kondo coupling to be absent, which we attribute to more confined molecular orbitals compared to $NiCp_2$ that may host a quantum-coherent spin.

Chapter 4

Decoupling of magnetic molecules on ultrathin insulators

In the preceding chapter, we have seen how graphene nanostructures and their supporting surface can be engineered to display customized electronic spin states. To probe magnetism at the atomic scale, we employed the Kondo correlations formed with metallic surfaces at low temperatures. Unfortunately, the same effect can quench the molecular spin lifetime T_1 and thereby also limits the decoherence time T_2.[97] Realization of a single molecule qubit therefore requires an additional step: spatial decoupling from conduction electrons. As the tunnel coupling falls rapidly with distance, Kondo scattering of the molecular spin is weakened and T_1 prolonged.[131]

In this chapter, we investigate the electronic and magnetic states of several molecules spaced by thin layers of the insulator MgO above Ag(100). Section 4.1 unravels a geometric quasi-gating scheme for chGNRs that allows deterministic control of highly decoupled open-shell configurations in extended nanographene. In Section 4.2 and Section 4.3, we apply this mechanism to the zero-dimensional limit by placing individual tetrapyrroles on MgO. We find a crucial difference in the characteristic of charge transfer depending on ligand groups, and indications of a long-lived spin state in a usually non-magnetic molecule.

A preprint article containing the results shown in the first section has been published in

> A. Domínguez-Celorrio†, L. Edens†, et al. "Engineering open-shell extended edge states in chiral graphene nanoribbons on MgO". Pre-print (2024). arXiv: 2406.03927.

Part of the measurements therein pertain to the PhD thesis of the equally contributing co-author and have been included in Figure 4.5 for comparison. The interested reader is referred to

> Domínguez-Celorrio, A. *On-Surface Synthesis of Functional Organic Nanostructures* PhD thesis (University of Zaragoza, 2022).

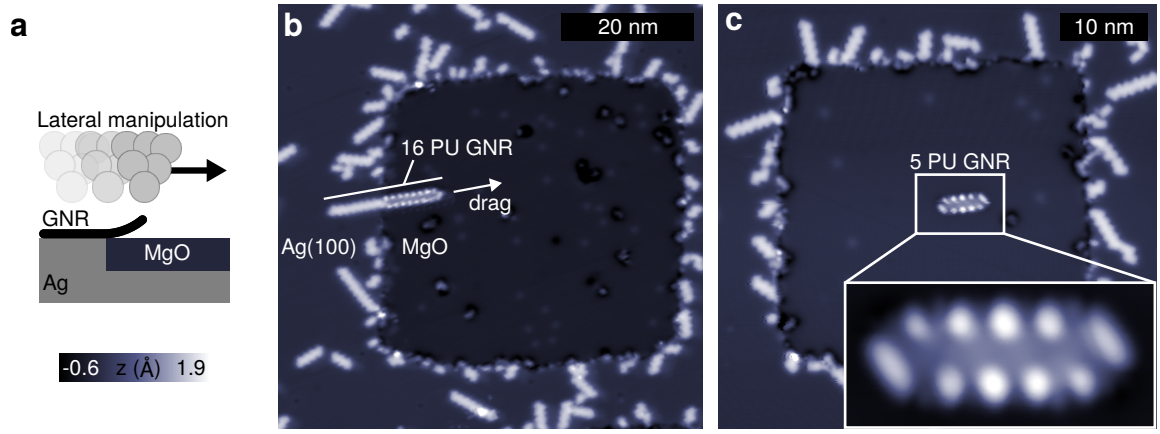

Figure 4.1: Lateral manipulation of (3, 2, 8)-chGNRs synthesized on Ag(100) onto embedded monolayers of MgO. **(a)** Sketch of the lateral manipulation procedure. **(b)** Topographic scan of a MgO island surrounded by chGNRs on the metallic substrate. A 16 PU chGNR has been dragged halfway across the interface. The segment supported by MgO shows a drastic change in appearance. **(c)** 5 PU chGNR fully supported by a layer of MgO. $U = 0.5$ V in all scans. $I = 10$ pA in **(a)** and 30 pA **(b)**.

4.1 Geometrical charge gating effect in chiral graphene nanoribbons

In order to decouple π-radical nanographenes, such as chGNRs, on-surface-synthesized molecules must be transferred to an insulating environment.[52,255] Previous studies have explored electronic decoupling of GNRs at the single-molecule level in the STM by post-synthesis surface passivation,[256,257] manual transferral onto the insulator NaCl[52,165,258] or direct synthesis on TiO_2.[259] The insulating spacer has been shown to modify the electronic state in two significant ways. For one, the decreased hybridization with the metal surface sharpens the orbital resonances. This has allowed resolving the discretization gaps between the QW-like edge-localized states in short GNRs.[52] Furthermore, the absence of metallic screening restores the electron-electron correlations that stabilize magnetism in nanographene. Intramolecular Coulomb repulsion results in the opening of a correlation gap in conductance spectra, which has been observed in spin-singlet GNRs.[52]

So far, the molecular tunnelling resonances found in GNRs on decoupling layers have exhibited broad linewidths typically on the order tens of meV, suggesting residual hybridization with the metal.[260] Insulators such as NaCl were also shown to introduce additional broadening via coupling to surface phonon modes.[68,261] Inspired by its excellent performance as a decoupling layer for magnetic atoms and smaller molecules,[13,33,101] we employ ultrathin MgO layers to fully decouple large nanographenes on the scale of tens of nm. We choose chGNRs as an archetypal system that can be synthesized in customized shapes and arbitrary length while featuring both gapped edge-localized states, and a robust set of topological zero-energy modes, as introduced in Section 1.1.2.

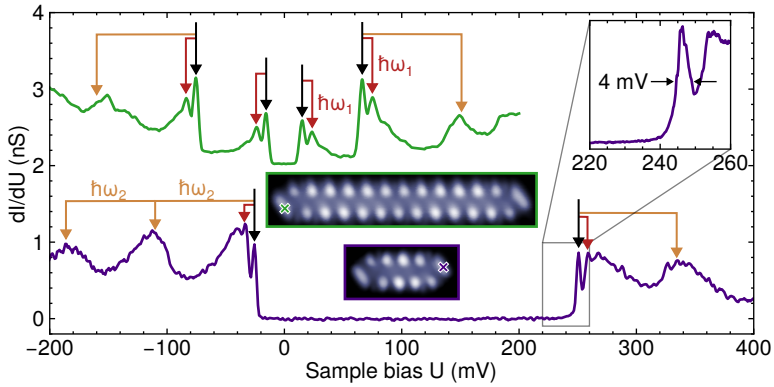

Figure 4.2: Tunnel resonances of a 5 PU (violet) and a 13 PU $(3, 2, 8)$-chGNR (green) on MgO/Ag(100). The two show vastly different and absolute conductance gaps. We can identify pairs of sharp resonances (inset). They are accompanied by vibronic satellites that appear as broader peaks at multiples of $\hbar\omega_1/e = 7.6\,\mathrm{mV}$ and $\hbar\omega_2/e = 76\,\mathrm{mV}$.

We synthesized chGNRs on Ag(100) by thermally activated Ullmann coupling of two different quateranthracene derivatives and subsequent cyclodehydrogenation, as described in Section 2.1. Alternate bromination of the precursors leads to the formation of two types of chGNRs with chiral vectors $(3, n, 8)$ with $n = 1$ and 2, respectively. Due to reaction kinetics, their final lengths vary naturally between $L = 2$ to 22 PU (precursor units). The chGNRs are then transferred to the previously grown MgO monolayer patches by means of lateral manipulation with the STM tip as shown in Figure 4.1. This is enabled by the embedding of MgO into the Ag surface, such that the two surfaces are flush.[29,141,152,156] Due to the small bias voltages used for stable imaging lying within the insulating gap of MgO, the islands are imaged as depressions. As shown in Figure 4.1b,c, chGNRs supported by MgO exhibit a stark change in STM topographic appearance, which hints at their modified electronic structure.

As seen in Figure 4.2 for two $(3, 2, 8)$-chGNRs with $L = 5$ and 11 PU, the differential conductance spectra recorded at 4.2 K exhibit zero-conductance gaps around the Fermi level ($U = 0$) delimited by unusually sharp (4 mV) molecular resonances, hallmarks of effective electronic decoupling. Each peak is followed by replicas at a spacing of 7.6 and 76 mV, independently of the chGNR length. We interpret them as vibronic excitations of chiral edge phonons in the Frank-Condon picture, similar to previous studies of individual molecules and chGNRs weakly coupled to metal surfaces.[262–265] In contrast to the bulk optical phonons responsible for tunnel resonance broadening in NaCl, these molecular vibrations are nanoscopically confined and thereby discrete and comparatively high in frequency.[266] This allows us to resolve them individually, and to discard heterogeneous broadening of the primary tunnel resonances. We attribute the residual, homogeneous, linewidth to the small tunnel coupling with the Ag substrate.[267] By correcting for bias modulation and thermal smearing, we obtain a full width at half maximum (FWHM) of 1 meV.[156] This allows to place a lower bound for the electronic lifetime on the order of 1 ps, in line with typical values of well-decoupled molecules.[268,269]

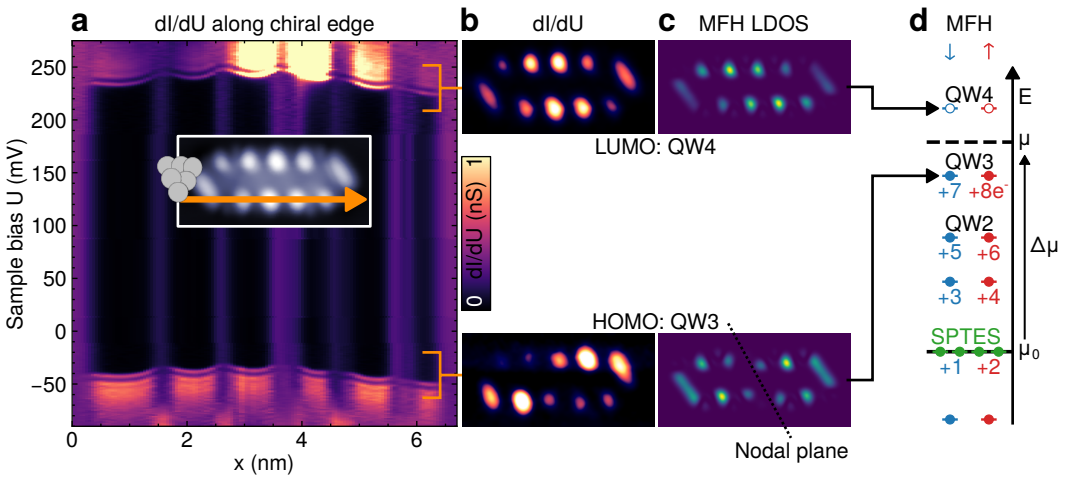

Figure 4.3: Mapping the quantization gap of a 5 PU $(3, 2, 8)$-chGNR on MgO/Ag(100). **(a)** False color plot of the differential conductance taken along the bottom chiral edge. **(b)** displays two $\mathrm{d}I/\mathrm{d}U$ scans taken at the tunnel resonances. The probed bias range is indicated with brackets. The charge state can be inferred by comparing to the LDOS of orbitals obtained from MFH calculations. The quantum-well-like edge-localized states QW3 and QW4 **(c)** match the experimental data and constitute the HOMO and LUMO. To move the chemical potential μ between these states, eight excess electrons have to populate QW1-QW3. In the level diagram **(d)** we reference μ in the charged state to the gas-phase electron affinity μ_0 by introducing the gating potential $\Delta\mu$.

The spectra in Figure 4.2 for two different lengths feature vastly different gap magnitudes. To assess their orbital character, we acquire $\mathrm{d}I/\mathrm{d}U$ spectroscopy curves along the ribbons' chiral edges. Figure 4.3a and Figure 4.4a show false color plots of the differential conductance as a function of bias and tip position x for $(3, 2, 8)$-chGNRs with $L = 5$ and 13, respectively. The spatial distribution of the conductance exhibits maxima distributed along the edge, interrupted by differing numbers and positions of nodal planes. This is characteristic of quantized states formed within the edge-localized conduction band of chGNRs we introduced in Section 1.1.2. These QW-like states are separated by discretization gaps, which here are also flanked by vibronic replicas. For $L = 5$, the resonances have zero and one nodal plane, respectively, and are spaced by a large gap of 280 meV. In the case of $L = 13$, the QW-like characteristic is most apparent as these states are less confined, and the discretization gaps are smaller. Therefore, we detect three distinct QW states within the same bias window (Figure 4.4), consistent with the longer chGNR. In contrast with the case of $L = 5$, the frontier QW states symmetrically spaced around $U = 0$ here exhibit identical intensity profiles along the edge. As will be discussed below, this spatial degeneracy is characteristic of a correlation gap,[52] as opposed to the discretization gap present for $L = 5$. Even though the QW behavior can be understood in a tight-binding framework, the inclusion of the Hubbard term proportional to U_H is essential in reproducing this effect.

By mapping the differential conductance across the entire molecule at each resonance, we can quantitatively assign the QW order by comparing in Figure 4.3b-c and Figure 4.4b-c

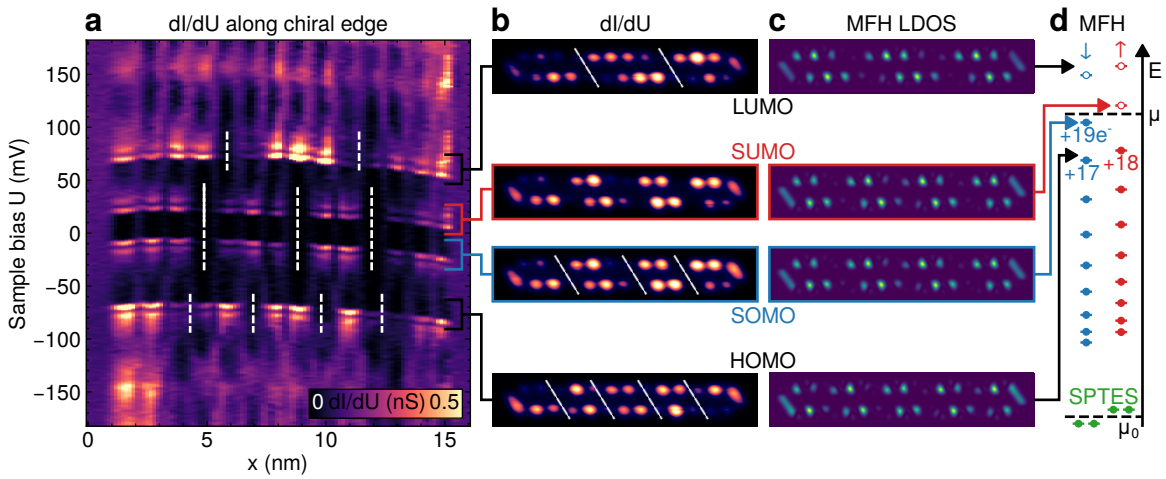

Figure 4.4: Correlation gap in a highly anionic 13 PU $(3, 2, 8)$-chGNR. In **(a)** and **(b)**, we have marked the nodal planes in the differential conductance. Note that their number decreases with energy. The smallest energy gap is straddled by two spatially identical states, mapped in **(b)**. They are SOMO and SUMO of QW9 **(c)** and differ only in their spin. **(d)** Spin-polarized energy levels with the 19 surplus electron charge required to achieve this state.

their structure with the theoretical LDOS obtained from MFH calculations. There is good agreement between the orbitals and experimental maps, in particular in the number and position of nodal planes indicated as dashed lines. To counteract the effect of a rigid electrostatic shift induced by nearby defects in MgO,[156] we apply large bias modulation amplitudes when acquiring $\mathrm{d}I/\mathrm{d}U$ maps to average out the curvature apparent in false color plots.

Let us first address the case of $L = 5$. By comparison of experiment to calculation, we identify the tunnel resonances as the high-lying states QW3 and QW4 of the gas phase ribbon. Considering that the chemical potential lies at $U = 0$ in tunnelling spectra, their position implies significant n-type charge transfer from Ag into the chGNR. Since no LDOS is present within the gap, this anionic charge state must be integer.

MFH modeling suggests that when μ lies within the quantized conduction band, common values of U_H do not significantly perturb the spatial distribution of molecular states due to their extended nature (cf. Figure 1.4d). We can therefore follow the *Aufbau* principle in filling up the gas-phase molecular orbitals from half-filling up to μ as shown in Figure 4.3d. Doubly occuping both SPTES takes two extra electrons, and populating QW1-QW3 another six. Consequently, a 5 PU-$(3, 2, 8)$-chGNR finds itself in a highly anionic closed-shell state on MgO, with eight excess electrons. For chGNRs with μ located inside discretization gaps, the charge q is always an even integer since μ must lie between doubly-occupied orbitals, the HOMO and LUMO. Figure 4.3 includes a level diagram obtained from the MFH solution of the $q = 8$ charge state. For even q, electron correlation in the MFH model only produces a rigid shift of $\mu \propto U_\mathrm{H}$ given by the last term in Equation (1.5).

Charging manifests differently in the case of $L = 13$. The observed resonances are in

perfect agreement with states QW8-QW10, see Figure 4.4b-c. Despite this high discretization index, only up to four nodal planes appear. Furthermore, their energetic ordering is inverted: the number of nodal planes decreases with energy. This is a result of the large charge transfer, which has shifted the chemical potential beyond the Brillouin zone boundary constituted by the periodicity of the chiral edge (Figure 1.3). By this inverted sequence, we assign a charge of 19 electrons. The last electron is here placed in state QW9, making q odd. QW8 and QW10 have even zero and double occupancy, respectively, and constitute the closed-shell HOMO and LUMO.

Electron-electron interactions, here represented by the Hubbard term, open a correlation gap,[50,52] which is much smaller than the discretization gaps between QW8-QW10. Its magnitude in conductance spectra is composed of the Coulomb repulsion that stabilizes the $q = 19$ open-shell charge state, plus the energetic cost of transiently inserting and removing electrons by tunnelling.[52,270] Both effects split apart the SUMO and SOMO resonances, which appear spatially identical to QW9 as the same orbital partakes in both electron and hole tunnelling. Due to single occupancy of the SOMO, the nanoribbon is imbued with an open-shell doublet spin polarization as shown in Figure 4.5d. In contrast to π-radicals we realized in neutral chGNRs on $GdAu_2$, this paramagnetic moment is highly delocalized. Theoretically, a correlation splitting is also experienced by the remaining states as seen in Figure 4.4d; this is a shortcoming of our mean-field approximation of the Hubbard model and is not the case in our experiment.

The extremely anionic charge states realized in chGNRs on MgO are unexpected. To explain the effect, we consider the level alignment of the two material interfaces present in our experiment (Figure 4.6b on page 69). MgO/Ag(100) is unique in that it possesses an extremely small work function. The supporting substrate Ag(100) with $\phi_{\mathrm{Ag}} = 4.3\,\mathrm{eV}$[70,156,271] is in itself electropositive; here, fractional charge transfer of 1.3 e^-/PU was observed in similar GNRs.[193] When interfaced with MgO, the metal additionally experiences a strong pillow effect, further lowering the work function down to $\phi_{\mathrm{MgO/Ag}} = 3.7\,\mathrm{eV}$.[156,272–274] Bulk intrinsic graphene, on the other hand, has a typical work function of $\phi_{\mathrm{Gr}} = 4.6\,\mathrm{eV}$[275,276] which is largely preserved in extended GNRs.[277]

We can apply these values to the chGNRs interface by utilizing the topological zero modes to reference the chemical potential to μ_0, the charge neutrality point. Due to the SPTES degeneracy, the electron affinity and ionization potential are both approximately equal to $\mu_0 = \phi_{\mathrm{Gr}}$ at this energy scale. When the molecule and substrate are first brought to contact, the vacuum potentials align and therefore the chemical potential μ will lie above the SPTES by $\Delta\mu = \phi_{\mathrm{Gr}} - \phi_{\mathrm{MgO/Ag}} = 900\,\mathrm{meV}$, implying an enormous transfer of negative charge. We can interpret $\Delta\mu$ as an electrostatic gating potential applied between the nanoribbon and Ag. Due to this redistribution of charge, an electrostatic potential difference forms between chGNR and Ag, with MgO acting as a dielectric spacer. Since our molecule is negatively charged, this dipolar field locally raises the effective surface work function, counteracting the pillow effect of MgO. The equilibrium value of $\Delta\mu$ is given by the delicate balance between the intrinsic work function mismatch and the interface dipole (IFD):

$$\Delta\mu = \phi_{\mathrm{Gr}} - \phi_{\mathrm{MgO/Ag}} - \mathrm{IFD} \tag{4.1}$$

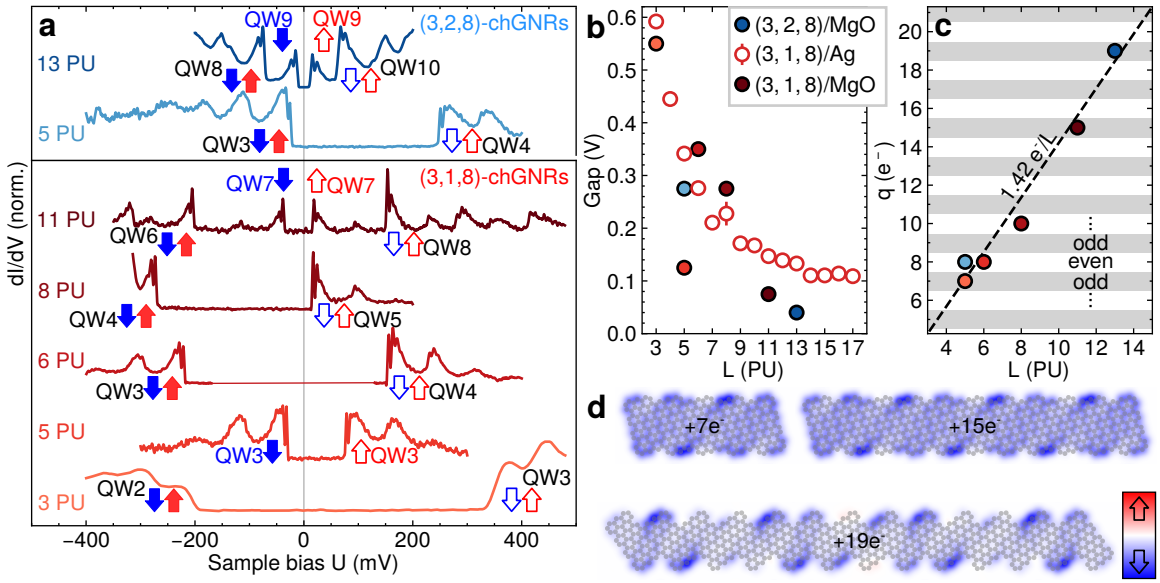

Figure 4.5: Comparing spectral fingerprints of $(3,2,8)$-chGNRs to $(3,1,8)$-chGNRs on MgO. **(a)** shows differential conductance traces for seven investigated molecules. Three spectra show correlation gaps. Arrows and labels mark the occupation of the frontier orbitals, as assigned by mapping the LDOS. The extracted gap width **(b)** and charge **(c)** follow general trends with the number of precursor units, L. **(c)** are the mean-field spin polarization of the three chGNRs with an odd charge and a correlation gap at $U_{\mathrm{H}} = 1.5\,\mathrm{eV}$.

We performed the same experiment on $(3,1,8)$-chGNRs of varying lengths. The two types ($n = 1$ and $n = 2$) differ by the effective mass of the edge-localized conduction band and therefore in their QW level spacing. Yet, both families of chGNRs investigated can be classified into the two categories described, i.e. either odd occupation with identical LDOS around the Fermi level (correlation gap, non-zero spin), or even occupation with μ between distinct QW states (discretization gap, spinless). A collection of representative spectra is shown in Figure 4.5a.

We will now consider the dependence of the electronic charge state on the ribbon length L. A control experiment for $(3,1,8)$-chGNRs on bare Ag(100) reveals exclusively discretization gaps with fractional anionic charge states due to substrate hybridization.[156] The gap magnitude decays asymptotically with L, as expected for a quantum well (empty markers in Figure 4.5b). On top of MgO, the discretization gaps observed in closed-shell $(3,1,8)$-chGNRs follow a similar trend but are slightly larger than those on Ag. We attribute this to unscreened electron-electron repulsion, which augments the gap measured in conductance spectra where charge is injected.[65,70,270] A finite drop of tunnelling bias between Ag and MgO and ionic polarization of the latter can lead to similar modifications of energy gaps.[156,261,278]

The gaps in the open-shell (q odd) species are consistently smaller than the discretization gaps and also decrease in magnitude with L. Despite these general trends, the determination of which electronic configuration occurs at which length appears to be erratic. For instance,

for $n = 1$ and $L = 5$ we have a correlation gap of about 100 meV and $q = 7$ (odd), whereas for just one more PU ($L = 6$) we get a discretization gap of 400 meV with $q = 8$. The inverse occurs between $L = 8$ (300 meV, $q = 10$) and $L = 11$ (50 meV, $q = 15$). On average, the surplus charge increases by 1.42 electrons for each PU added to the chGNR, as shown in Figure 4.5c. However, since there is no hybridization with the substrate, the charge q must be integer, and can therefore only increase either by a single electron, or by two electrons at once. The length of our chGNR therefore acts a purely geometric parameter that controls the charge state of our molecule, and therefore spin according to the parity of q.

To predict the evolution of charge parity, we now introduce a theoretical model that describes electron doping as a function of length. We represent each chGNR in contact with the substrate electron bath in the grand canonical ensemble,[279] as sketched in Figure 4.6a. Therein, it can freely exchange electrons, establishing an equilibrium number q dictated by the chemical potential μ, a temperature T, and its electronic structure determined by its length L and its chiral vector (m, n, w). To correctly describe the molecular orbitals, we compute the internal energy of each charge state E_q for both types $n = 1$ and 2 with increasing L using the MFH model. To avoid ambiguity in determining the magnetic ground state that arise for large Hubbard parameters due to the chGNR's extended size, we restrict the spin.[60] The meV-level correlation gap energy is therefore not explicitly included in E_q, but the larger mean-field Coulomb repulsion still enters proportionally to $U_\mathrm{H} = 3\,\mathrm{eV}$. The ensemble average of q is then

$$\langle q(\mu, L, T)\rangle = k_\mathrm{B} T \frac{\mathrm{d}\ln(\mathcal{Z})}{\mathrm{d}\mu} \tag{4.2}$$

We formulate our grand canonical partition function as

$$\mathcal{Z}(\mu, L, T) = \sum_q \exp\left(-\frac{E_q - q\mu}{k_\mathrm{B} T}\right) \tag{4.3}$$

We limit our sum to only a relevant range of integer surplus charges q. Note that the result of Equation (4.2) requires no definition of an absolute energy scale for E_q. In the MFH model, energies are referred to the on-site energy (ε in Equation (1.5)) which is usually set to zero. As a result, μ is referenced to the vacuum potential and on the order of several eV. We identify μ_0 as the charge neutrality point at which $\langle q\rangle = 0$, which by virtue of the zero mode nature of the SPTES is independent of L. Our value for μ_0 obtained theoretically somewhat deviates from literature values for ϕ_Gr as electron correlations are not fully captured by MFH theory. Nevertheless, μ_0 robustly defines the gating potential $\Delta\mu$ introduced previously, which allows us to draw conclusions about interface level alignment.

False color plots of $\langle q\rangle$ at $T = 4.2\,\mathrm{K}$ are shown in Figure 4.6c-d for the two chiral vectors. Due to our low temperature, fluctuations are small, and $\langle q\rangle$ here coincides with the integer value q. The diagrams illustrate how, if one fixes L and increases $\Delta\mu$, charge is transferred into the molecule in integer intervals. There is a strong preference for even-numbered charge, consistent with the correlation versus discretization gap magnitudes. Conversely, the correlation gap (q odd) state occurs only in narrow ranges of $\Delta\mu$. These windows are

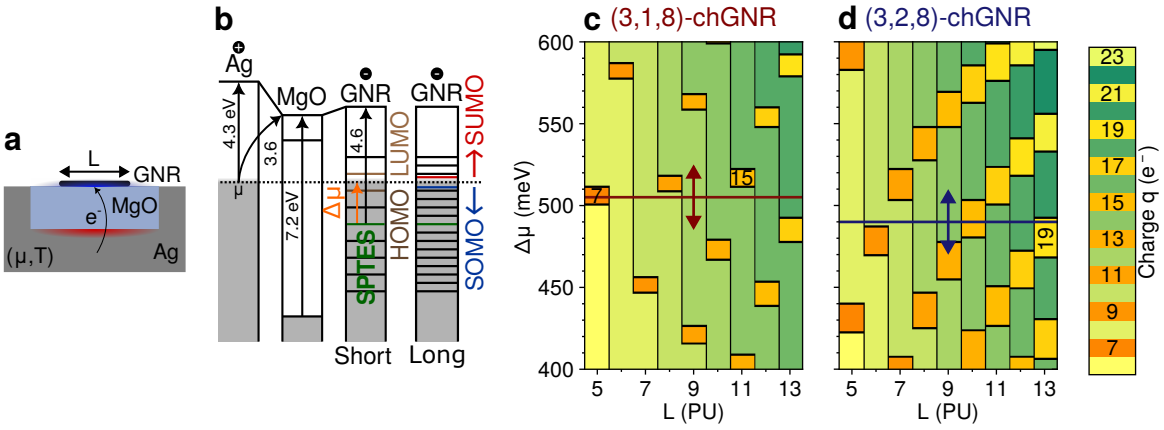

Figure 4.6: Modelling the length-dependent gating effect of MgO/Ag(100). **(a)** shows the transfer of electrons into the chGNR of length L at constant μ and T. Opposing charges accumulate on Ag and the molecule. The level alignment **(b)** follows from the interplay of work function reduction induced by MgO, the large electron affinity of graphene, and the interface dipole. The gating potential $\Delta\mu$ quantifies the deviation from charge neutrality and is length-independent. Shown are the two cases: discretization gap and an even charge, and a correlation gap with an odd charge. In the false-color plots **(c)** and **(d)**, the modelled charges for the two types of chGNRs are displayed. Different colors for even and odd q are used. By fixing a value of $\Delta\mu$, one predicts $q(L)$. The three observed cases of odd charges (correlation gap) are indicated.

stabilized by U_{H}, as odd charging occurs only when the Coulomb repulsion energy required to make q even is larger than the binding energy gained from double occupation of a QW state. Correlation gaps are more likely to occur in $(3, 2, 8)$-chGNRs because of a larger degree of localization between armchair segments and smaller discretization gaps.

Let us now fix $\Delta\mu$, as indicated by the horizontal bars, and increment L. We observe that in most cases, addition of one PU often results in a transfer of two electrons at once, i.e. a transition that conserves charge parity. In some cases however, one crosses from even to odd q and vice-versa with L by transferal of one electron only, as the second is blocked by Coulomb repulsion. In this picture, the abrupt length-dependent switching between discretization and correlation gaps is evident. It derives purely from the systematic evolution of the QW level spacing with L, competing with U_{H}. As expected, the average charge per PU for a given $\Delta\mu$ is fractional. In the thermodynamic limit $L \to \infty$, charge and level quantization becomes irrelevant and q/L asymptotically approaches an intensive value corresponding the n-type carrier density of a chGNR gated by an electric potential $\Delta\mu/e$.[193]

To obtain the local gating potential of each family of chiral ribbons on the MgO layer, we fit the experimental electron doping deduced in Figure 4.5 with predicted charges using $\Delta\mu$ as a free parameter. The results of the fit, shown in Figure 4.7, reproduce the charging pattern of both nanoribbon types with $\Delta\mu = 0.49\,\mathrm{V}$ for $(3, 1, 8)$-chGNRs and $0.511\,\mathrm{V}$ for $(3, 2, 8)$-chGNRs. The only experimental deviation is the case of $n = 1$ and $L = 8$, for which the model predicts the single occupancy of the lowest frontier state. Instead, this chGNR

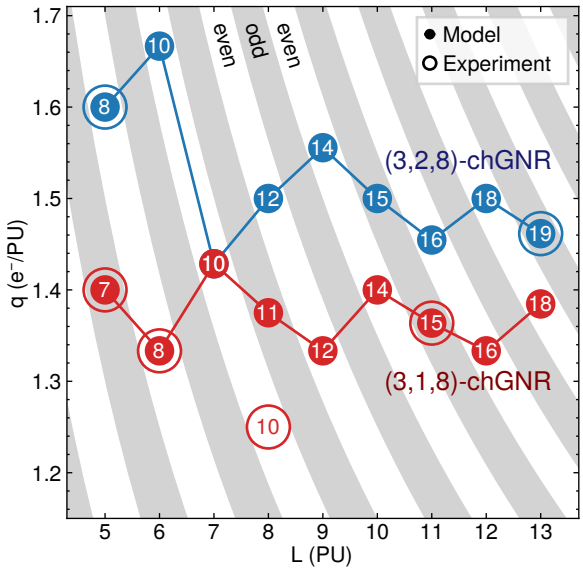

n	L (PU)	q (e⁻)	C (aF/PU)	A/A$_o$ (1/PU)
1	5	7	1.9	165
1	6	8	2.1	180
1	8	10	2.4	210
1	11	15	4.0	344
2	5	8	2.6	227
2	13	19	5.7	492

Figure 4.7: Left: fit of the gating model to experimentally determined charges. We plot q/L, which oscillates around a mean value. Even and odd charge values are indicated with shaded bands. Each point is also labelled with q. The table on the right applies the plate capacitor model to the interface dipole obtained from the fit.

appears on MgO charged with ten electrons, with its LUMO (QW5) at only 17 meV above μ (Figure 4.5a), i.e. at the verge of single occupancy. This discrepancy is likely due to the electrostatic potential emanating from nearby charged defects in the MgO lattice.[156]

The determined value of $\Delta\mu$ of approximately 0.5 eV is about half of the work function difference between MgO/Ag(001) and graphene. As mentioned above, this can be attributed to a sizable interface dipole across the MgO layer, which conversely acts to lower the molecular charge state. From the interface energetic balance (Equation (4.1)), the electrostatic energy stored in the interface becomes IFD ≈ 0.4 eV. Following the plate capacitor model of Hurdax *et al.*[280], first developed for contiguous overlayers of small molecules on MgO/Ag(100), we can use this estimated value to calculate the equivalent capacitance per precursor unit $C = \frac{q^2}{2L \cdot \mathrm{IFD}}$ of each nanoribbon, and a corresponding area $A = \frac{Cd}{\epsilon_0 \epsilon_r L}$. We set $d = 4$ Å as the chGNR-Ag spacing and $\epsilon_r = 10$ as the dielectric constant of single-crystal MgO.[281] Values are listed in the table in Figure 4.7. We express the equivalent area in units of the aromatic ring area $A_o = 5.24$ Å^2. Considering that each PU contains only 56 benzene rings, the interface capacitance is clearly overestimated by this geometric simplification. Since we are working at the single-molecule level, it is not fully justified to assign a planar area to our molecule; rather one would have to integrate over the extended charge density. Furthermore d is not determined in our experiment. Lastly, the dielectric constant may well be modified from its bulk value in our ultrathin limit.

4.2 Inducing magnetism in metal-free phthalocyanine

The highly electropositive character of MgO/Ag(100) allows inducing spin in molecules that otherwise possess no net magnetic moment by transferring an odd number of charges. This was been realized in extended chGNRs, where we found an approximately linear dependence of charge on size. Here we test the limits of this mechanism in the zero-dimensional limit by studying metal-free phthalocyanine, where electrons are localized predominantly to its small ligand groups.

H_2Pc is a planar macrocyclic molecule, where the central ring is formed by four isocyanide groups bridging between four isoindole units (inset of Figure 4.8). Importantly, it does not contain a central ion. Instead, two hydrogen atoms are bound to either of the two pairs of opposing nitrogen sites in the cycle. H_2Pc is tautomeric: the pair of hydrogen atoms may bind to the other pair of opposing nitrogen atoms with only a small activation energy. Due to the four-fold rotational symmetry, the two possible tautomers are degenerate.

In-situ deposition of H_2Pc onto MgO/Ag(100) yields randomly adsorbed molecules on both the metallic substrate and the insulating islands, as seen in Figure 4.8. The small size of H_2Pc and thereby vanishing adsorption energy on MgO necessitates the use of unusually large junction resistances, on the order of 1 TΩ, for stable imaging. This is contrast to its iron-containing analogue FePc which was previously shown to be more stable, possibly due to a weak bond formed between Fe and the O site of MgO.[11,14]

To describe the electronic state of H_2Pc on MgO/Ag(100), we assess the differential conductance curves recorded in CC mode shown in Figure 4.9. Two prominent resonances manifest in $\mathrm{d}I/\mathrm{d}U$ and steps in z at negative and positive bias, respectively. Their onset defines a conductance gap, where tunnelling takes place directly between tip and sample, without injection of charge into the molecular orbitals. When U is tuned to the positive

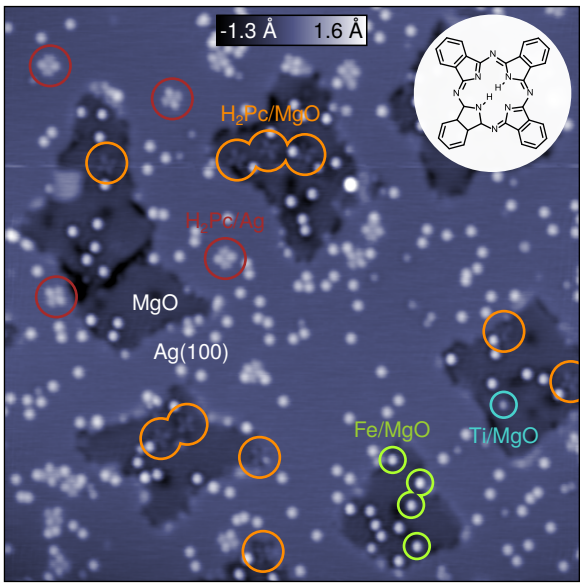

Figure 4.8: STM scan showing isolated H_2Pc, Fe and Ti adsorbed on MgO/Ag(100) following in-situ sublimation. The insulating bilayer patches here appear darker than the surrounding metal substrate due to embedded growth. Note the faint appearance of the molecule adsorbed on the metal compared to on MgO. In the inset, the chemical structure of phthalocyanine is displayed. Imaging conditions $40 \times 40\,\mathrm{nm}^2$, −100 mV, −200 fA.

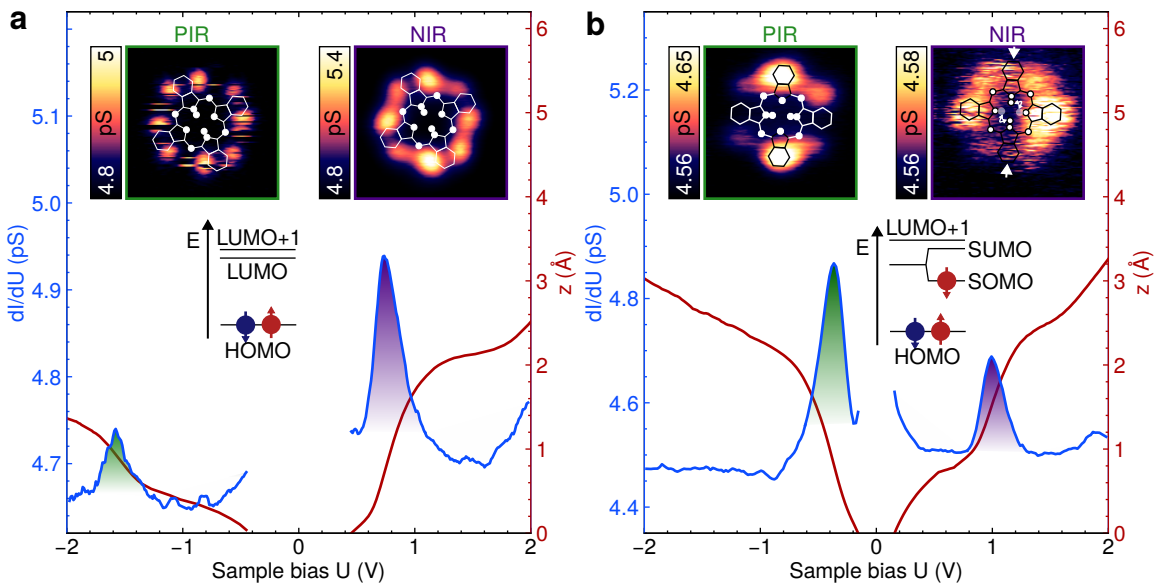

Figure 4.9: Ionic resonances of **(a)** H_2Pc and **(b)** H_2Pc^- on MgO. Insets show differential conductance maps taken at the ionic resonances, and a level diagram of the two distinct charge stares. Spectra have been recorded in CC mode at 100 and 200 fA, respectively. Image size $2 \times 2\,nm^2$.

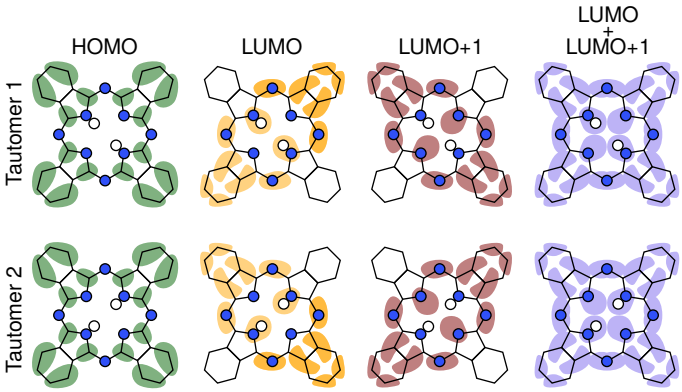

Figure 4.10: Reproduction of the gas-phase molecular orbitals of H_2Pc^0 after Imai-Imada *et al.*[282], for each tautomer. Also shown is the superposition of LUMO orbitals as it is observed in experiments.

(negative) peak, the H_2Pc is transiently charged (de-charged). These features are referred to as negative ion resonance (NIR) and positive ion resonance (PIR), respectively.[68]

We find that the adsorbed molecules fall into two distinct classes. The first type exhibits a large conductance gap on the order of 2.5 V (Figure 4.9a); the other a reduced gap of only 1.2 V (Figure 4.9b). When mapping the differential conductance at the ion resonance energies, the first type of molecule presents two fourfold-symmetric orbitals. The PIR exhibits eight circular lobes, whereas the NIR consists of four kidney-shaped lobes. The former is in direct correspondence with the gas-phase HOMO of H_2Pc as determined from DFT (Figure 4.10). The NIR molecular orbital can be constructed as a superposition of the LUMO and LUMO+1 orbitals. Since they differ only by the weight on the central hydrogen pair, they are near-degenerate and thereby usually imaged simultaneously in experiments.[265,283,284] Note that because of the large tip-molecule distance in our experiment,

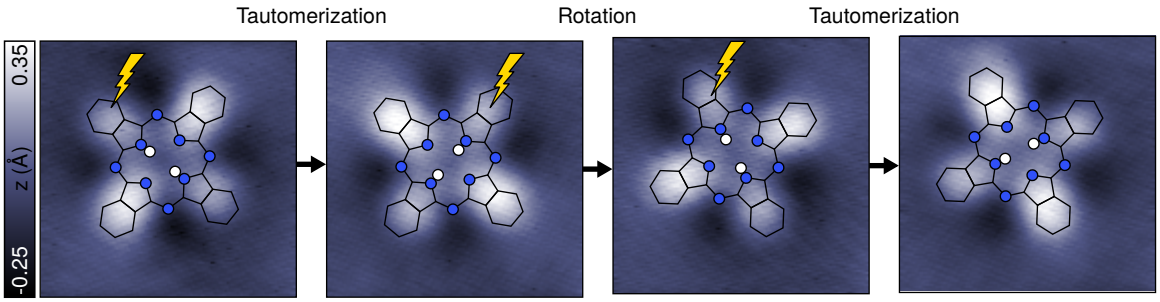

Figure 4.11: Tip-induced tautomerization and rotation of H_2Pc^- on MgO/Ag(100). The first left scan shows the inital state. The three following are recorded after a millisecond-duration bias pulse to 1 V at 200 fA on the positions marked with a thunderbolt symbol. We observe two tautomerizations and one rotation event. $2 \times 2\,\mathrm{nm}^2$, −100 mV, −200 fA.

electron density on the macrocycle cannot be resolved; only the lobes located on the four outermost benzene rings are imaged. We attribute this molecular species to charge-neutral H_2Pc. Evidently, the extent of its orbitals is simply too small to accommodate the smallest integer charge, one electron, in the face of the large intramolecular Coulomb repulsion on the decoupling layer. Hence, the electron affinity level of adsorbed H_2Pc must slightly lie above the work function of MgO/Ag(100).

In the small-gap case, the PIR and NIR are imaged to be two-fold symmetric, and differ in this case only by a 90° rotation (Figure 4.9b). We find that this type of molecule is consistently unstable under positive sample bias and undergoes tautomerization, which geometrically corresponds to a rotation by 90°. While mapping the NIR, these switching events occurs at a rate comparable to the bandwidth of STM, as evidenced by the fuzzy appearance in the differential conductance map. As a result, the superposition of two configurations is recorded. Here, the contribution of the tautomer different from that found at the PIR dominates the image. Yet, some DOS is also detected in the NIR in positions where the PIR has maxima (white arrows in Figure 4.9b). We conclude that both ion resonances stem from the same orbital, the gas-phase LUMO, and thus represent the SOMO and SUMO of H_2Pc^-. In the absence of tip-induced tautomerization, the singly (un)occupied orbitals would be spatially degenerate as in the case of chGNRs (Section 4.1). The conductance gap thereby arises from electronic correlation alone in this species,[274] and is much larger than what we had observed in chGNRs. We attribute this difference to the high charge density required to accommodate the surplus electron within a highly confined orbital. It has been found that defects at the MgO/Ag interface can locally alter the work function,[280,285] which is a possible cause for the occurrence of two charge states.

We will now investigate the tautomerization of H_2Pc^- on MgO more closely. Since the thermal switching rate at our temperature of 1.3 K is essentially zero,[284,286–288] we can stably alternate between tautomers by injecting electrons into the SUMO. A single H_2Pc^- is shown in Figure 4.11. As here we image it within the conductance gap, no tautomerization takes place. The molecular orbitals only indirectly participate in tunnelling,[289] and the molecule appears smaller. The isoindole units are imaged as lobes, with one opposing pair lower

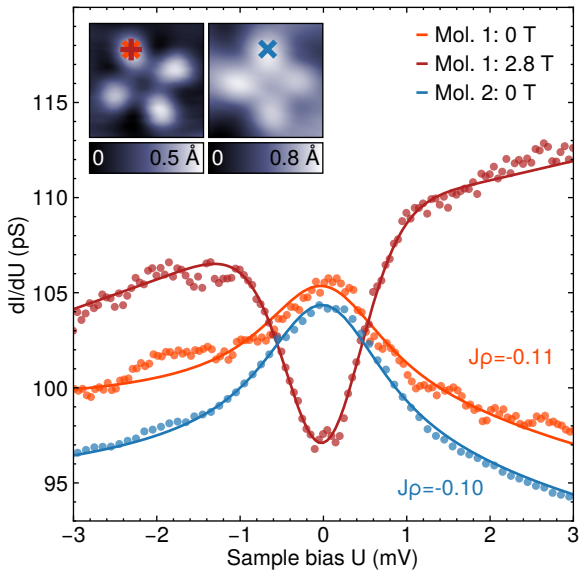

Figure 4.12: Sensing the magnetic state of H_2Pc^- on MgO/Ag(100). Shown are IETS traces of two molecules, with and without external magnetic field. We observe a weak Kondo resonance, which readily splits with the magnetic field, confirming that $S = 1/2$. Spectra have been taken at 5 GΩ. Insets show STM scans of size $1.65 \times 1.65\,\mathrm{nm}^2$. Imaging conditions from left to right: −200 fA at −100 mV and 25 pA at 100 mV.

than the other. Considering that the SOMO and SUMO have weight on the hydrogen pair (gas-phase LUMO Figure 4.10), we allocate the H binding site to the two brighter lobes. By performing short bias pulses to 1 V, the SUMO is transiently populated and tautomerization is induced. Under the same conditions, the molecule may also perform a rotation.

H_2Pc^-, being singly charged, is expected to form a spin doublet. In the high resolution differential conductance spectra in Figure 4.12, we indeed observe a faint Kondo resonance characteristic of a $S = 1/2$ magnetic impurity. Since the Kondo coupling strength $J\rho$ to the Ag(100) conduction electrons is substantially weakened by the MgO layer, the peak is particularly narrow.[11] From its width, we determine[83] $T_K = 2.3$ K. Application of a strong out-of-plane magnetic field splits the resonance into a pair of conductance steps. Their position matches exactly with the Zeeman transition energy of a free $S = 1/2$ at 2.8 T as the fit gives $g = -2$. We can thereby confirm the spin doublet character of H_2Pc^-.

Its two-level spin state makes H_2Pc^- an excellent candidate for a molecular spin qubit. Kovarik *et al.*[13] have recently shown that the spin transfer torque exerted onto charged pentacene by spin-polarized RF current can lock to its Larmor precession and produce a magnetic resonance similar to conventional ESR-STM. The hallmark of this effect is the observation that spin-polarized tunnelling into SOMO and SUMO pumps the spin polarization to be opposite to that of the tip, which in turn gives increased tunnel magnetoresistance. With increasing current and tip polarization, this effect should intensify.

We here attempt to reproduce the magnetoresistive effect between H_2Pc^- and a spin-polarized Fe tip in an increasing external magnetic field, see Figure 4.13. As a reference for the tip polarization magnitude η, we consult the spin-flip excitations on of Fe/MgO. We observe a larger spin-pumping effect in Fe at higher fields, indicating that the tip polarization has increased. On H_2Pc^-, we encounter evidence of molecular spin transfer torque. Since these measurements are conducted in CC mode, an increase in tunnel magnetoresistance manifests as a decrease in tip height z. We obtain consistently smaller tip-molecule separations at

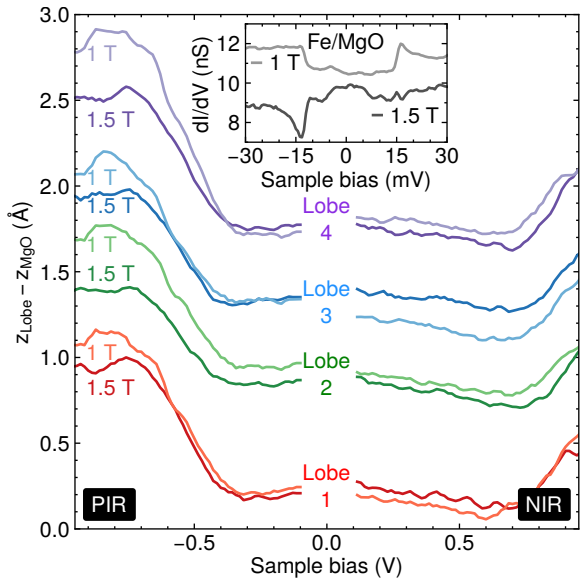

Figure 4.13: Probing spin transfer torque in H_2Pc^-. Shown are four sets of traces of $z(V)$ at $I = 70\,\text{fA}$, one for each isoindole unit of the molecule, for two magnetic fields. Reference curves on plain MgO have been subtracted to eliminate drift. The inset shows the spin-flip excitations of Fe/MgO from which the degree of tip polarization at each field can be deduced. Sets of curves are shifted for clarity.

the higher field when the bias voltage is tuned to the positive ion resonance. The effect is absent for the NIR, where the two sets of curves mostly coincide. The behaviour is consistent across the four lobes of H_2Pc^-, indicating that the magnetic moment is equally distributed between the ligands. It is remarkable that this effect persists even at the very low currents used ($I = 70\,\text{fA}$). Since spin-transfer torque competes with a magnetic damping equivalent to the longitudinal relaxation time, this implies an approximate lower bound for H_2Pc^- on MgO/Ag(100) at $T_1 = e/I = 2.3\,\mu\text{s}$. The dominant relaxation mechanism for a $S = 1/2$ impurity is the Kondo scattering by substrate electrons. Our value for T_1 approaches those measured for the single-atom magnet Fe/MgO[29,30] and is higher than what was found in charged pentacene on MgO with currents in the pA range.[13]

4.3 Preserving charge neutrality via self-decoupling

As we have seen in the case of chGNRs and H_2Pc, ultrathin MgO is a highly efficient decoupling layer with an unusually small work function. However, the magnetic properties of adsorbates are highly modified and therefore difficult to anticipate, which presents a challenge to the rational chemical design of molecular spins. For instance, it was recently shown that FePc, usually in a $S = 1$ configuration,[290] lowers its multiplicity upon adsorption on MgO/Ag(100).[11,14] Here, we will take here a chemical approach to remedying this effect. We study the related iron tetraphenylporphyrin (TPP), which by virtue of its alternate ligands, has a self-decoupling quality and retains its spin state.

The chemical structures of FeTPP and its chlorinated form FeTPP-Cl is shown in Figure 4.14a-b. Much like FePc, it consists of a tetrapyrrole (I) macrocycle containing a central Fe, but has four phenyl rings (II) attached to the nitrogen sites of the isocyanide (III) linkers. The latter allow for a saddle-shaped adsorption geometry in which a part of the molecule is lifts itself off the surface. This intrinsic decoupling allows observing sharp spin-flip excitations in tunnelling spectra when adsorbed on Au(111), contrary to bare FePc.[291] The transitions are attributed to a triplet ($S = 1$) ground state with a large easy-plane anisotropy $D = 7.4\,\text{meV}$. The chlorinated form (Figure 4.14b) on the other hand has been shown to adopt a quadruplet ($S = 3/2$) ground state on Au(111), with a much smaller easy-plane anisotropy of $D = 850\,\mu\text{eV}$.[292–294]

To compare the effect of self-decoupling with that of an additional decoupling layer, we deposit FeTPP and FeTPP-Cl via sublimation of powder-form FeTPP-Cl onto MgO in-situ. We obtain a random distribution of molecules on both the underlying metal and insulating patches, as shown in Figure 4.14. The majority of molecules are thermally dechlorinated during sublimation.[292] On Ag(100), FeTPP is imaged as a rectangular hump with four surrounding circular lobes. FeTPP-Cl appears similar, but with a less pronounced cen-

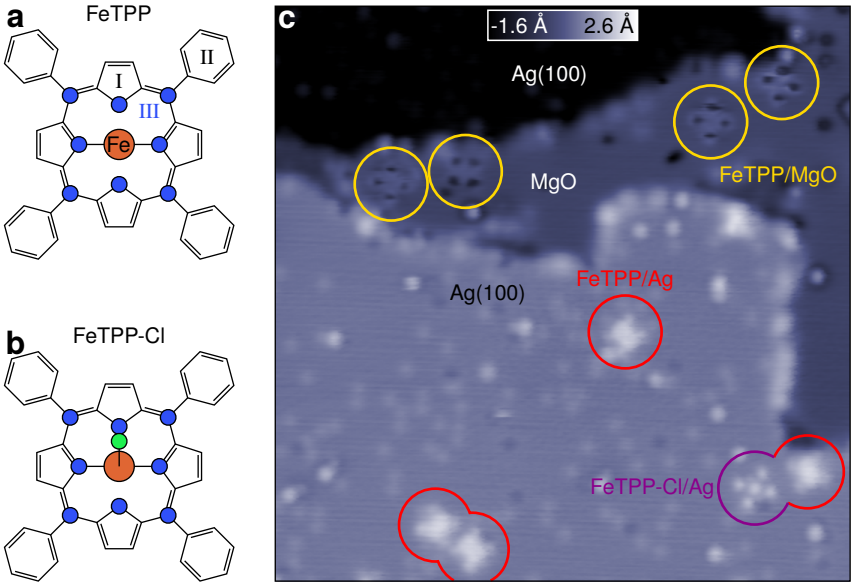

Figure 4.14: Self-decoupling of iron porphyrins on MgO. **(a,b)** are the chemical structures of the investigated molecules. The chlorine atom vertically bound to Fe is shown in green. **(c)** STM scan of Fe, Ti, FeTPP and FeTPP-Cl on Ag and MgO. $15 \times 15\,\text{nm}^2$, 80 mV, 50 fA.

tral feature. Spin-flip spectroscopy of the metal-adsorbed species reproduces the magnetic signatures previously found for FeTPP and FeTPP-Cl on bare Au(111).[292] By fitting the third-order inelastic tunnelling model (Figure 4.15a), we extract values for the easy-plane anisotropy slightly larger than those found previously; this could be caused by a minor difference in the adsorption geometry on Ag(100) versus Au(111).[295]

On the insulating MgO islands, FeTPP and FeTPP-Cl are imaged very differently. Due to the combined effect of self-decoupling and an efficient decoupling layer, the molecules are only weakly adsorbed and easily moved to the island's borders when scanning the surface (Figure 4.14c). We find they can be imaged only within the conductance gap at large tip-molecule separations, where the molecular orbitals do not significantly partake in tunnelling. Under these conditions, both types appear cloverleaf-shaped, with one displaying a bright center. We attribute this species to FeTPP-Cl. The four lobes stand out as dark depressions compared to the surrounding insulator. This local suppression of the density of states was already observed in H_2Pc adsorbed on MgO in Section 4.2.

Remarkably, we find that the magnetic excitation spectrum is only slightly modified by the insertion of the MgO decoupling layer between the molecule and Ag(100) (Figure 4.15a). Considering the similarity, there is no indication that the total spin state is altered by the change of substrate. We attribute the resilience of the magnetic state to the lifted adsorption geometry in FeTPP and FeTPP-Cl. Since the distance between molecule and metal is en-

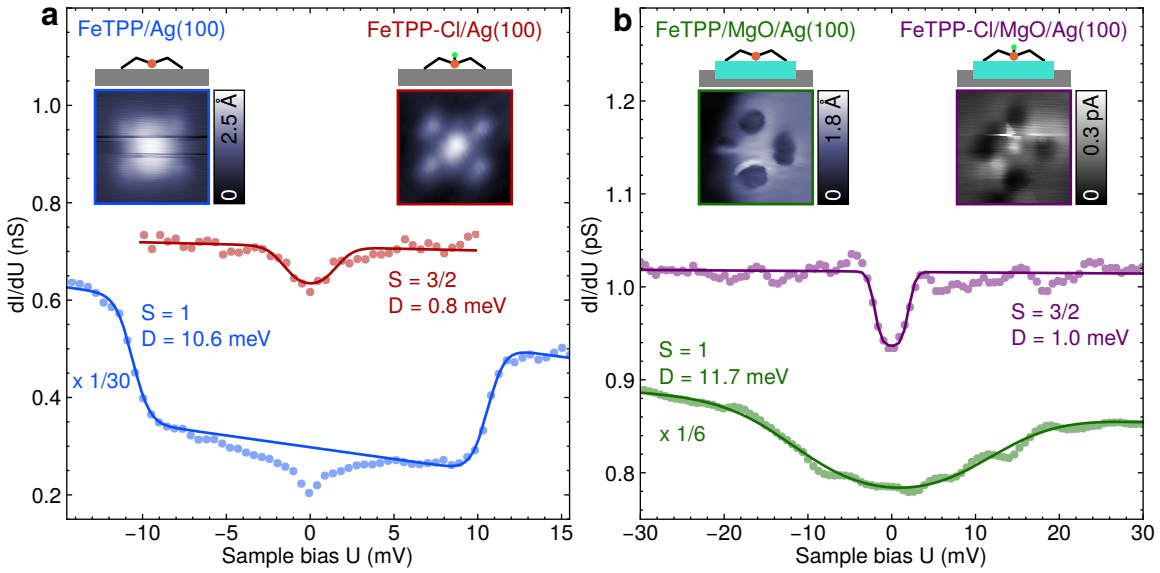

Figure 4.15: IETS of FeTPP and FeTPP-Cl on **(a)** Ag(100) (R = 50 and 100 MΩ) and **(b)** on MgO/Ag(100) (R = 15 and 80 GΩ). Insets show STM scans. Spectra were recorded on the center of each molecule. Scan size 2.5 × 2.5 nm^2 and 1.5 × 1.5 nm^2 in **(a)** and **(b)**, respectively. Imaging conditions, from left to right: 20 pA at 15 mV, 200 fA at 30 mV, 100 fA at 60 mV, and 80 mV. Curves are scaled by the indicated factor. The dip in conductance at zero bias in FeTPP/Ag(100) is due to an electronic artifact and has been excluded from the fit.

hanced, transfer of integer charge onto this small capacitance is energetically unfavorable.[67] This conclusion matches the earlier observation that the similarly sized but fully planar H_2Pc does undergo singly anionic charging (Section 4.2). Similarly, in the case of chGNRs on MgO/Ag(100), highly anionic states are realized as a consequence of their extended and fully planar nature, which correspond to a large interface capacitance.

Summary of Chapter 4

In this chapter, we studied the interplay of charge transfer with electronic decoupling by placing single molecules on ultrathin layers of the insulator MgO. This was found to have several consequences. Due to the suppressed tunnel coupling to the underlying metal, molecular orbital resonances could be probed with extraordinary resolution in chiral graphene nanoribbons and phthalocyanine. The low work function of MgO/Ag(100) also enables substantial anionic integer charge states: in the case of chGNRs, we identified n-doping with up to 19 excess electrons. H_2Pc, on the other hand, was found to occur both in a neutral and singly anionic state, the latter forming a spin-doublet state.

The reduction of metallic screening also enhanced the effect of intramolecular electron-electron repulsion. This manifested in the opening of a correlation gap in chGNRs and H_2Pc^-. We therein discovered an interesting interplay of charging, Coulomb correlations and geometry. In chiral graphene nanoribbons, the charge is predictably determined by length, and alternates between an even-numbered closed-shell configuration to an odd-numbered open-shell state with a distributed magnetic moment. In the much smaller tetrapyrroles, larger intramolecular correlation was able to prevent charge transfer entirely. This was especially pronounced in the specially ligated macrocycles, FeTPP and FeTPP-Cl, which retained their intrinsic spin on MgO due to a non-planar adsorption geometry. Due to electronic decoupling effect of MgO, the Kondo effect was significantly weakened in all molecular species, which we exploited to perform a spin pumping experiment in H_2Pc^-.

Chapter 5

Quantum coherence in the scanning tunnelling microscope

We have realized several instances where a molecular two-level electronic spin system also exhibits a high degree of decoupling in the preceding experiments: open-shell chGNRs, H_2Pc^-, VCp_2 and FeTPP-Cl. In these systems, we also expect an enhanced value for T_1 by virtue of a thin MgO decoupling layer or self-decoupling via ligands. This combination makes them exciting candidates as molecular spin qubits that can be addressed directly in STM.

Whether their spin coherence T_2 is sufficiently long for quantum computation, can only be assessed in a magnetic resonance experiment. As a preliminary step, we here demonstrate high-resolution ESR-STM, using the experimental setup developed in Section 5.1, of a single titanium atom. We will then theoretically explore a scheme to also sense nuclear spins in single atoms and molecules by combing nuclear magnetic resonance with ESR-STM in Section 5.2.

5.1 Electron spin resonance of a single titanium atom

In Chapter 1 and Chapter 2 we have covered the seminal technique ESR-STM and the practical concepts involved therein. In this section, we will test the new experimental setup against a known system to probe if the energy resolution and signal amplitude attained in our new instrument is sufficient to spectroscopically probe and quantum-coherently control new molecular spin qubits.

ESR-STM was first demonstrated on isolated Ti atoms adsorbed onto bilayers MgO on Ag(100) by Yang *et al.*[28] and it has since become an often reproduced and expanded on experimental platform.[37–39,104,106–119] On the rocksalt lattice structure, Ti naturally occurs in two species: adsorbed directly onto the oxygen atoms (Ti_O), or in the "bridge" configuration between two O sites (Ti_B). We focus on the latter, given its greater stability. Ti_B possesses an electronic spin $S = 1/2$, a nearly isotropic g-factor, and a natural rarity of nuclear moments (13 %)[296] that would give heterogeneous broadening. Given that it approximately behaves as a free unpaired electron, we choose Ti_B as our benchmark system of minimal complexity.

Iron and titanium were deposited on top of bilayer MgO/Ag(100) via in-situ sublimation as described in Section 2.1. This results in isolated adatoms on insulating patches of MgO shown in Figure 5.1b. Since the coverage with MgO is small, a comparatively large amount of Fe and Ti was sublimated to have a sufficient quantity of atoms on the insulator to spin-polarize the tip by picking up Fe (Section 2.2). After transferral of 13 atoms to the tip, we observe strong spin pumping and conductance step asymmetry in tunnelling spectra on the two highlighted Fe and Ti atoms under an out-of-plane magnetic field on the order of 500 mT (Figure 5.1c). These features indicate a high degree of tip polarization (Section 1.3.2). The low-energy inelastic steps, corresponding to the spin-flip transition $m_s = -1/2 \rightarrow 1/2$, and a large apparent height compared to Ti_O[28] confirm the Ti atom highlighted in Figure 5.1b as Ti_B, which will be the subject of our experiment.

The spin-polarized tip is then stabilized above the Ti_B in constant-current mode and the magnetic field tuned to $B \approx 390\,\mathrm{mT}$ such that f_L lies within the frequency window of 10 to 12 GHz where the coaxial antenna termination is well coupled to the tip (Section 2.4). A relatively large DC voltage bias of 75 mV and a reduced feedback current setpoint of 10 pA are chosen such that the atom is perturbed minimally by the tip, which will be rationalized in the following. Finally, the RF tone f applied via the antenna is swept at a constant junction RF amplitude of $U_{RF,J} = 8.5\,\mathrm{mV}$, fully compensating the transfer function. At approximately f_L, we observe a sharp peak of height $\Delta I_{ESR} \approx 20\,\mathrm{fA}$ that we attribute to ESR of Ti_B as detected by the elastic magnetoconductance between the cluster of Fe atoms on the tip and Zeeman-polarized Ti_B (Figure 5.1a). By increasing B in increments of 7 mT, the resonance rigidly blueshifts as seen in Figure 5.1d, confirming its magnetic character.

The TF of our RF circuit has been characterized up to the generator's bandwidth of 20 GHz. By adjusting B, the resonance is tuned into two higher frequency ranges (Figure 5.1e-f). Around 15 GHz, the resonance is stronger and broader because of the larger feedback cur-

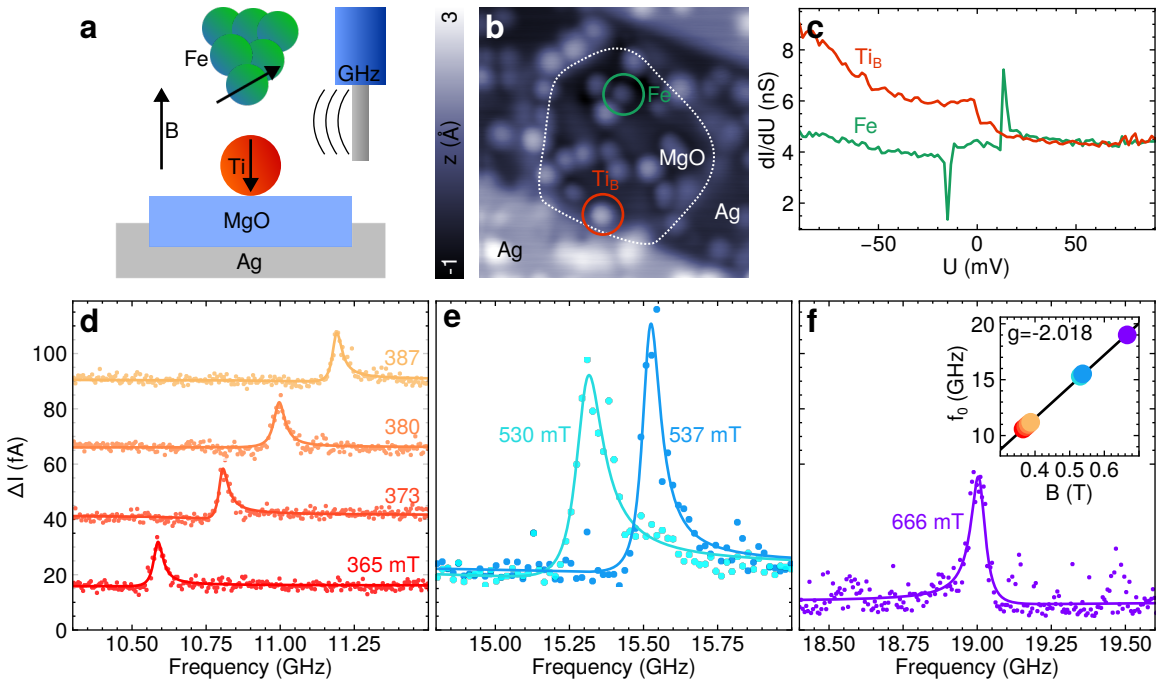

Figure 5.1: Electron spin resonance of a single Ti_B atom on MgO/Ag(100). **(a)** Sketch of the tunnelling junction formed between Ti_B and spin-polarized tip irradiated with RF. **(b)** STM topographic scan of the investigated MgO island. Circles mark Ti_B and Fe. $10 \times 10\,nm^2$, 50 mV, 10 pA. **(c)** Inelastic tunnelling spectra on the two highlighted atoms display significant spin polarization. Bottom row: ESR spectra at different magnetic fields taken using the same tip, with their respective Fano-like fits. We plot ΔI versus f. **(d)** Resonances at four different fields, here stacked by 25 fA. Feed back is engaged at $I_{DC} = 10\,pA$. **(e)** At higher fields using $I_{DC} = 40\,pA$. **(f)** At the highest frequency range, using $I_{DC} = 20\,pA$. Other parameters: $U_{DC} = 75\,mV$, $U_{RF,J} = 8.5\,mV$. Inset shows a linear fit of the resonance frequencies f_0 as a function of field B, which yields the g-factor.

rent employed. All ESR peaks recorded with this particular spin-polarized tip show a slight asymmetry. As introduced in Section 1.3.3, this is attributed to the simultaneous detection of longitudinal and transverse spin components via the elastic magnetoconductance. The Fano-like lineshape of Equation (1.17) gives a good fit to the resonances. As evidenced by the very small peak asymmetry, the transverse contribution for this particular tip is small, implying its easy axis to be mostly aligned with the external magnetic field. Note that at Figure 5.1f, the sign of the asymmetry parameter is reversed compared to the other resonances, indicating a re-oriented tip magnetization at the largest field. The shift of the resonance with B allows us to infer the longitudinal g-factor of Ti_B. A linear fit (Figure 5.1f) of f_L, as fitted, versus B gives $g = -2.018$, in good agreement with a previous study.[38]

We have so far neglected exchange coupling to the tip,[129] which acts as an effective magnetic field and causes an additional shift in frequency depending on the tip-adsorbate distance.[108] In our field sweep, we have varied the setpoint current, so the tip field experienced by Ti_B is slightly altered. It has also been shown that the magnitude of tip polarization depends on

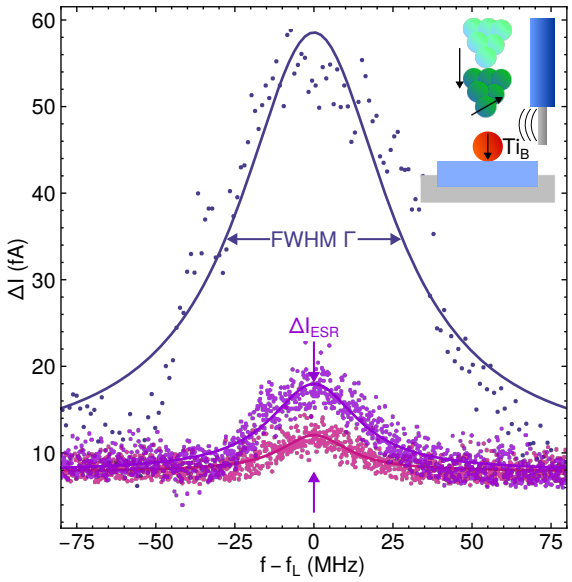

I_{DC} (pA)	ΔI_{ESR} (fA)	f_L (GHz)	Γ (MHz)
7.5	4	18.87	26
10	10	18.91	33
20	49	18.99	58

Figure 5.2: Probing the resolution limit of our ESR-STM implementation. The tip is approached towards the atom by increasing the feedback current setpoint. Fano fits give the peak amplitude ΔI_{ESR}, Larmor frequency f_L and FWHM Γ, see table to the right. The peak broadens due to an increase in the Rabi rate, and additional decoherence caused by tunnelling electrons. It also blueshifts due to increasing exchange coupling to the tip. $U_{DC} = 75\,\text{mV}$, $U_{RF,J} = 21\,\text{mV}$.

the magnetic field;[13,113] consequently, the tip field cannot be assumed constant for all fields. These effects introduce a small error in our determination of g.

The ability of ESR-STM to resolve fine couplings, such as those to nuclei, depends on the intrinsic peak width $\Gamma = \sqrt{1 + \Omega^2 T_1 T_2}/(\pi T_2)$. It captures the balance of the driving strength Ω with the relaxation and decoherence times T_1 and T_2. Generally, large T_1 and T_2 and small Ω will give the sharpest resonances. There are several mechanisms that limit these times in our experiment. For one, the inelastic Kondo scattering between the adsorbate and Ag(100) can efficiently reverse the spin of Ti_B with a single electron since the ground states are separated by $\Delta m_s = 1/2$. This is exponentially suppressed by the MgO decoupling layer, but still finite, as we saw in the case of H_2Pc^-. The same process occurs with the spin-polarized tunnelling electrons originating from the tip. These two mechanisms dominate T_1.[30] T_2 is limited by temporal fluctuation of magnetic couplings that introduce uncertainty in the Larmor precession frequency.[16] This is most trivially caused by unavoidable oscillation of the tip-adsorbate distance due to mechanical noise, which modulates the tip field. Field fluctuations are also constituted by elastic tunnelling of substrate and tip electrons, and the thermal reversal of the tip magnetization.[30,110] Other sources may be spin-spin coupling to nearby magnetic adsorbates or even the hyperfine interaction with fluctuating nuclear spins such as ^{25}Mg in the adsorption environment.

The spin relaxation and decoherence due to the flow of current and the tip field can both be mitigated by increasing the tip-adsorbate separation. Figure 5.2 shows the magnetic

resonance peaks for three different feedback setpoints with fits of Equation (1.17). Withdrawing the tip decreases its exchange coupling to Ti_B and thereby the tip field, which shifts f_L down by up to 120 MHz. If we assume both the tip and atom to be aligned with **B** in equilibrium, this is consistent with antiferromagnetic tip-adsorbate coupling.[108] The reduction in tunnelling current also enhances T_1 and T_2, and thereby decreases the peak width Γ. The influence of mechanical vibrations on T_2 is also lowered as the tip field is smaller in magnitude. The Rabi frequency Ω also scales with the tip coupling;[110] this effect contributes to decreasing the peak width even further, but also its amplitude. The decreased junction conductance also lowers the sensitivity of magnetoconductive readout. The gain in resolution therefore comes at the cost of signal strength. At the lowest current of 7.5 pA, we achieved $\Gamma = 26$ MHz, which corresponds to an energy broadening in the range of tens of neV. This resolution matches that obtained in another instrument operating at the same temperature,[39] which proves that the only sources of decoherence are those intrinsic to the system under study and the ESR-STM technique. We determine this set of parameters as our detection limit for an averaging time of 1 h, as the peak height $\Delta I_{ESR} = 4$ fA is equal to the peak-to-peak background noise level.

5.2 Theory of electron-nuclear double resonance

Coherent control of the electron spin in individual qubits, as demonstrated above, also provides the possibility of addressing intrinsic nuclear spin. The hyperfine and quadrupole interactions between electron and nucleus can act as an intermediary to electrically both drive and sense the nuclear state via the valence or ligand electrons. The indirect read out of the nuclear spin via electron tunnelling relies on state hybridization via the hyperfine interaction. This has previously been exploited in molecular junctions,[10,297,298] single magnetic adatoms in the STM[116,299,300] and donor spin qubits.[301]

For the application of individual molecules or atoms to quantum devices, access to nuclear spins is a seminal advancement: now each metal ion can host not only one, but two or more entangled qubits. Large numbers of individually addressable two-level systems are possible with higher electronic and nuclear spins where magnetic anisotropy and a quadrupole moment can provide the necessary zero-field detuning.[7] Furthermore, as nuclear spins can interact with their environment only indirectly via the weak hyperfine interaction or even weaker dipolar or quadrupolar couplings, the relaxation and coherence times are expected to be far superior to those of electronic spins.[300,302]

Apart from quantum computing applications, simultaneous electronic and nuclear control is also of relevance for quantum sensing. A large variety of ensemble measurement schemes known as ENDOR[17] leverage the interactions between electrons and nuclei. This routinely enables structure elucidation in complex bulk systems where hyperfine couplings are too fine to resolve with single-frequency methods. The underlying mechanism is the dynamic nuclear polarization following the saturation of electronic transitions.[303] If implemented using ESR-STM, this would allow sensing the intramolecular hyperfine or nuclear spin-spin

interactions in single molecules with atomic precision.

ESR-STM fundamentally differs from conventional bulk magnetic resonance methods in its fully electrical driving and readout via spin-polarized tunnelling. The inelastic fraction of the tunnelling current can drive both electron and nuclear spin far out of thermal equilibrium by an effect known as spin pumping[94,299] that we introduced in Section 1.3.2. Often, the associated excitation and relaxation rates are comparable or stronger than the actual magnetic resonance Rabi rates and the two effects combine. To investigate if the existing ENDOR schemes can be applied to ESR-STM, we will study theoretically the interplay of separate and simultaneous driving of electronic and nuclear transitions of single magnetic atoms in the presence of a spin-polarized current.

To this extent, we revisit the theoretical model first developed by Yang *et al.*[299] for single Cu atoms on MgO and apply it to a simpler representative system, ^{6}Li. We extend the treatment to higher order to include possibly spin-polarized Kondo-like scattering with tunnelling and substrate electrons. We then extract both ESR and indirectly detected nuclear magnetic resonance (NMR) spectra by rigorously evaluating the steady-state tunnel magnetoconductance. We then investigate a two-dimensional experiment, in which both ESR and NMR frequencies are swept.

To start, we focus on the simplest case of a single-atom magnet with a higher-spin nucleus: an electronic $S = 1/2$ coupled to a nuclear $I = 1$. This corresponds to a charge-neutral ^{6}Li. We can write its spin Hamiltonian as:[17]

$$\mathcal{H} = \mathcal{H}_{\mathrm{EZE}} + \mathcal{H}_{\mathrm{NZE}} + \mathcal{H}_{\mathrm{HFI}} + \mathcal{H}_{\mathrm{QPI}} \tag{5.1}$$

where the first two terms are the Zeeman effects of the form introduced in Section 1.1.1 for the electronic and nuclear spins. We set an isotropic $g_{\mathrm{e}} = -2$. We furthermore neglect the much smaller nuclear Zeeman effect (NZE) for now and set $g_{\mathrm{n}} = 0$. The hyperfine interaction couples the two spins to one another like

$$\mathcal{H}_{\mathrm{HFI}} = \hat{\mathbf{S}}^{\mathrm{T}}\mathbf{A}\hat{\mathbf{I}} \tag{5.2}$$

For simplicity, we assume an isotropic hyperfine coupling of typical magnitude: $A/h = 150\,\mathrm{MHz}$. The hyperfine tensor $\mathbf{A}$ is then diagonal. Many nuclei posses a sizeable quadrupole moment that can induce a zero-field splitting to the nuclear levels. It is included by

$$\mathcal{H}_{\mathrm{QPI}} = \hat{\mathbf{I}}^{\mathrm{T}}\mathbf{Q}\hat{\mathbf{I}} \tag{5.3}$$

We here also neglect the quadrupole interaction (QPI) for simplicity. We will re-introduce the two nuclear terms and the hyperfine anisotropy later.

Exact diagonalization yields six eigenstates, which disperse approximately linearly as seen in Figure 5.3a. In the absence of magnetic field ($B = 0$), we have two sets of states corresponding to $F = 1/2$ and $F = 3/2$, where $F = I + S$ is the coupled angular momentum quantum number. The only good quantum number at all fields is m_F, whose values are also included.

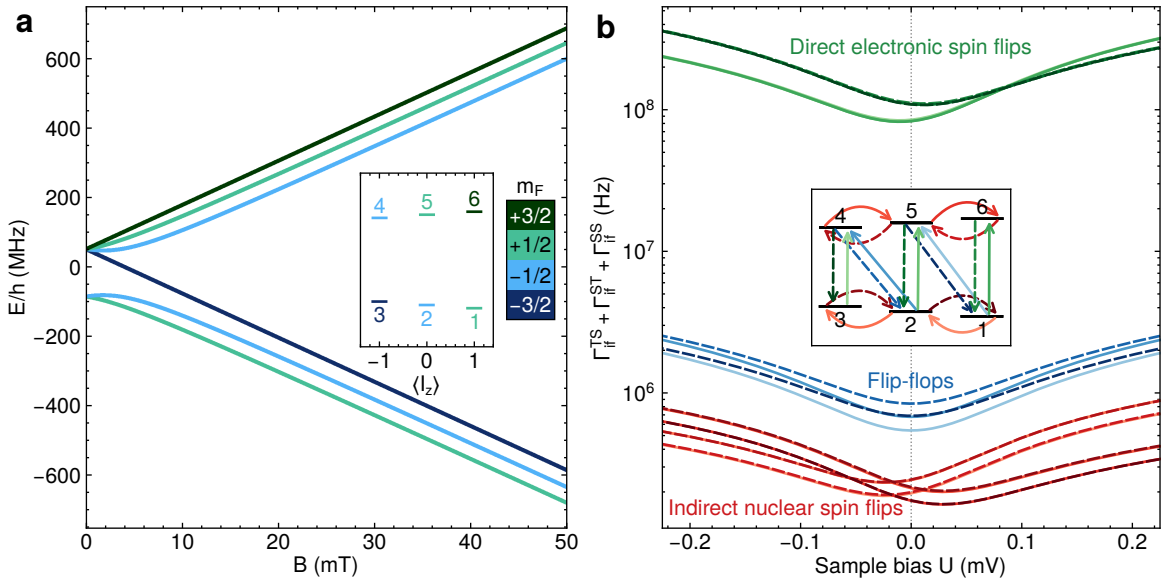

Figure 5.3: **(a)** Eigenstates of ^{6}Li as a function of external magnetic field. States are coloured by the total spin quantum number m_F. The inset shows the energy level diagram at $B = 50\,\mathrm{mT}$ arranged by $\langle I_z \rangle$. **(b)** Summed inelastic scattering rates for each pair of states as a function of bias. De-excitation rates are plotted as dashed lines. Voltages close to the Fermi level are chosen to discern all processes. Green, blue and red curves correspond to the direct electronic spin flip, flip-flop, and indirect nuclear spin flip transitions, respectively, as indicated in the inset. Excitation and relaxation rates are shown as solid and dashed lines. Calculation parameters: $B = 50\,\mathrm{mT}$, $g_e = -2$, $\eta = 0.4$, $G_{TS} = 1\,\mu\mathrm{S}$, $G_{SS} = 1\,\mu\mathrm{S}$, $J\rho = -0.1$, $T = 0.3\,\mathrm{K}$.

Since the nuclear spin does not experience a Zeeman effect here, two regimes occur under the influence of B: in the low-field limit, states split according to $\langle \hat{S}_z \rangle$, which vanishes for two of the states hybridized by A. At higher fields, the electronic Zeeman effect has overcome the hyperfine interaction: the states de-hybridize and split linearly. In this Paschen-Back limit the system is well described by two sets of three product states $|F, m_F\rangle \approx |m_S\rangle \otimes |m_I\rangle$:

$$
\begin{aligned}
|1\rangle &= |1/2, +1/2\rangle \approx |-1/2\rangle \otimes |+1\rangle \\
|2\rangle &= |1/2, -1/2\rangle \approx |-1/2\rangle \otimes |0\rangle \\
|3\rangle &= |3/2, -3/2\rangle \approx |-1/2\rangle \otimes |-1\rangle \\
|4\rangle &= |3/2, -1/2\rangle \approx |+1/2\rangle \otimes |-1\rangle \\
|5\rangle &= |3/2, +1/2\rangle \approx |+1/2\rangle \otimes |0\rangle \\
|6\rangle &= |3/2, +3/2\rangle \approx |+1/2\rangle \otimes |+1\rangle
\end{aligned}
\tag{5.4}
$$

Where we have enumerated the states by increasing energy. The lowest set of three states has a negative electron spin, and the upper set positive electron spin.

To simulate ESR, NMR, and continuous wave ENDOR (CW-ENDOR) in the STM, we must combine the effects of spin pumping and magnetic resonance. For this, we perform a rate calculation.[303] By summing the inelastic scattering rates with magnetic resonance driving rates of the electronic and nuclear spins, we can solve for the steady-state populations of the states in Equation (5.4) using the Pauli master equation given in Equation (1.15). This approach is justified since in our continuous-wave experiment, the low detection bandwidth of STM effectively averages out the population dynamics.[299] Then, we can extract the change in magnetoconductance ΔG between the tip and the impurity, which is the experimentally measured quantity.

To obtain the scattering rates, we turn to the inelastic tunnelling model of Ternes[75] as described in Section 1.3.2. Both tunnelling and substrate electrons are allowed to scatter with the impurity; here we consider processes with up to two electrons. We also explicitly neglect direct spin flip scattering of the nuclear with single electrons. It can therefore only interact with the environment via its coupling to the electronic spin. Processes where the impurity gains two or more $\hbar$ (e.g. $|3\rangle \leftrightarrow |5\rangle$) are not included as they are forbidden by conservation of angular momentum.

In our description, there are three distinct scattering pathways, which are sketched in the inset of Figure 5.3b. The first and dominant rate is the direct electronic spin flip excitation, in which angular momentum of the tunnelling or substrate electrons is transferred to the impurity's unpaired electron spin. These transitions are $|1\rangle \leftrightarrow |6\rangle$, $|2\rangle \leftrightarrow |5\rangle$ and $|3\rangle \leftrightarrow |4\rangle$.

The second is the flip-flop mechanism, which transfers angular momentum between the impurity's electronic and nuclear spins without affecting that of the tunnelling or substrate electron. These transitions are $|1\rangle \leftrightarrow |5\rangle$ and $|2\rangle \leftrightarrow |4\rangle$. It is enabled by hyperfine coupling alone and must therefore vanish at large enough magnetic fields as the state hybridization becomes minimal.

The direct electronic spin flip and flip-flop mechanisms are triggered by scattering of a single electron. When considering also processes with two scattering events, the former two effects can combine. This gives the third scattering pathway, which are indirect nuclear spin flips: $|1\rangle \leftrightarrow |2\rangle$, $|2\rangle \leftrightarrow |3\rangle$, $|4\rangle \leftrightarrow |5\rangle$ and $|5\rangle \leftrightarrow |6\rangle$. In these processes, an intermediate state is scattered into or out of with a flip-flop event followed or preceded by an electronic spin flip, e.g. $|1\rangle \rightarrow |5\rangle \rightarrow |2\rangle$. These nuclear T_1 processes will weaken with increasing magnetic field as they are rate-limited by the flip-flop mechanism. They scale with the Kondo coupling strength $J\rho$, which we have set here to the value obtained in Section 4.2 for H_2Pc^- on MgO/Ag(100). Despite T_K being small, these Kondo-like processes are of similar in order of magnitude as the flip-flop mechanism. Higher-order scattering also formally augments the direct electronic spin flip and flip-flop rates with processes such as $|1\rangle \rightarrow |6\rangle \rightarrow |6\rangle$.

Figure 5.3b shows the combined scattering rates $\sum_{lk} \Gamma_{if}^{lk}$, as obtained by Equation (1.9), of the three mechanisms considered. We here assume a positively polarized tip (majority spin up, $\eta > 0$). The rates for each scattering pathway decrease in magnitude in the order that we introduced them. Note that due to the similar transition energies between the states, many

curves nearly overlap.

Detailed balance would require that the relaxation rates be larger than the excitation rates by the respective Boltzmann factor regardless of the bias voltage U. Here, this rule is only obeyed by the flip-flop rates, which are independent of the tunnelling electron's spin. Due to the tip polarization, the electronic and nuclear spin flip rates are instead asymmetric with respect to the direction of current flow. For direct electronic spin flips, the excitation rates far exceed the relaxation rates for tip-sample tunnelling, as already described in Section 1.3.2. The opposite is true for sample-tip tunnelling. As a result, we expect the electron spin to invert at sufficiently large positive bias, and a lowering of the electronic effective temperature at negative bias. The highest attainable electron spin polarization by this mechanism is $\pm\eta$ for positive and negative bias, respectively.[94] Similar behaviour of the nuclear spin temperature is expected due to the asymmetry of indirect nuclear spin flips. In contrast to the direct electronic spin flips, the nuclear spin flips drive the nuclear moment to be opposite in sign to η at positive bias.

The interplay of these three mechanisms becomes apparent when analysing the steady-state populations as a function of bias voltage. Note that this emulates a constant-height measurement. For now we disregard the indirect nuclear spin flips and refer to Figure 5.4a. We observe a transfer of population towards the terminal states $|6\rangle$ at positive bias and $|3\rangle$ at negative bias. Consequently, the electron and nuclear spin polarizations are enhanced significantly over their thermal values ($U = 0$) and change sign with bias polarity. Notably, the nuclear polarization quickly becomes larger in magnitude than the electronic polarization

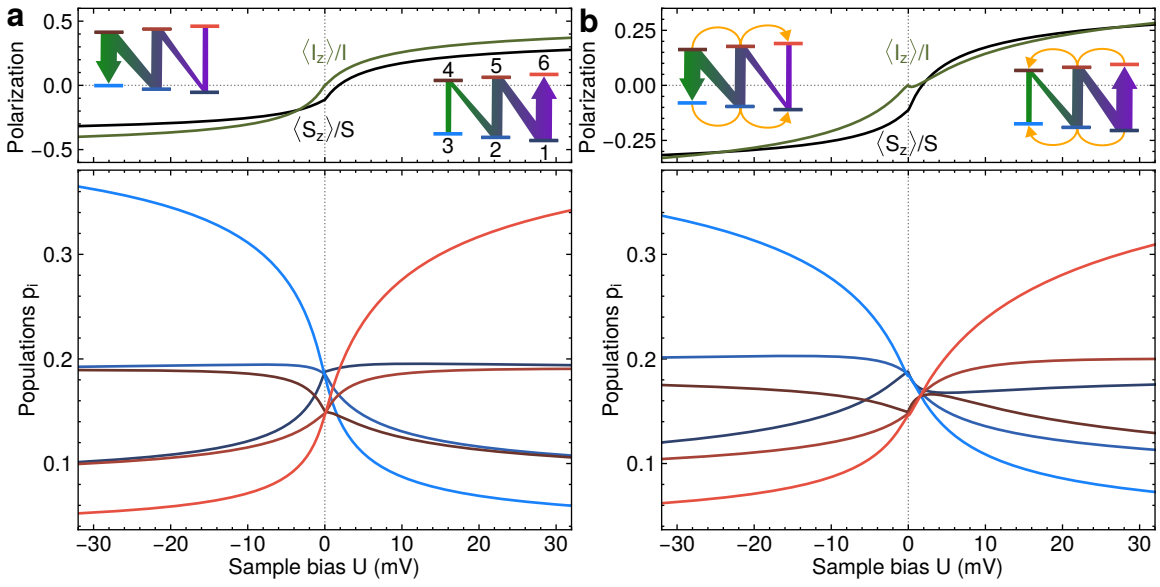

Figure 5.4: The steady-state populations (bottom row) and the resulting electron and nuclear spin polarizations (top row) as a function of bias voltage. In **(a)**, the indirect nuclear spin flip mechanism has been suppressed. In **(b)**, all three mechanisms are active. Insets sketches show the population flow due to scattering along the dominant paths indicated by arrows. Calculation parameters identical to Figure 5.3 except $G_{\mathrm{TS}} = 10\,\mathrm{nS}$.

due to its large lifetime T_1, as no dedicated nuclear relaxation channel is available.

The underlying mechanism is best understood by considering an instantaneous application of U (a voltage pulse) after the impurity has been in thermal equilibrium. Before, at $U = 0$, states $|1\rangle$, $|2\rangle$ and $|3\rangle$ have the highest occupations. Inelastic spin-polarized tunnelling at $U > 0$ then preferentially scatters into states $|6\rangle$, $|5\rangle$ and $|4\rangle$. States $|4\rangle$ and $|5\rangle$ are in turn connected to states $|1\rangle$ and $|2\rangle$ via flip-flop relaxation. As a result, state $|3\rangle$ is drained and its population transferred mostly to $|1\rangle$. Finally, the fast direct electronic spin flip process scatters into $|6\rangle$ and completes the population avalanche. There, relaxation is inefficient: no flip-flop transition connects to it, and the spin-up polarized current lacks spin-down electrons to scatter back into $|1\rangle$. At negative bias, the opposite occurs: population of $|1\rangle$ is funnelled into $|3\rangle$.

Let us now consider the effect on the non-terminal states. For purely single-electron scattering, these two pairs of states, connected to another only by flip-flop scattering, are perturbed only weakly. At large biases, the flip-flop excitation rate cannot accumulate populations as the direct spin flip into the terminal states dominates the flip-flop relaxation rate. Consequently, their populations remain equal with increasing current.

Two-electron scattering circumvents this bottleneck (Figure 5.4b). An indirect nuclear spin-flip followed by a fast electronic spin flip aids flip-flop relaxation in establishing population differences. As a result, all state populations fan out with U. As we will show, this effect enhances magnetic response when probing magnetic resonance transitions between these pairs.

Since the avalanche process is weakened, and there now exists a T_1 mechanism, the nuclear polarization now lies below the electronic polarization for a large range of bias voltages. This holds until the avalanche effect, linear in U, dominates these higher-order effects, sublinear in U. This limit is not reached in typical conditions for ESR-STM where the smallest practicable currents are employed to limit decoherence. In the following, we will therefore always include indirect nuclear spin flips.

With the magnetic atom's electronic and nuclear spins efficiently initialized by spin pumping, we now drive the system using magnetic resonance. Two RF voltages are applied to the tunnelling junction, with frequencies f_n and f_e and different amplitudes. They are transduced to two RF fields $\mathbf{B}_{1,\mathrm{n}}$ and $\mathbf{B}_{1,\mathrm{e}}$ oriented along the x-axis. Their effect on the level populations is given by the steady-state solution for $\langle \hat{S}_z \rangle$ of the Bloch equation, as discussed in Section 1.3.3. Following Yang *et al.*[299], we define the ESR and NMR rates as

$$\begin{aligned} \Gamma_{if}^{\mathrm{ESR}}(f_\mathrm{e}) &= \frac{(\Omega_{\mathrm{ESR}} m_{if})^2 T_{2,\mathrm{e}}}{4(\pi(f_\mathrm{e} - f_{if})T_{2,\mathrm{e}})^2 + 1} \\ \Gamma_{if}^{\mathrm{NMR}}(f_\mathrm{n}) &= \frac{(\Omega_{\mathrm{NMR}} m_{if})^2 T_{2,\mathrm{n}}}{4(\pi(f_\mathrm{n} - f_{if})T_{2,\mathrm{n}})^2 + 1} \end{aligned} \tag{5.5}$$

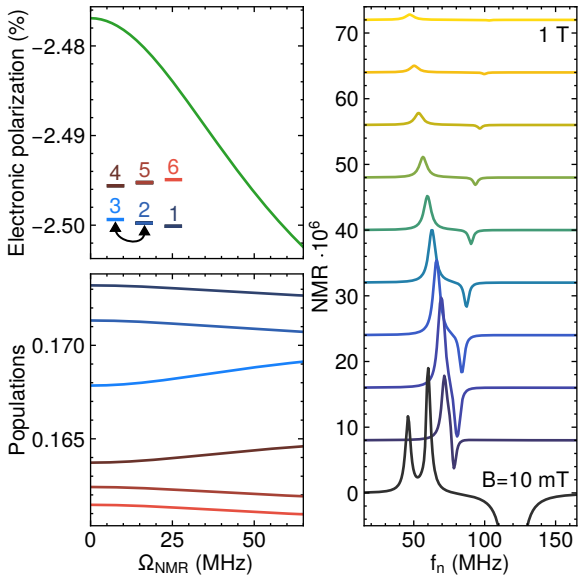

Figure 5.5: Effect of NMR driving at $U = 17\,\mathrm{mV}$ and large tip-sample separation. On the left, electron spin polarization and level populations are shown at $B = 10\,\mathrm{mT}$. On the right, the evolution of NMR spectra with linearly increasing field. Other calculation parameters identical to Figure 5.4 except $G_{\mathrm{TS}} = 10\,\mathrm{pS}$ and $T_{2,\mathrm{n}} = 100\,\mathrm{ns}$.

where the matrix elements of the appropriate spin operator ($\hat{S}_x$ or $\hat{I}_x$) are

$$m_{if} = \frac{1}{\hbar}\langle f|\hat{L}_x|i\rangle \tag{5.6}$$

This accounts for the fact that the different nuclear sublevels m_I will experience different driving strengths depending on their orientation with respect to $\mathbf{B}_{1,\mathrm{n}}$. For each rate, we only allow transitions between states of the appropriate energy scale. In this way, f_{n} (f_{e}) will only drive NMR (ESR) transitions even if the resonances should overlap. Since $m_{if} = m_{fi}$, the magnetic resonance rates lead to equal populations of $|i\rangle$ and $|f\rangle$, an effect known as saturation.[17]

The dependence of the magnetic resonance rates on the actual RF voltages are holistically included in the scale factors Ω_{ESR} and Ω_{NMR}. We make no statement on the actual driving mechanism for now, apart from the fact that the driving strengths must be significantly different. We assume that $\Omega_{\mathrm{NMR}} \ll \Omega_{\mathrm{ESR}}$ and $T_{2,\mathrm{n}} \gg T_{2,\mathrm{e}}$, in line with experiments.[116,299,300] Crucially, we have our NMR driving act directly on the nuclear spin, in a largely field-independent manner.

To address all NMR transitions individually, we now include the nuclear Zeeman effect with a small nuclear gyromagnetic ratio $\gamma_{\mathrm{n}}/\gamma_{\mathrm{e}} = 10^{-3}$. Driving an NMR transition such as $|2\rangle \leftrightarrow |3\rangle$ close to thermal equilibrium (i.e. small G_{TS}) affects primarily the nuclear spin polarization as population flows from $|2\rangle$ towards $|3\rangle$, as shown in Figure 5.5. However, at relatively low magnetic fields, a small change in electron spin polarization is also induced. This has two causes: for one, due to the remnant state hybridization, population changes within each set of three states will affect $\langle\hat{S}_z\rangle$ as each state slightly deviates from $\langle\hat{S}_z\rangle = \pm 1/2$. Secondarily, the lower triplet of states ($|1\rangle$ to $|3\rangle$) actually slightly increases in population over states $|4\rangle$ to $|6\rangle$. and $\langle\hat{S}_z\rangle$ decreases. This is due to the fact that the inelastic substrate-substrate scattering rates are also affected by hybridization and slightly differ depending on m_I. The resulting drop in electron spin polarization can be read out by

a change in magnetoconductance due to the tip polarization η. We define the NMR signal as

$$\mathrm{NMR} = \Delta G / G_{\mathrm{TS}} = \eta \Delta \langle \hat{S}_z \rangle / S \tag{5.7}$$

where we use $\langle \hat{S}_z \rangle = \sum_i p_i \langle i | \hat{S}_z | i \rangle$. Through this mechanism, NMR can be read out via its effect on the electron spin polarization. However, due to small population differences between the states, the signal is relatively weak and quickly diminishes with increasing fields as the states de-hybridize. This decay is shown on the right in Figure 5.5. Experimentally, the magnetoconductive NMR signal has been observed in individual atoms with unusually strong hyperfine coupling[299] or at very small magnetic fields.[116] In both cases, the hybridization is strong. In principle, the NMR sensitivity could be improved by dynamic nuclear polarization via the avalanche effect at increased tunnelling currents, where it can overcome the indirect nuclear spin flip mechanism (Figure 5.4b). However, as the tip approaches, the exponentially rising exchange interaction with the atom[129] would quickly nullify the signal enhancement by de-hybridizing the spin states.[116]

Unlike NMR, ESR can be observed by magnetoconductance at all magnetic fields as the electron spin is read out directly. In Figure 5.6, we simulate the effect of electronic driving of $|3\rangle \leftrightarrow |4\rangle$. With the transition saturated, we have $p_3 \approx p_4$. Since the remaining, undriven states $|2\rangle$, $|5\rangle$, $|1\rangle$ and $|6\rangle$ are connected to $|4\rangle$ and between one another via combinations of the three scattering mechanisms, part of the thermal population of $|3\rangle$ is transferred to them in the same order. In this process, these four states, where $\langle \hat{I}_z \rangle = 0$, gain more population than $|4\rangle$ which has $\langle \hat{I}_z \rangle = -1$. As a consequence, the nucleus becomes positively polarized well over its thermal value for sufficiently large Ω_{ESR}. This is known as the Overhauser effect.[17,303]

In a f_{e}-swept spectrum, we observe three hyperfine peaks in the magnetoconductive ESR signal defined analogously to Equation (5.7). They correspond to the three transitions $|3\rangle \leftrightarrow |4\rangle$, $|2\rangle \leftrightarrow |5\rangle$ and $|1\rangle \leftrightarrow |6\rangle$. Their sign is positive, since the RF driving cants the electron

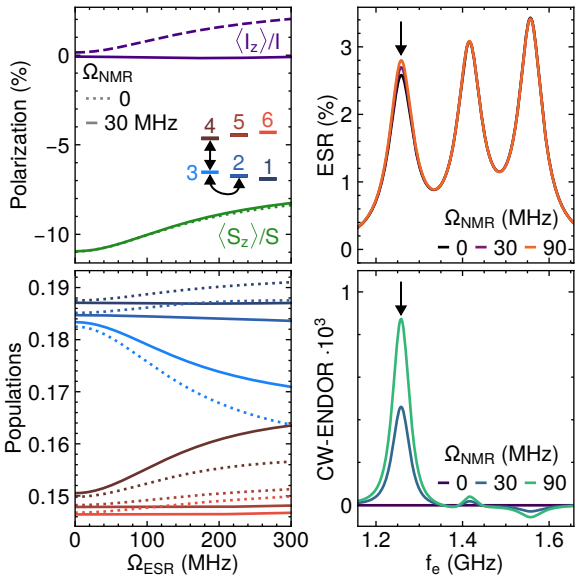

Figure 5.6: On the left, effect of individual and simultaneous ESR and NMR driving at $B = 50\,\mathrm{mT}$ and $U = 17\,\mathrm{mV}$. Electron and nuclear spin polarizations and level populations are shown with (continuous line) and without (dashed lines) additional NMR. On the right we evaluate the magnetoconductive signals ESR and CW-ENDOR as defined in the text. The response at $f_{\mathrm{e}} \approx 1.23\,\mathrm{GHz}$ is sensitive to Ω_{NMR}. $T_{2,\mathrm{e}} = 10\,\mathrm{ns}$ and $T_{2,\mathrm{n}} = 500\,\mathrm{ns}$. Other calculation parameters identical to Figure 5.5.

spin upwards. In contrast, when spin pumping is strong, we expect to always have a negative signal at positive bias since the electron spin is pumped towards η and ESR driving acts to decrease the magnitude of electron polarization.

We now apply an additional frequency to drive the transition $|2\rangle \leftrightarrow |3\rangle$. This second rate impedes the Overhauser effect: now only the populations of the ESR-driven pair are affected. This occurs as any relaxation of $|4\rangle$ towards $|2\rangle$ via flip-flop scattering is immediately short-circuited by the much faster NMR rate back into $|3\rangle$. Consequently, $|3\rangle$ looses less of its population to the undriven states and the electron spin retains less of its thermal polarization compared to single frequency ESR. In the spectrum, this manifests as a small increase in the amplitude of the first hyperfine peak. Crucially, this effect does not rely on level hybridization and should persist up to high magnetic fields. In fact, it should amplify with increasing fields as flip-flop scattering becomes weaker.

In a first approximation, the measured change in magnetoconductance ΔG_{DR} in our double resonance experiment will just be the sum of single-tone driving. To isolate the smaller contribution due to the effect just described we extract the signal of interest as

$$\text{CW-ENDOR} = \frac{1}{G_{\mathrm{TS}}} \left(\Delta G_{\mathrm{DR}} - (\Delta G_{\mathrm{ESR}} + \Delta G_{\mathrm{NMR}})\right) \tag{5.8}$$

Where large values signify that NMR driving increases the magnetoconductance signal of an ESR transition. Experimentally, this signal can be obtained by subtracting the conventional single-frequency ESR-STM signal at f_{e} from a measurement in which f_{n} is swept in unmodulated continuous-wave mode. If a direct NMR signal is present, it also needs to be subtracted, with f_{e} off-resonance.

Sweeping both f_{e} and f_{n} yields 2D CW-ENDOR patterns as shown in Figure 5.7. In the limit of small tip-sample conductance, the states are populated thermally via the spin-averaging substrate-substrate scattering process. The electronic polarization is small, and the nucleus is essentially unpolarized. In this case, the pattern exhibits only three pronounced peaks. Each corresponds to NMR driving on one of the states being driven by ESR, as in Figure 5.6. Note that at a field as low as 50 mT the extracted signal strength of nuclear transitions already far exceeds that obtained by readout via hyperfine hybridization (Figure 5.5.)

When the tip is moved closer, spin-polarized scattering polarizes both electron and nucleus via the avalanche effect (Figure 5.4). Due to the dramatically enhanced population differences between the spin levels, we can now observe signal for all combinations of ESR and NMR transitions. Since the electron spin has been inverted by spin pumping, so has the polarity of the CW-ENDOR peaks. This allows the read-out of the nuclear state using any of the six levels. Remarkably, since strong magnetic fields can now be used, even the nuclear Zeeman effect can in principle be observed.

The applicability on the proposed implementation of CW-ENDOR relies on our assumption that nuclear driving be sufficiently strong, even at larger fields. Whether this is the case will depend on whether the dominant driving mechanism depends on hyperfine-induced

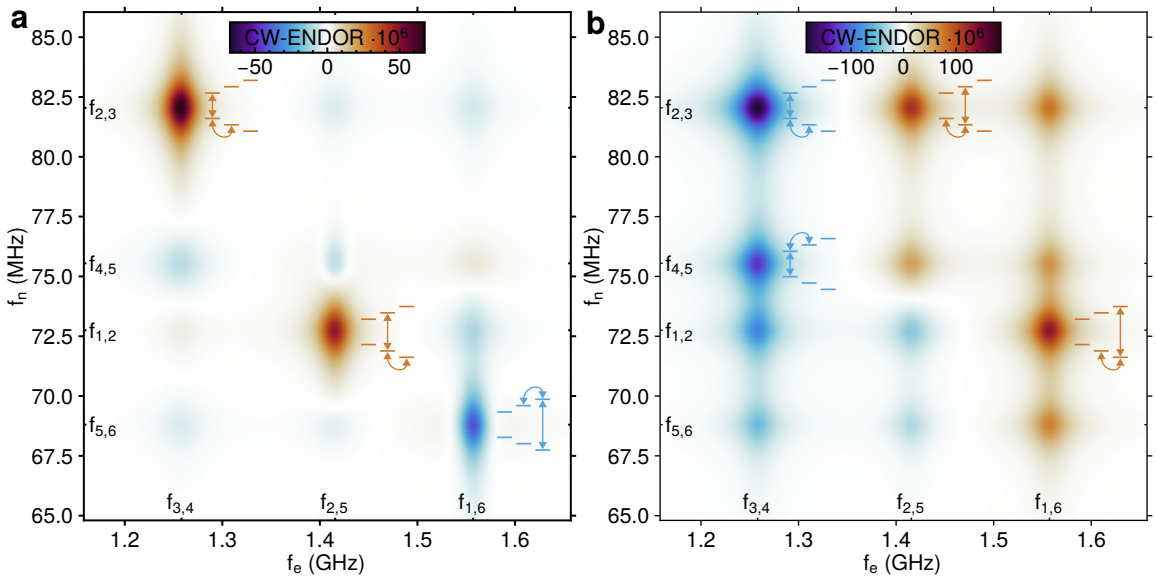

Figure 5.7: 2D CW-ENDOR diagram at $B = 50\,\mathrm{mT}$ and $U = 17\,\mathrm{mV}$ at different tip-sample separations. In **(a)**, $G_{\mathrm{TS}} = 10\,\mathrm{pS}$. In **(b)**, $G_{\mathrm{TS}} = 5\,\mathrm{nS}$. Sketches show the driving schemes for dominant peaks. In both panels, $\Omega_{\mathrm{NMR}} = 30\,\mathrm{MHz}$ and $\Omega_{\mathrm{ESR}} = 100\,\mathrm{MHz}$. We have set $T_{2,\mathrm{e}} = 10\,\mathrm{ns}$ and $T_{2,\mathrm{n}} = 200\,\mathrm{ns}$ for clarity. Other calculation parameters identical to Figure 5.6.

hybridization or not. The transduction of the RF out-of-surface electric field emanating from the tip to a transverse RF magnetic field experienced by the nucleus is essential. Possibly, it is caused by a Stark effect on the electronic orbital. In this picture, the electron cloud distorts easily due to the extreme proximity of the tip. The nucleus, being much heavier, could then be assumed to be stationary within the Born-Oppenheimer approximation. This has two consequences. For one, the weight of the electronic wave function at the nucleus is modulated periodically, which also modulates A which is mostly made up by the Fermi contact interaction. This can lead to a torque onto the nuclear spin.[301] It scales with the strength of the hyperfine interaction and therefore will vanish at large fields together with flip-flop scattering. The second effect occurs only for high-spin nuclei in low-symmetry environments, such as a crystal surface. The quadrupole splitting is proportional to the electric field gradient at the nucleus, which is also modulated by the RF displacement of the electronic orbital. This effect is field-independent, but also quite weak: typical quadrupole interactions are in the range of only a few MHz.

We will now apply the developed formalism for CW-ENDOR to a system where both NMR and ESR using STM have been demonstrated previously. Titanium is known to act as a $S = 1/2$ on MgO/Ag(100). Its stable isotope ^{47}Ti possesses a nuclear spin $I = 5/2$. On the oxygen adsorption site, the electronic wavefunction and thereby all relevant tensors in the spin Hamiltonian have uniaxial symmetry. Veldman *et al.*[116] were able to precisely quantify the principal values of the hyperfine and quadrupole tensors of $^{47}\mathrm{Ti_O}$ with $A = (10, 10, 130)\,\mathrm{MHz}$ and $Q = (1.5, 1.5, -3)\,\mathrm{MHz}$. The g-tensor has also been shown to be anisotropic and particularly small longitudinally: $g = (-1.67, -1.67, -0.61)$.[304] We will

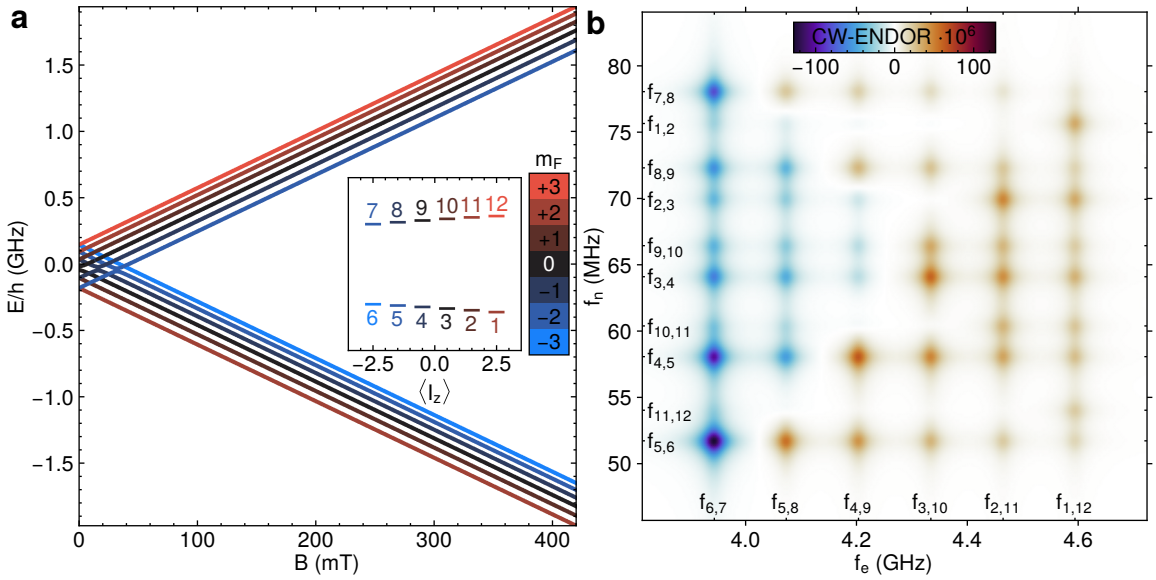

Figure 5.8: Zeeman diagram of $^{47}Ti_O$ (**a**) and its $B = 500\,\mathrm{mT}$ 2D CW-ENDOR pattern (**b**). Calculation parameters identical to Figure 5.7b.

also assume $g_n = -0.31$.[305] The large nuclear spin imbues this isotope with twelve Zeeman-like states as in Equation (5.4) for a purely out-of-surface field above the highest level anti-crossing at 40 mT. All NMR transition differ by each other by a few MHz at these fields. The Zeeman diagram is shown in Figure 5.8a.

Under sufficiently spin-pumped conditions, the system presents itself with a rich 2D CW-ENDOR pattern consisting of a manifold of 50 out of 60 possible individual peaks (Figure 5.8b). As before, the avalanche effect at positive spin polarization and bias funnels most population into state $|12\rangle$ and thereby also polarizes the nucleus. Due to the large number of nuclear spin levels, an asymmetry between NMR driving of states with opposite sign of m_I is now apparent. Addressing states with $m_I = +5/2$ has little effect: probing the four central ESR frequencies, NMR on $|1\rangle \leftrightarrow |2\rangle$ and $|11\rangle \leftrightarrow |12\rangle$ gives no signal, while $|7\rangle \leftrightarrow |8\rangle$ and $|5\rangle \leftrightarrow |6\rangle$ does. Likewise, the largest ESR frequency gives the smallest signals. The population avalanche towards $|12\rangle$ is most sensitive to the populations of the $m_I = -5/2$ states; any effects of NMR driving are thereby amplified.

Of particular interest is the evolution of the f_n-swept spectrum with magnetic field shown in Figure 5.9a. We choose to probe the lowest ESR frequency, $|6\rangle \leftrightarrow |7\rangle$. Signal of measurable strength is found at all fields, with the three dominant transitions actually increasing in amplitude as the states dehybridize. Even for the modest coherence times chosen, the nuclear Zeeman effect can be energetically resolved, indicating individual addressability of the nuclear states. Two dominant peaks are evident; they correspond to NMR driving into or out of the inital and final states of the probed ESR transition: $|5\rangle \leftrightarrow |6\rangle$ and $|7\rangle \leftrightarrow |8\rangle$. The third-largest peak occurs when driving the next-removed nuclear transition $|4\rangle \leftrightarrow |5\rangle$. Its intensity is enhanced due to the indirect nuclear spin flip from $|5\rangle$ to $|6\rangle$ via $|7\rangle$. In general,

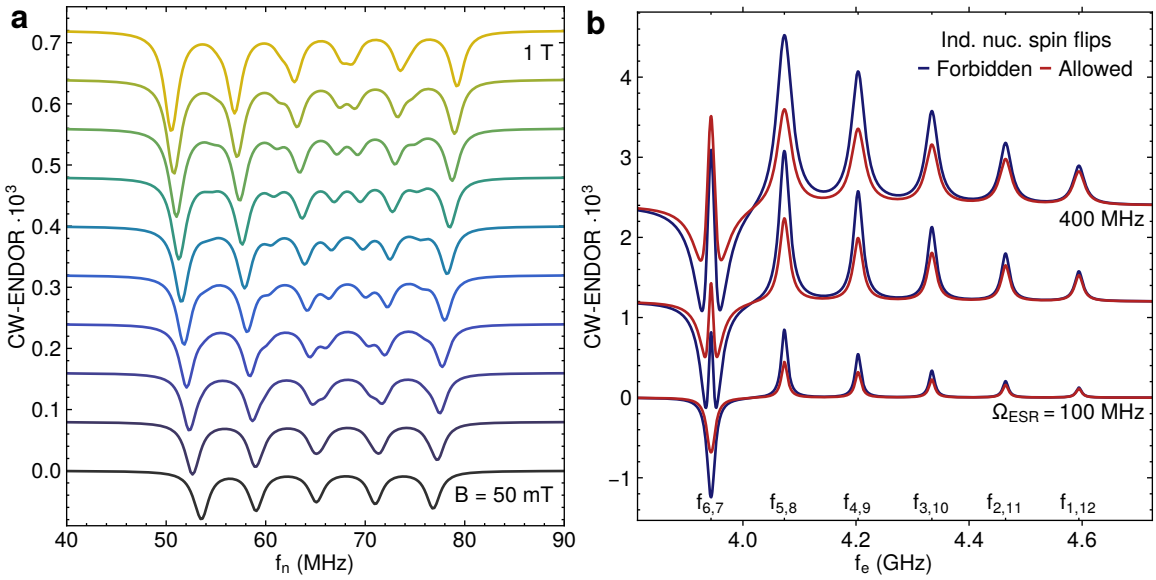

Figure 5.9: (**a**): Field dependence of the CW-ENDOR spectrum when probing the first ESR transition. In (**b**), the electronic Rabi frequency is varied. In this case, the first NMR transition is probed while the f_e is swept. In (**b**), $T_{2,e} = 30\,\text{ns}$ and $T_{2,n} = 1\,\mu\text{s}$. Other calculation parameters identical to Figure 5.8b.

inclusion of these processes gives a more equal double-resonance intensity between all pairs of states, as the saturation of a NMR pair is more strongly linked to the other populations.

Finally, we briefly address the dependence of CW-ENDOR on driving strengths in this system. At small tip-sample conductance, the peak heights increase monotonously with the electronic Rabi frequency Ω_{ESR}, and eventually saturate. At closer distances, the behaviour is more intricate as shown in Figure 5.9b. For very large but experimentally achievable electronic driving approaching the regime of GHz,[118] the magnetic resonance rate exceeds those of direct electronic spin-flips responsible for the avalanche effect. The electron polarization is driven back towards its thermal value; consequently, the CW-ENDOR signal inverts as we saw already in Figure 5.7. This is the case only for pairs of frequencies that act upon the same state and occurs sooner when indirect nuclear spin-flips are included. The latter is because this scattering mechanism opposes the principal spin-pumping effect and helps to overcome it. Within realistic ranges of coherence times and driving rates, no such inversion exists with the nuclear driving rate at the magnetic fields considered here.

Summary of Chapter 5

In this last chapter, we covered the implementation of quantum coherent measurements in the LT-STM, both experimentally and theoretically. By detecting the electron spin resonance of a single titanium atom supported by MgO, we validated the setup developed in

this thesis as a state-of-the-art ESR-STM with negligible instrumental broadening. As a result, we were able to achieve excellent energy resolution and signal sensitivity, which will allow measurements of weak interactions such as those between electronic and nuclear spins in single molecules.

Motivated by this possibility, we investigated how the double-resonance technique can be applied to ESR-STM in hyperfine-coupled systems. We rigorously modelled the effect of spin-polarized tunnelling, simultaneous ESR and NMR, and magnetoresistive readout. By including higher-order processes, we described a new T_1 mechanism for the nuclear spin by which inelastic scattering can limit the sensitivity to single-frequency NMR driving. In the simulated electron-nuclear double resonance experiment, we found that the signal obtained from nuclear transitions exceeds that from pure NMR. Spin pumping by tunnelling electrons, in this case, is beneficial: its action allows for a magnetoconductive response at almost all combinations of electronic and nuclear resonance frequencies, and thereby a full characterization of the hyperfine manifold. Finally, we generalized the results by considering an experimentally investigated system with a large nuclear spin and an additional quadrupolar coupling: individual ^{47}Ti atoms on MgO/Ag(100).

Conclusions and outlook

In this thesis, we investigated the electronic spin of single adsorbed molecules by low-temperature scanning tunnelling spectroscopy. Interactions with the underlying surface are generally detrimental, but we identified mitigation strategies based on functional layers and molecular engineering. For instance, charge transfer can be compensated on several substrates, provided the work functions lies between electron affinity and ionization potential. This approach was realized in a specific chiral graphene nanoribbon geometry directly synthesized on thin layers of the intermetallic $GdAu_2$. The neutral charge state manifested in the emergence of two Kondo-screened local magnetic moments hosted by symmetry-protected topological zero modes, which are quenched for another edge geometry.[197] By manipulation across the surface, we were additionally able to reversibly pair single π-radical electrons, which Kelvin probe force microscopy revealed is caused by the electrostatically inhomogeneous moiré superstructure of $GdAu_2$. This gave inversion-symmetry-broken singly anionic chGNRs, with a doublet spin, and a net magnetic moment. Given the high susceptibility of zero-energy modes to electron transfer, other rare earth alloys with slightly modified work functions[195] may additionally stabilize the charge states $+1$ and -2. The ability to switch individual π-radicals "on" and "off" should enable the selective study of mutual interactions in high-spin nanographene systems.[306,307]

To mitigate magnetic scattering with conduction electrons, we studied single molecular spins on ultrathin layers of the insulator MgO, which results in a decoupling from the underlying metal. The reduced hybridization allowed us to probe molecular tunnelling with extraordinary resolution. The Kondo effect was found to be significantly weakened, enabling large magnetic relaxation times. Absence of metallic screening also enhanced the effect of intramolecular Coulomb repulsion, resulting in the opening of a correlation gap. Due to the small work function of MgO/Ag(100), a large anionic integer electron transfer into adsorbed molecules can take place, which however competes with electron-electron correlations. We found that in the case of chiral graphene nanoribbons, the equilibrium charge state is predictably determined by length, and alternates between an even-numbered closed-shell configuration to an odd-numbered open-shell state. On the other hand, we were able to show that in the much smaller tetrapyrrole H_2Pc, large intramolecular correlation due to high orbital localization can prevent integer charge transfer entirely.

We also explored how molecule-surface interactions can be minimized in specialized chemical structures. The phenylated macrocycles FeTPP and FeTPP-Cl were found to retain their

gas-phase spin by non-planar adsorption on the electropositive surface Ag(100), and even on additional MgO layers. The self-decoupling effect was also shown to be effective in isolated vanadocene molecules, which by virtue of confined orbitals did not feature observable Kondo screening despite direct contact to a metallic substrate. We anticipate that combining three-dimensional coordination with decoupling layers could give superior quantum coherence over candidates with a mostly flat adsorption configuration.[14]

We also explored the concept of exchange bias at the single-molecule level. We showed that due to the in-plane ferromagnetism of $GdAu_2$, the two topological end states in neutral chiral graphene nanoribbons are simultaneously exchange-coupled both to one another, but also to the surface. The latter was found to vary locally, and to be large enough to overcome both the Kondo effect and the intramolecular exchange interaction. This allows for a stable triplet state, protected energetically from conduction electron scattering. We then sensed the exchange field of $GdAu_2$ with high spatial resolution by attaching a single nickelocene molecule to the STM tip and forming quantum point contacts with individual Gd^{3+} sites in the surface lattice. Magnetic excitations of the Kondo-screened state allowed us to infer the magnitude and atomic variation of the exchange bias as experienced by adsorbed spins such as nanographene π-radicals. Combining electronic decoupling with an exchange bias is a promising intersection, as one could obtain a coherent two-level molecular spin qubit with a built-in splitting; ferromagnetic insulators offer this joint functionality.[218]

The experiments in this thesis yielded several molecular spin qubit candidates, that show sufficiently decoupled spin two-level systems when adsorbed on surfaces. A $S = 1/2$ was found in singly anionic phthalocyanine H_2Pc^- and in several chiral graphene nanoribbons supported by MgO. In the former case, a spin-pumping experiment in an external magnetic field provided evidence of an enhanced T_1 time. The self-decoupling $S = 3/2$ molecules FeTPP-Cl and vanadocene also show potential as spin qubits due to their easy-plane anisotropy. In particular, tip-adsorbed VCp_2 could enable highly sensitive magnetometry by probing the $m_s = \pm 1/2$ transition with magnetic resonance.[250]

To assess the decoherence time T_2 of single-molecule spin qubits, we successfully implemented a ESR-STM setup operating at 1.3 K, frequencies up to 40 GHz and out-of-plane magnetic fields up to 3 T. In a benchmark experiment, we detected magnetic resonance of a single titanium atom on MgO with negligible instrumental broadening. The neV energy resolution obtained will enable quantifying fine magnetic structure, such as the coupling to ^{13}C nuclei in nanographene.[308] Motivated by this possibility, we modelled an STM implementation of continuous wave electron-nuclear double resonance. The results show that the two-frequency scheme gives appreciable changes in the magnetoconductance when probing nuclear transitions, which we found can even exceed that of single-frequency driving. Spin-polarized inelastic tunnelling initializes the nuclear spin, allowing greater population differences between levels than those attainable by external fields and low temperatures. This leads to a double resonance signal at almost all frequency pairs, such that the full hyperfine manifold can be quantified. Experimentally, such a signal has so far not been resolved[299] due to a broadening of NMR transitions at large ESR drive amplitudes. However, we can anticipate its observation in further studies on highly decoupled molecular systems with

nuclear moments such as ^{57}FeTPP-Cl/MgO, possibly also at lower temperatures,[14] where smaller Rabi frequencies are sufficient to drive the electron spin. A double-resonance experiment also requires coherent nuclear driving, which we proposed may be mediated by the quadrupolar interaction. Transduction of RF electric to magnetic fields could be boosted by careful selection of isotopes with large quadrupole moments, such as lanthanides.[305] By leveraging low-symmetry adatom adsorption sites on decoupling layers, or tailor-made ligands in molecular systems, the spin-carrying orbitals could be distorted[9,309] to maximize the effect.

Appendix

A.3 Radiation from stripped coaxial cable

A stripped coaxial cable was employed in Section 2.3 as a termination to the newly installed feedline, which is intended to transmit RF signals to the STM tip. We will explore the nature of radiation from such a structure, its dependence on geometry, and the mechanism of coupling.

The closest established antenna architecture is the coax-fed monopole antenna. An (ideally infinite) ground plane is penetrated by the inner conductor of a coaxial cable, which extends well above it and acts, together with its image charge, as the resonating dipole element.[180] We parametrically simulated such structures using the finite-element electromagnetic solver implemented in `Comsol 5.4` assuming non-resistive surfaces. The axisymmetric arrangement allows definition in 2D, as shown in Figure A.10. The coax dimensions are those of the actual 50 Ω cable used in the experiment. It is excited across the PTFE dielectric at its shorted end. The whole arrangement is contained in a vacuum sphere surrounded by a non-reflective boundary which suppresses cavity modes and allows calculation of the far-field amplitudes. The conical opening angle of the exposed inner conductor is not relevant here and set to 1°.

The RF response of the coaxial monopole antenna, quantified by the reflection amplitude

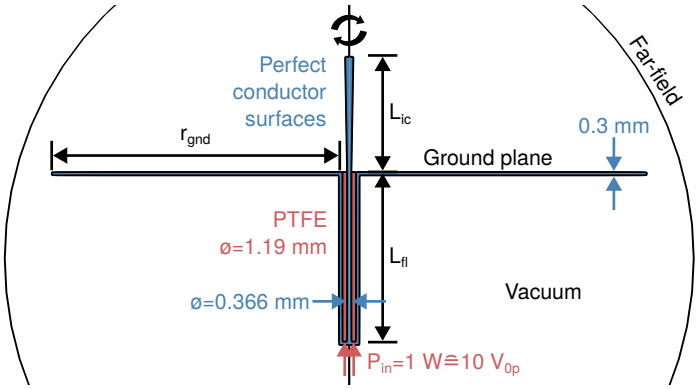

Figure A.10: Definition of the simulation domain. A shorted coaxial stub (L_{fl}) is excited across its dielectric. At the other end, the insulator is truncated, the outer conductor forms a disk (r_{gnd}), and the inner conductor a monopole of length L_{ic}. No electrical resistance is included. The structure is encased in a vacuum sphere with non-reflective outer boundaries.

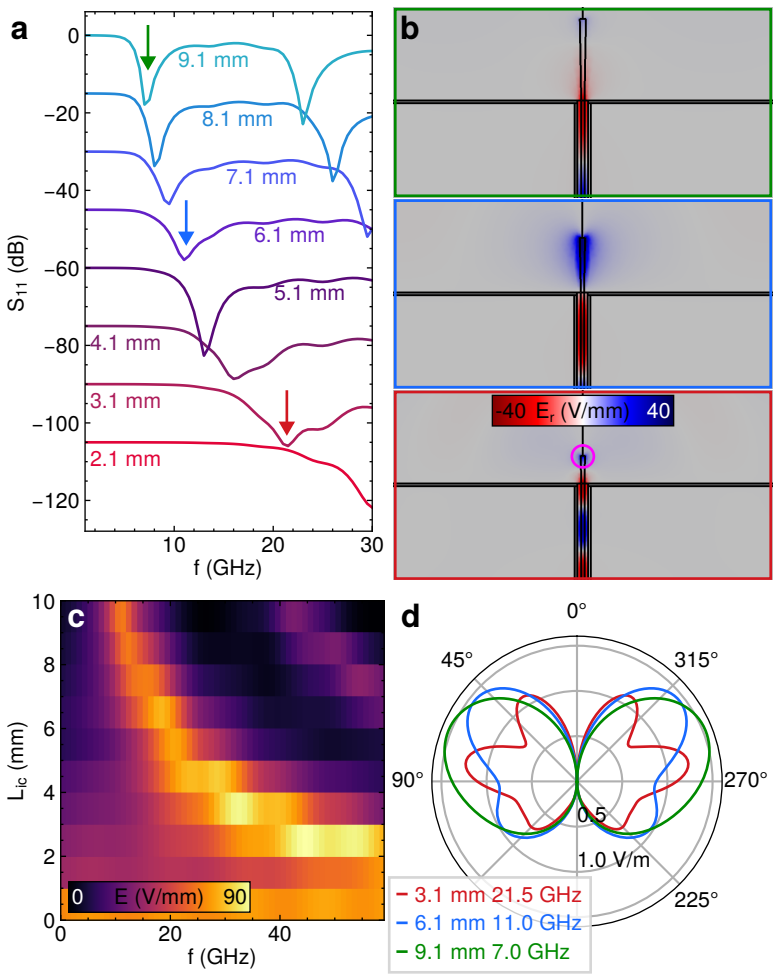

Figure A.11: Characterization of the coaxial monopole antenna resonance, with a large ground plane. **(a)** The reflection S_{11} shows two resonances which shift with L_{ic}. **(b)** Radial electric field component for the strongest mode at L_{ic}=9.1, 6.1 and 3.1 mm marked on the left. **(c)** Total electric field at the tip if the extended inner conductor as function of f and L_{ic}. **(d)** Far-field radiation patterns of the three resonances shown above. Note the developed side lobes for L_{ic}=3.1 mm.

S_{11} back towards the excitation port, is displayed in Figure A.11a. Radiation occurs in a series of discrete resonances (here two), that blueshift as the radiative length L_{ic} is reduced. Ideal monopole antennas support resonances with a voltage nodal plane at the bottom of the element and more within it, whose frequency is given by $L_{ic} \approx \lambda/4 + n\lambda/2, n \in \mathbf{Z}$. Due to the finite geometry used here, the position of nodal planes is slightly modified.

In Figure A.11b, the $\lambda/4$ modes are shown for different values of L_{ic}. The far-field radiation patterns in Figure A.11d reveal a development of side lobes for small L_{ic}; this is characteristic for a resonant element radius comparable to its length. The quantity of interest is the electric field magnitude at the tip of the exposed inner conductor, which establishes the potential capacitively coupling to the STM tip in the near field. As seen in in Figure A.11c, it is largest for the fundamental mode.

We will now investigate the case of a finite ground plane radius r_{gnd}. As shown in Figure A.12a, this modifies the radiation characteristic: the $\lambda/4$ antenna resonance is shifted to higher frequencies, and eventually dies out when the ground plane has vanished completely. This behaviour is expected, as the image charge can no longer be produced. Meanwhile, a second mode becomes apparent whose position and amplitude are largely independent

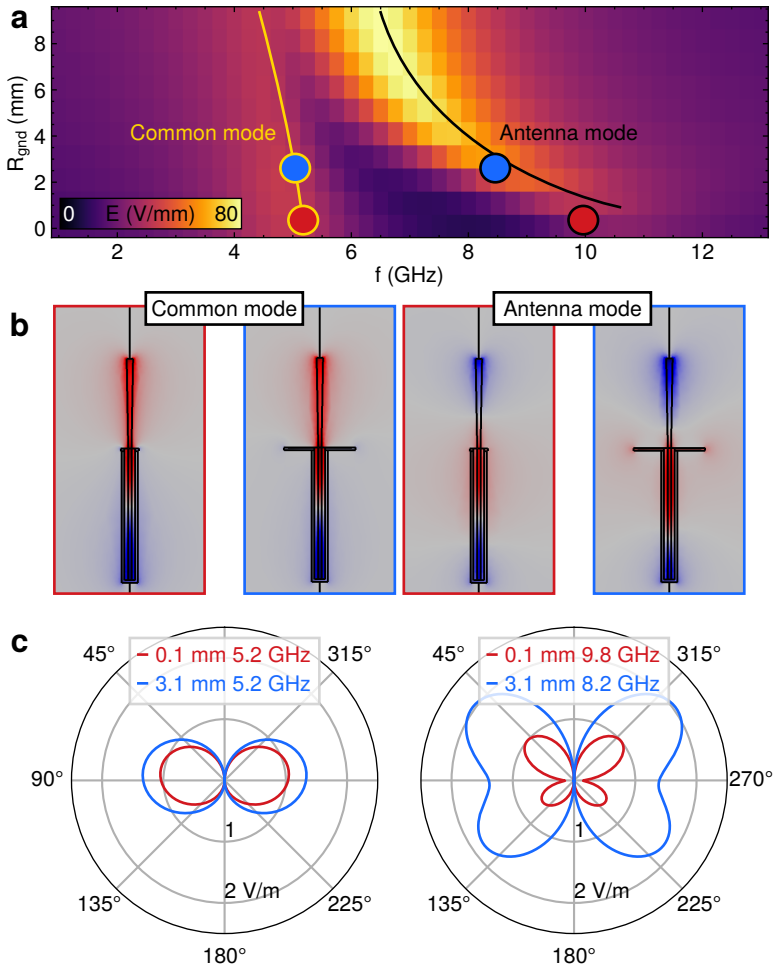

Figure A.12: Response to ground plane radii r_{gnd}<L_{ic}. **(a)** Electric field magnitude at the tip of the extended inner connector as a function of f and r_{gnd}. The antenna mode is shifted up and disappears, while a second resonance, the common mode, persists. **(b)** Antenna and common mode for small and vanishing ground planes. Significant field strengths are present along the outer conductor. **(c)** Far-field radiation patterns of either resonance. The coaxial feedline acts as a dipole with a typical figure-eight common-mode emission.

of r_{gnd}. We refer to it as the common mode; currents rejected from the modified antenna mode travelling downwards along the perimeter of the outer conductor radiate into free space, see Figure A.12b. Its radiation pattern is figure- eight-shaped, as that of a dipole; conversely, the residual antenna mode radiation is highly anisotropic. The far-field radiated power $P \propto E^2$ from the antenna mode is much smaller than that of the common mode. Its non-zero amplitude derives purely from the finite width of the outer conductor, which acts as a miniature ground plane.

Clearly, our stripped coaxial cable structure does not act as an antenna in the intended way, since the resonant element is formed by the feedline itself. The common mode is best characterized by letting the feedline length vary, as shown in Figure A.13b. The series of resonances, each with a corresponding numbers of nodal planes on the outer surface of the shield, disperse with L_{fl}, proving the feedline as the primary emitter. Even for a vanishing ground plane, the tip of the exposed inner conductor still sees a sizeable electric field, but whose amplitude decays quickly with its extension (Figure A.13c). On the other hand, the resonance frequencies show only a minor dependence on L_{ic}, as the inner conductor is not the emitting element.

Practically, it is therefore preferable to keep the exposed inner conductor short for the max-

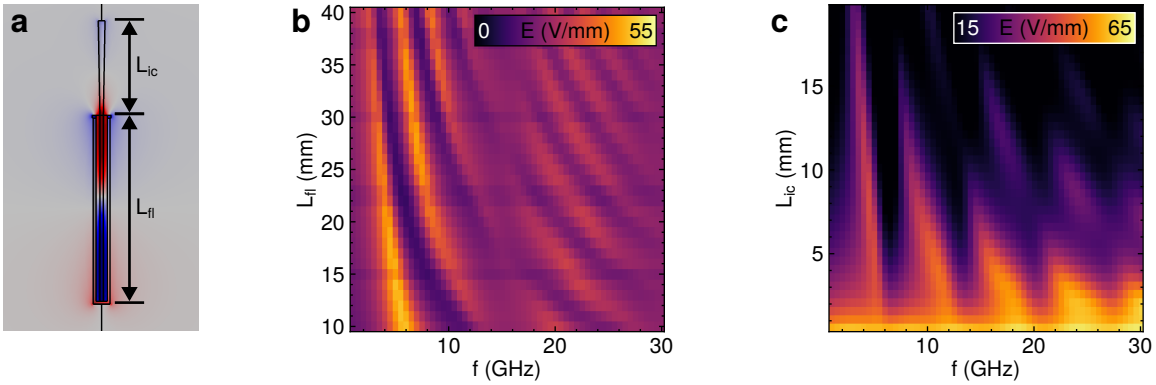

Figure A.13: Common-mode resonances for r_{gnd}=0 as a function of feedline length L_{fl} and inner conductor extension L_{ic}.

imum amplitude at its tip; this will not come at the penalty of high-lying, widely spaced resonances, as one may expect. This rationale was followed in determining the dimensions of the antenna termination in Section 2.3. Since the cable's polymer jacket was removed, the metallic shield contacts the grounded body of the microscope unit at several positions. This makes up a complex ground plane, such that the radiative length of the common mode is only part of the entire feedline. The resonant coupling to the STM tip is then best interpreted in terms of a coaxially fed 3D cavity mode, whose electric field is picked up by the tip-surface gap.[128] In our setup, the reflective cavity boundaries are formed by the tip assembly and sample surface, as well as the microscope body enclosed by the cryogenic heat shield.

A.4 Survey of MgO epitaxy on Ag(100)

In the context of this thesis, the epitaxy of MgO on Ag(100), introduced in Section 2.1, had to be finely controlled in order to produce sub-monolayer coverages of defect-free insulating patches as shown in the main text. We discuss here the formation of MgO under non-optimal conditions, and thereby attempt to draw conclusions about the growth mechanism. The key variables are substrate temperature (250 to 420 °C) and the Mg sublimation rate, the latter controlled by the Knudsen cell heating power. The former is the most influential parameter: changes of 10 °C can lead to completely different growth modes. Since accurate temperature measurements in UHV are notoriously challenging, we report here the filament current used for heating the Ag(100) single crystal. The Mg rate determined using a quartz microbalance ranges from 0.14 to 2.1 Å/min. We find high-quality epitaxy can be achieved for any choice of sublimation rate by making adjustments to the Ag temperature. The oxygen pressure, as will be shown now, is found to play only a subordinate role.

Figure A.14 shows "phase diagrams" of MgO epitaxy, in which representative topographic scans are placed at coordinates representing Ag and Mg temperatures. Marker size and

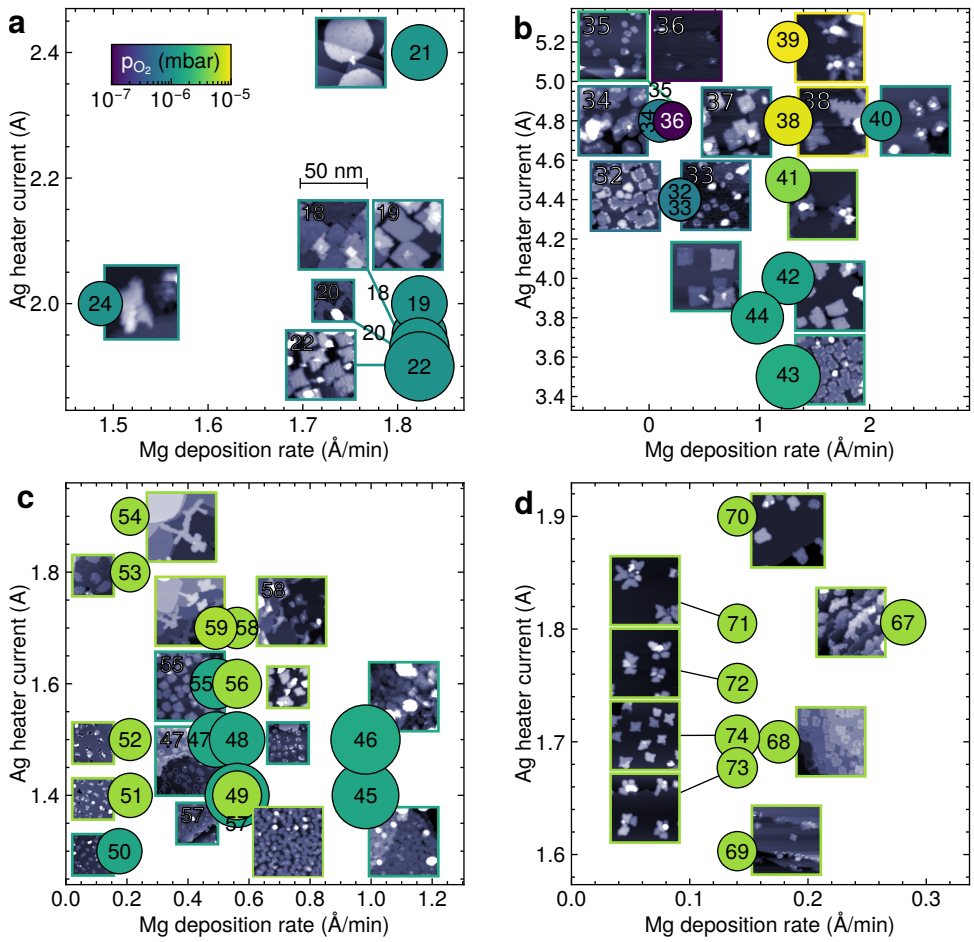

Figure A.14: Morphology phase diagram of MgO epitaxy on Ag{100}, showing growth conditions and representative STM scans taken at a sample bias above 3 V. Marker size is proportional to the apparent growth rate. Marker color denotes oxygen pressure. Note that the experimental parameters are not to be compared between panels.

colour indicate growth rate, as determined by STM, and oxygen pressures, respectively. All four datasets have been acquired using differing evaporation geometries, so only qualitative comparison is possible between panels. The desired growth mode is that of few but large and flat islands with little point defects, such as in samples 18, 19, 21 and 44. Under different conditions, the morphology can change drastically. For instance, excessive Ag heating at low Mg rates leads to dendritic edge shapes (cf. samples 42 and 38, 55 and 54, or 74 and 71). Insufficient Ag temperature instead gives finely dispersed round nuclei (samples 59 and 57) at any Mg rate. This morphology can also persist at high temperatures if the Mg rate is small (samples 35 and 36). Large circular patches can form at large Ag temperatures and high Mg rates (sample 21). Three-dimensional growth occurs at high Ag temperatures (samples 19, 24, 40, 58) and manifests as a central protrusion. Generally, largest growth rates are achieved at the smallest Ag temperatures. The oxygen pressure was not found to have a large effect across the orders of magnitude (36 vs 35, 38 vs 41).

Considering the high sensitivity to substrate temperature, we propose that the reaction of

Mg and O to form MgO crystals occurs on the Ag(100) surface as opposed to in the gas phase. The substrate temperature then controls the sticking coefficient of Mg and O_2 at a given rate/pressure, which gives their equilibrium coverage. This is corroborated by the observation of increased growth rates at lower temperatures. However, since adsorption of Mg and O_2 will depend differently on temperature, the overall stoichiometry is also affected. Furthermore, heating modifies the adatom diffusion constants which are essential to crystallization. Sensitivity to substrate temperature also hints at a thermally activated dissociation of O_2 into atomic O on Ag(100)[310] which could limit the reaction rate as opposed to diffusion. Overall, both the stoichiometry and epitaxy kinetics will be dictated by respective Arrhenius laws in the Ag temperature. At low Mg rates and small O pressures, Mg and O adatoms are found in equal proportion and diffuse across the surface before finding a vacancy at the edge or atop a MgO nucleus.[137] This heterogeneous nucleation enables the growth of few, large islands without defects. At large Mg rates and small O pressures, or vice versa, the surface is instead saturated with one species and reactions occurs rapidly upon adsorption of the other, which manifests as disperse homogeneous nucleation. In this case, only small nuclei are found.

While slow stoichiometric growth is preferable for island size and sparsity, as adatoms can diffuse lengthily and attach to highly coordinated edge vacancies, it is also susceptible to contamination. We find the boundaries of such patches often passivated by the background pressure of the UHV chamber (cf. samples 32, 53), which inhibits further growth and leads to a large number of smaller islands. The best results are obtained at rather large Mg sublimation rates. The two-dimensional shape of the islands is also influenced by the growth kinetics. Ideally, the outer boundary should lie along the high-symmetry directions of the MgO lattice, forming perfect rectangles.[141,144] We find that at a given oxygen pressure, excessive Mg sublimation rates lead to convex boundaries (71 vs 67), and Mg scarcity to concave edges (68 vs 74). This mechanism has been proposed to be an electrostatic preference for the formation of edges with polar character under non-stoichiometric conditions.[155] These effects are more pronounced at higher temperatures, leading to circles (21) and fully dendritic shapes (54), respectively.

A.5 On the asymmetric Hubbard dimer

Section 3.1 makes use of the Hubbard dimer in the grand canonical ensemble to extract the (effective) magnetic field required for singlet-doublet-triplet transitions in chiral graphene nanoribbons. This appendix describes the calculation in more detail. A site-symmetric version was studied by Cheng *et al.*[209]. To solve the fully asymmetric Hamiltonian (Equation (3.1)) we choose the basis $|\varphi_k\rangle$ spanning zero, one, two, three and four electrons occupying either site i, j (L and R) with respective spins $\uparrow$ and $\downarrow$. There are $\sum_0^4 \binom{4}{N} = 16$ states,

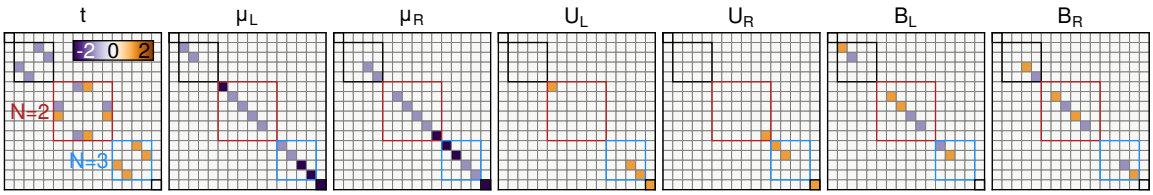

Figure A.15: Hamiltonian matrix elements of the asymmetric Hubbard dimer. Entries for each variable are represented by shaded squares, with values in $\{-2,-1,0,+1,+2\}$. The blocks $N=2$ and $N=3$ are relevant to this work.

which we denote as $|n_{\mathrm{L}\uparrow} n_{\mathrm{L}\downarrow} n_{\mathrm{R}\uparrow} n_{\mathrm{R}\downarrow}\rangle$:[311]

$$
\begin{aligned}
|0000\rangle &= |0\rangle & |0110\rangle &= \hat{c}^\dagger_{\mathrm{L}\downarrow}\hat{c}^\dagger_{\mathrm{R}\uparrow}|0\rangle \\
|1000\rangle &= \hat{c}^\dagger_{\mathrm{L}\uparrow}|0\rangle & |0101\rangle &= \hat{c}^\dagger_{\mathrm{L}\downarrow}\hat{c}^\dagger_{\mathrm{R}\downarrow}|0\rangle \\
|0100\rangle &= \hat{c}^\dagger_{\mathrm{L}\downarrow}|0\rangle & |0011\rangle &= \hat{c}^\dagger_{\mathrm{R}\uparrow}\hat{c}^\dagger_{\mathrm{R}\downarrow}|0\rangle \\
|0010\rangle &= \hat{c}^\dagger_{\mathrm{R}\uparrow}|0\rangle & |0111\rangle &= \hat{c}^\dagger_{\mathrm{L}\downarrow}\hat{c}^\dagger_{\mathrm{R}\uparrow}\hat{c}^\dagger_{\mathrm{R}\downarrow}|0\rangle \\
|0001\rangle &= \hat{c}^\dagger_{\mathrm{R}\downarrow}|0\rangle & |1011\rangle &= \hat{c}^\dagger_{\mathrm{L}\uparrow}\hat{c}^\dagger_{\mathrm{R}\uparrow}\hat{c}^\dagger_{\mathrm{R}\downarrow}|0\rangle \\
|1100\rangle &= \hat{c}^\dagger_{\mathrm{L}\uparrow}\hat{c}^\dagger_{\mathrm{L}\downarrow}|0\rangle & |1101\rangle &= \hat{c}^\dagger_{\mathrm{L}\uparrow}\hat{c}^\dagger_{\mathrm{L}\downarrow}\hat{c}^\dagger_{\mathrm{R}\downarrow}|0\rangle \\
|1010\rangle &= \hat{c}^\dagger_{\mathrm{L}\uparrow}\hat{c}^\dagger_{\mathrm{R}\uparrow}|0\rangle & |1110\rangle &= \hat{c}^\dagger_{\mathrm{L}\uparrow}\hat{c}^\dagger_{\mathrm{L}\downarrow}\hat{c}^\dagger_{\mathrm{R}\uparrow}|0\rangle \\
|1001\rangle &= \hat{c}^\dagger_{\mathrm{L}\uparrow}\hat{c}^\dagger_{\mathrm{R}\downarrow}|0\rangle & |1111\rangle &= \hat{c}^\dagger_{\mathrm{L}\uparrow}\hat{c}^\dagger_{\mathrm{L}\downarrow}\hat{c}^\dagger_{\mathrm{R}\uparrow}\hat{c}^\dagger_{\mathrm{L}\downarrow}|0\rangle
\end{aligned}
\tag{A.9}
$$

The Hamiltonian matrix elements are obtained by letting $\mathcal{H}$ act on the basis states.[312] Their values are shown in Figure A.15. We limit the following discussion to blocks $N=2$ and $N=3$, which corresponds to half-filling and a singly anionic charge state, respectively.

Exact diagonalization then gives $6+4=10$ eigenstates in total, which we label as $|N, m_s\rangle$. The system's ground states relevant to the experiment are constituted by the low-energy states at $N=2$, which are the singlet $|2,0\rangle$ and triplets $|2,-1\rangle$, $|2,+1\rangle$, and those at $N=3$, namely the doublets $|3,-1/2\rangle$ and $|3,+1/2\rangle$. We will first discuss the simplest choice of parameters: symmetric repulsion $U_{\mathrm{L}} = U_{\mathrm{R}} = U_{\mathrm{sym}}$, symmetric field $B_{\mathrm{L}} = B_{\mathrm{R}} = B_{\mathrm{sym}}$ and half-filling $\mu_{\mathrm{L}} = \mu_{\mathrm{R}} = U_{\mathrm{sym}}/2$. Section A.5 plots the eigenenergies as a function of U_{sym}/t in this case. The non-singlet states experience a Zeeman effect due to small B_{sym}. Clearly, for this choice of fields and chemical potentials, the ground state is $|2,0\rangle$, as expected. Its composition continuously evolves with U_{sym}/t. In the limits of weak and strong localization, respectively, it is

$$
\begin{aligned}
\lim_{U_{\mathrm{sym}}/t\to 0} |2,0\rangle &= \frac{1}{2}\left(|1100\rangle + |1001\rangle - |0110\rangle + |0011\rangle\right) \\
\lim_{U_{\mathrm{sym}}/t\to \infty} |2,0\rangle &= \frac{1}{\sqrt{2}}\left(|1001\rangle - |0110\rangle\right)
\end{aligned}
\tag{A.10}
$$

where the states $|1100\rangle$ and $|0011\rangle$ lose weight due to the energy penalty for double occu-

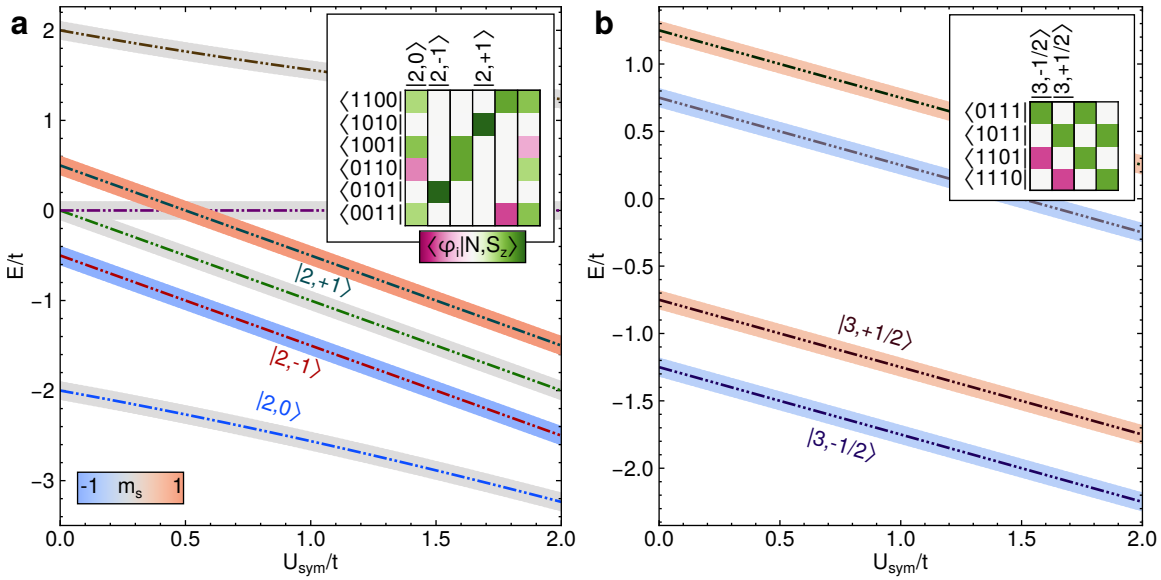

Figure A.16: Eigenstates of the Hubbard dimer in the symmetric case $U_\mathrm{L} = U_\mathrm{R} = U_\mathrm{sym}$, $B_\mathrm{L} = B_\mathrm{R} = B_\mathrm{sym} = t/4$ and half-filling $\mu_\mathrm{L} = \mu_\mathrm{R} = U_\mathrm{sym}/2$ as a function of U_sym/t, shaded by $\langle \hat{S}_\mathrm{z} \rangle$. **(a)** shows states with $N = 2$ and **(b)** for $N = 3$. Projections onto the basis $|\varphi_i\rangle$ given in Equation (A.9) are displayed in the inset for $U_\mathrm{sym} = t$.

pation. The remaining states are, for this choice of parameters, independent of U_sym/t:

$$\begin{aligned} |2,-1\rangle &= |0101\rangle \\ |2,+1\rangle &= |1010\rangle \\ |3,-1/2\rangle &= \frac{1}{\sqrt{2}}\left(|0111\rangle - |1101\rangle\right) \\ |3,+1/2\rangle &= \frac{1}{\sqrt{2}}\left(|1011\rangle - |1110\rangle\right) \end{aligned} \tag{A.11}$$

The eigenenergies for $N = 2$ are simply

$$\begin{aligned} E_{2,0} &= -\frac{U_\mathrm{sym}}{2} - \sqrt{\left(\frac{U_\mathrm{sym}}{2}\right)^2 + (2t)^2} \\ E_{2,-1} &= -U - 2B_\mathrm{sym} \\ E_{2,+1} &= -U + 2B_\mathrm{sym} \end{aligned} \tag{A.12}$$

For $B_\mathrm{sym} > 0$, the singlet-triplet transition occurs exactly at half the gap between $|2,0\rangle$ and

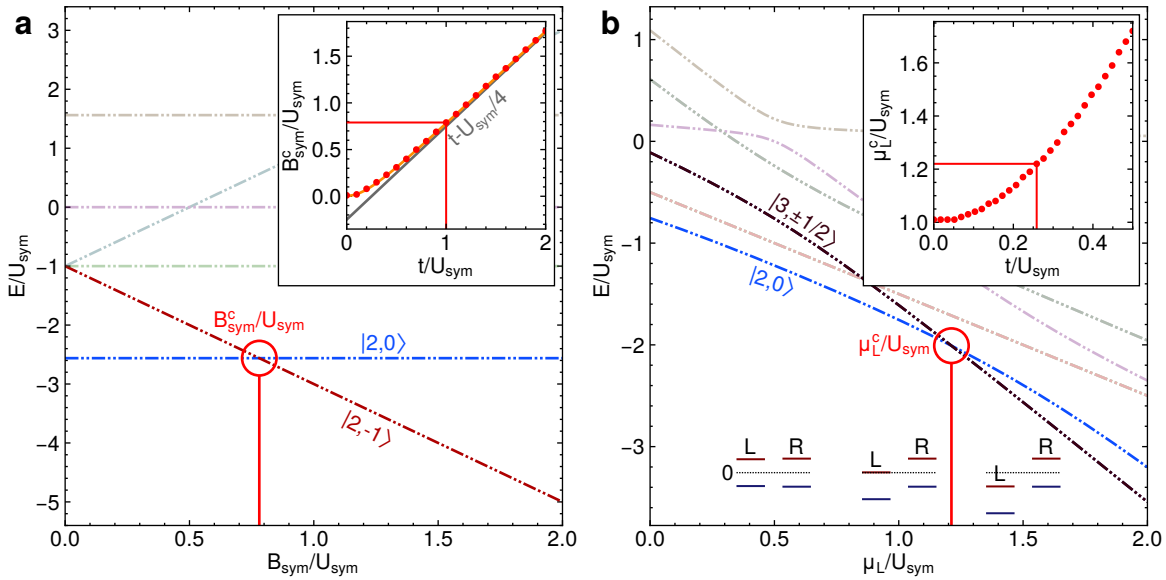

Figure A.17: Critical points of the Hubbard dimer in the chemical potential μ_{L} and field B_{sym}. **(a)** Singlet-triplet transition for $N = 2$ at $t = U_{\mathrm{sym}}$ for symmetric fields $B_{\mathrm{L}} = B_{\mathrm{R}} = B_{\mathrm{sym}}$. The inset tracks the critical field $B^{\mathrm{c}}_{\mathrm{sym}}$ for varying t/U_{sym}. **(b)** Two- and three-electron eigenenergies as a function of μ_{L} at $t/U_{\mathrm{sym}} = 0.26$ and $\mu_{\mathrm{R}} = U_{\mathrm{sym}}/2$ and $B_{\mathrm{L}} = B_{\mathrm{R}} = 0$. The charging transition takes place at $\mu^{\mathrm{c}}_{\mathrm{L}}$. The inset shows its value as a function of t/U_{sym}. Sketches depict the single-particle levels for one of the basis states in Equation (A.9).

$|2,-1\rangle$, as shown in Figure A.17a. Its values and two characteristic limits are

$$
\begin{aligned}
B^{\mathrm{c}}_{\mathrm{sym}} &= \sqrt{\left(\frac{U_{\mathrm{sym}}}{4}\right)^2 + t^2} - \frac{U_{\mathrm{sym}}}{4} \\
\lim_{U_{\mathrm{sym}}/t \to 0} B^{\mathrm{c}}_{\mathrm{sym}} &= t - \frac{U_{\mathrm{sym}}}{4} \\
\lim_{U_{\mathrm{sym}}/t \to \infty} B^{\mathrm{c}}_{\mathrm{sym}} &= \frac{2t^2}{U_{\mathrm{sym}}} z
\end{aligned}
\tag{A.13}
$$

In the latter limit, one can map the Hubbard dimer onto a Heisenberg dimer $J\hat{\sigma}_{\mathrm{L}} \cdot \hat{\sigma}_{\mathrm{R}}$ with isotropic coupling $J = -gB^{\mathrm{c}}_{\mathrm{sym}}$. For asymmetric fields $B_{\mathrm{L}} \neq B_{\mathrm{R}}$, such a picture is no longer applicable, and the Zeeman effect becomes non-linear as will be discussed below.

In Figure A.18, we fix B_{R} and let only B_{L} vary. The triplet states $|2,\pm 1\rangle$ then split linearly at only half the rate, as expected; the singlet $|2,0\rangle$ evolves in a complex manner. The critical field $B^{\mathrm{c}}_{\mathrm{L}}$ depends on the magnitude of B_{R}. Interestingly, even if B_{R} is small compared to J, sufficiently large values of B_{L} will stabilize the triplet ground state nevertheless. If however site R experiences no effective field at all, the triplet approaches the singlet eigenenergy asymptotically with B_{L}, and the ground state total spin remains zero.

We will now depart from half-filling by allowing μ_{L} to vary, but keep $\mu_{\mathrm{R}} = U_{\mathrm{sym}}/2$ and symmetric fields and repulsion. We are interested in the ground state transition from $|2,0\rangle$

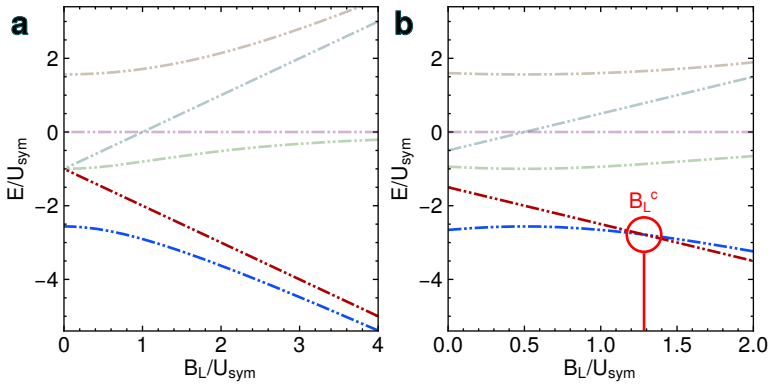

Figure A.18: Evolution of eigenenergies for asymmetric fields at $U_{\mathrm{sym}}/t = 1$. In **(a)** we set $B_{\mathrm{R}} = 0$ and in **(b)** $B_{\mathrm{R}} = U_{\mathrm{sym}}/2$. In the former case, no ground state transitions takes place.

to $|3, \pm 1/2\rangle$. The algebraic form of the eigenenergy $E_{2,0}$ becomes unwieldy in this case, but we can consider the limit of weak hybridization, where $t = 0$:

$$\begin{aligned}
\lim_{U_{\mathrm{sym}}/t \to \infty} E_{2,0} &= -\frac{U_{\mathrm{sym}}}{2} - \mu_{\mathrm{L}} \\
\lim_{U_{\mathrm{sym}}/t \to \infty} E_{2,\pm 1} &= -\frac{U_{\mathrm{sym}}}{2} - \mu_{\mathrm{L}} \pm 2B_{\mathrm{sym}} \\
\lim_{U_{\mathrm{sym}}/t \to \infty} E_{3,\pm 1/2} &= \frac{U_{\mathrm{sym}}}{2} - 2\mu_{\mathrm{L}} \pm B_{\mathrm{sym}}
\end{aligned} \tag{A.14}$$

Here, the transition occurs at the critical value

$$\mu_{\mathrm{L}}^{\mathrm{c}} = U_{\mathrm{sym}} \pm B_{\mathrm{sym}} \tag{A.15}$$

Which for $B_{\mathrm{sym}} = 0$ exactly corresponds to the case of double occupancy of site L coming at no energy cost, as shown in the inset sketches in of Figure A.17b. Numerical solution for the critical chemical potential $\mu_{\mathrm{L}}^{\mathrm{c}}$ shows it rises with t due to the increasing binding energy of the $N = 2$ singlet. We identify $\Delta\mu_{\mathrm{L}} = \mu_{\mathrm{L}} - U_{\mathrm{sym}}/2$ as the departure from half filling, akin to a local gating potential, such that $\Delta\mu_{\mathrm{L}}^{\mathrm{c}} = U_{\mathrm{sym}}/2 \pm B_{\mathrm{sym}}$ in this limit. For gating in the opposite direction, i.e. $\Delta\mu_{\mathrm{L}} < 0$, the analogous transition into the singly occupied state $|1, \pm 1/2\rangle$ takes place. This is not observed in Chapter 3, but we include it here for completeness.

The charging and field transitions mark the high-symmetry points in the ground-state phase diagram shown in Figure 3.5b with symmetric fields, repulsions and right-site half filling $\mu_{\mathrm{R}} = U_{\mathrm{sym}}$. As shown in Figure A.19a-b, increased hybridization t stabilizes the singlet state $|2, 0\rangle$ against the Zeeman effect B_{sym} and the gating potential $\Delta\mu_{\mathrm{L}}$. For this choice of parameters, the ground state critical boundaries are symmetric with respect to inversion of $\Delta\mu_{\mathrm{L}}$ from n-type to p-type gating, and reversal of the magnetic field direction. This also holds if $B_{\mathrm{L}} \neq B_{\mathrm{R}}$, as seen in Figure A.19c. The critical field required for a singlet-triplet transition in this case is limited by the smaller of the two Zeeman effects. In the fully asymmetric dimer, where additionally $U_{\mathrm{L}} \neq U_{\mathrm{R}}$, and $\mu_{\mathrm{R}} \neq U_{\mathrm{R}}/2$, the singlet state is more stable against one gating polarity. In Figure A.19d, since site R is only slightly n-type gated, $\Delta\mu_{\mathrm{L}}$ establishes the singly occupied states with $N = 1$ more readily than $N = 3$.

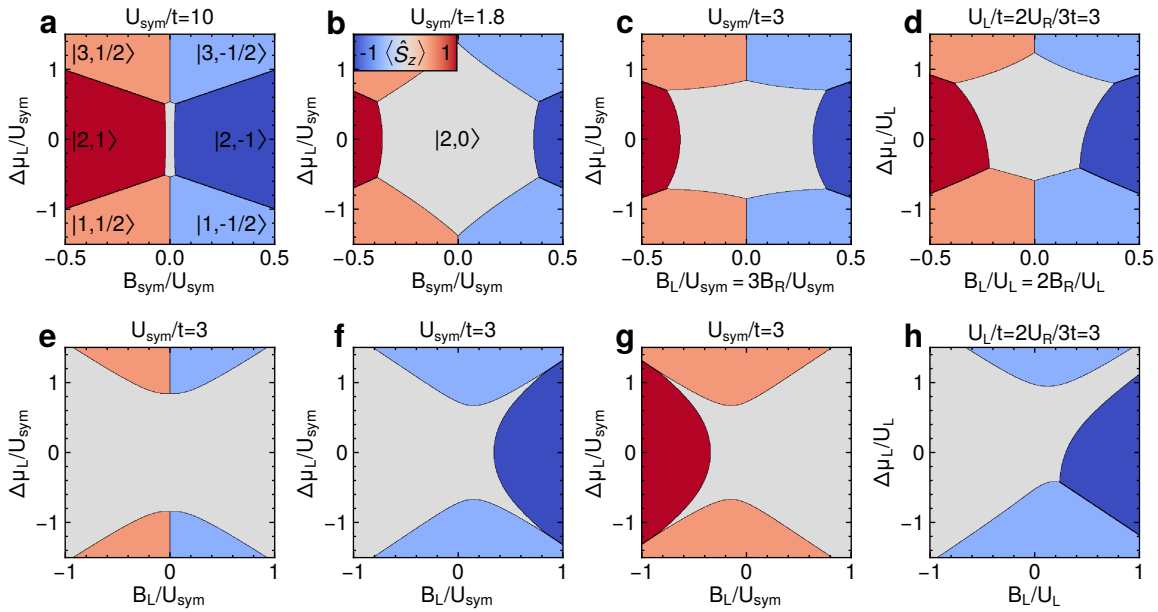

Figure A.19: Ground-state phase diagrams of the asymmetric Hubbard dimer. In the top row, B_L and B_R are scaled together. **(a-b)** Symmetric repulsion, symmetric fields and half-filling for two values of U_sym/t. **(c)** At $U_\mathrm{sym}/t = 3$ but with asymmetric fields $B_\mathrm{L}/B_\mathrm{R} = 3$. **(d)** The fully asymmetric case with $B_\mathrm{L}/B_\mathrm{R} = 2$, $U_\mathrm{L}/U_\mathrm{R} = 2/3$ and $\mu_\mathrm{R} = U_\mathrm{R}/6$. In the bottom row, B_R is constant value and B_L scaled independently. **(e)** $B_\mathrm{R} = 0$, **(f)** $B_\mathrm{R} = U_\mathrm{sym}/10$, **(g)** $B_\mathrm{R} = -U_\mathrm{sym}/10$. **(h)** as in **(d)** but with $B_\mathrm{R} = U_\mathrm{L}/10$.

If B_L is varied independently of B_R, the system can no longer adapt all possible ground states. For $B_\mathrm{R} = 0$, shown in Figure A.19e, the triplet configurations are absent, which derives from the asymptotic trend in Figure A.18a. Essentially, site R can always align antiferromagnetically to site L with no energy cost, independent of B_L. If B_R is non-zero, only one of the triplet state can be form: the one matching the sign of B_R. This is seen in Figure A.19f-g. The same holds for the doublet states $|1, \pm 1/2\rangle$ and $|3, \pm 1/2\rangle$.

We map the symmetric Hubbard dimer onto chiral graphene nanoribbons by estimating the effective repulsion parameter $U_\mathrm{sym}^\mathrm{eff}$ and hopping amplitude t_eff from tight-binding calculations of the π-electron system. Hybridization between symmetry-protected topological end states opens a gap whose magnitude decays exponentially with length L; we identify it as $2t_\mathrm{eff}$. The penalty for double occupancy of one SPTES by two electrons ψ_1 and ψ_2 is the Coulomb integral:[46]

$$U_\mathrm{sym}^\mathrm{eff} = \frac{e^2}{4\pi\epsilon_0} \int \frac{\psi_1(\mathbf{r}_1)^2 \psi_2(\mathbf{r}_2)^2}{||\mathbf{r}_1 - \mathbf{r}_2||} \mathrm{d}\mathbf{r}_1 \mathrm{d}\mathbf{r}_2 \approx U_\mathrm{H} \sum_i |\Psi_i|^4 \tag{A.16}$$

Where the integral is parameterized by the Hubbard parameter U_H, and the sum over the tight-binding wavefunction of the SPTES Ψ_i, which runs over all carbon sites i. This relies on the assumption that electron-electron repulsion does not significantly modify Ψ_i, i.e. SPTESs do not mix with edge-localized bands. This is fulfilled for $U_\mathrm{H} = 3\,\mathrm{eV}$, as shown in Figure 1.4. The obtained values are shown in Figure A.20, which can be used to analytically

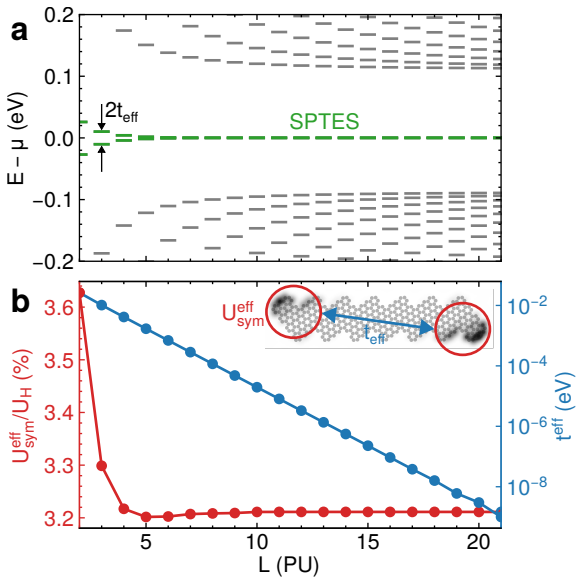

Figure A.20: Mapping chiral graphene nanoribbons to the Hubbard dimer. **(a)** Tight-binding spectrum as a function of the GNR length L. Note that the SPTESs hybridize significantly at $L < 5\,\mathrm{PU}$ to form a gap of $2t_{\mathrm{eff}}$. Its value is plotted logarithmically in **(b)**, together with the effective repulsion parameter $U^{\mathrm{eff}}_{\mathrm{sym}}$ obtained from the Coulomb integral over one SPTESs.

obtain $\Delta\mu^{\mathrm{c}}_{\mathrm{L}}$ from Equation (A.15) and $B^{\mathrm{c}}_{\mathrm{sym}}$ from Equation (A.13) in the discussed symmetric limits, or numerically for the fully asymmetric case $U_{\mathrm{H,L}} \neq U_{\mathrm{H,R}}$.

Notes

[1]In order to stabilize this state numerically, one has to apply a small gradient of on-site energies ε along the molecular axis. Here, the left terminus experiences a potential of −5 meV over the right terminus.

[2]The opposite process is thermally suppressed.

[3]Lateral manipulation of single atoms[313] is also possible by approaching the tip towards their side, and applying a pulse. In Figure 2.4c, this has occurred inadvertently, as the Ti atom, initially found on the bridge adsorption site, is transferred to the oxygen site.

[4]Strictly speaking, this is true only in the limit $U_{\mathrm{RF,J}} \gg k_{\mathrm{B}}T$.

[5]A strikingly similar effect with the same functional dependence arises in field-modulated NMR at kHz frequencies[314]

[6]We follow the treatment of Turco *et al.*[84], who determine the Kondo temperature as

$$1.542 k_{\mathrm{B}} T_{\mathrm{K}} = \sqrt{\sqrt{\Gamma^4/3 + \tau^2\Gamma^2/3 + 0.622\tau^4} - 0.711\tau^2 - 0.423\Gamma^2}$$

with $\tau = \pi k_{\mathrm{B}} T$, the temperature $T = 5\,\mathrm{K}$ in our setup, and $\Gamma = 2.542\Gamma_{\mathrm{F}}$ the temperature-broadened half-width determined here from the fit of Frota's lineshape[83] with its width parameter Γ_{F}.

Bibliography

1. Rosenberg, D. *et al.* npj Quantum Information 3, 1–5 (2017).
2. Hartnett, K. Quanta Magazine (2019).
3. De Leon, N. P. *et al.* Science 372, eabb2823 (2021).
4. Mohseni, M. *et al. How to Build a Quantum Supercomputer: Scaling from Hundreds to Millions of Qubits* arXiv: 2411.10406 [quant-ph]. Pre-published.
5. Leuenberger, M. N. *et al.* Nature 410, 789–793 (2001).
6. Martínez-Pérez, M. J. *et al.* Physical Review Letters 108, 247213 (2012).
7. Gaita-Ariño, A. *et al.* Nature Chemistry 11, 301–309 (4 2019).
8. Gatteschi, D. *et al.* Molecular Nanomagnets. *Mesoscopic Physics and Nanotechnology* **5.** 395 pp. (Oxford University Press, Oxford ; New York, 2006).
9. Morrillo, W. T. *et al.* Journal of the American Chemical Society 146, 25841–25851 (2024).
10. Godfrin, C. *et al.* Physical Review Letters 119, 187702 (2017).
11. Zhang, X. *et al.* Nature Chemistry 14, 59–65 (2022).
12. Kawaguchi, R. *et al.* Nano Letters 23, 213–219 (2023).
13. Kovarik, S. *et al.* Science 384, 1368–1373 (2024).
14. Huang, W. *et al. Quantum Spin-Engineering in On-Surface Molecular Ferrimagnets* arXiv: 2410.18563 [cond-mat]. Pre-published.
15. Sakurai, J. J. *et al.* Modern Quantum Mechanics 2nd edition. 550 pp. (Pearson, Boston, 2010).
16. Abragam, A. *et al.* Electron Paramagnetic Resonance of Transition Ions. 911 pp. (Oxford University Press, Oxford, 1970).
17. Slichter, C. P. Principles of Magnetic Resonance (red. Cardona, M. *et al.*) (Springer Berlin Heidelberg, Berlin, Heidelberg, 1990).
18. Stoll, S. *Spectral Simulations in Solid-State Electron Paramagnetic Resonance* PhD thesis (ETH Zürich, 2003).
19. Swart, M. Inorganica Chimica Acta 360, 179–189 (2007).
20. Prins, R. *et al.* The Journal of Chemical Physics 46, 1216–1217 (1967).
21. Jackson, T. A. *et al.* Organometallics 31, 8265–8274 (2012).
22. Ormaza, M. *et al.* Nano Letters 17, 1877–1882 (2017).
23. Gambardella, P. *et al.* Physical Review Letters 88, 047202 (2002).
24. Gambardella, P. *et al.* Science 300, 1130–1133 (2003).
25. Heinrich, A. J. *et al.* Science 306, 466–469 (2004).
26. Brune, H. *et al.* Surface Science 603, 1812–1830 (2009).
27. Baumann, S. *Investigation of the Unusual Magnetic Properties of Fe and Co on MgO with High Spatial, Energy and Temporal Resolution* PhD thesis (University Basel, Basel, 2015).
28. Yang, K. *et al.* Physical Review Letters 119 (2017).
29. Paul, W. *et al.* Nature Physics 13, 403–407 (2017).
30. Willke, P. *et al.* Science Advances 4 (2018).
31. Meier, F. *et al.* Science 320, 82–86 (2008).
32. Donati, F. *et al.* Physical Review Letters 113, 237201 (2014).
33. Donati, F. *et al.* Science 352, 318–321 (2016).
34. Donati, F. *et al.* Nano Letters 21, 8266–8273 (2021).

35. Donati, F. *et al.* Applied Physics Letters 119, 160503 (2021).
36. Wernsdorfer, W. *et al.* Science 284, 133–135 (1999).
37. Steinbrecher, M. *et al.* Physical Review B 103 (2021).
38. Farinacci, L. *et al.* Nano Letters 22, 8470–8474 (2022).
39. Kim, J. *et al.* Nano Letters 22, 9766–9772 (2022).
40. Castro Neto, A. H. *et al.* Reviews of Modern Physics 81, 109–162 (2009).
41. Nakada, K. *et al.,* 8 (1996).
42. Fujita, M. *et al.* Journal of the Physical Society of Japan 65, 1920–1923 (1996).
43. Fernández-Rossier, J. *et al.* Physical Review Letters 99, 177204 (2007).
44. Yazyev, O. V. Reports on Progress in Physics 73, 056501 (2010).
45. Yazyev, O. V. in *Basic Physics of Functionalized Graphite* (ed Esquinazi, P. D.) 1–24 (Springer International Publishing, Cham, 2016).
46. De Oteyza, D. G. *et al.* Journal of Physics: Condensed Matter 34, 443001 (2022).
47. Ovchinnikov, A. A. Theoretica chimica acta 47, 297–304 (1978).
48. Lieb, E. H. Physical Review Letters 62, 1201–1204 (1989).
49. Yazyev, O. V. *et al.* Physical Review B 84, 115406 (2011).
50. Li, J. *et al.* Nature Communications 12, 5538 (2021).
51. Söde, H. *et al.* Physical Review B 91, 045429 (2015).
52. Wang, S. *et al.* Nature Communications 7, 11507 (1 2016).
53. Cao, T. *et al.* Physical Review Letters 119, 076401 (2017).
54. Gröning, O. *et al.* Nature 560, 209–213 (2018).
55. Rizzo, D. *et al.* Nature 560, 204–208 (2018).
56. Hancock, Y. *et al.* Physical Review B 81, 245402 (2010).
57. Jacob, D. *et al.* Physical Review B 106, 205405 (2022).
58. Krane, N. *et al.* Nano Letters 23, 9353–9359 (2023).
59. Henriques, J. C. G. *et al.* Physical Review B 108, 155423 (2023).
60. Wuhl, S. S. *π-Magnetism and Quantum Transport in Graphene-Based Nanostructures* PhD thesis (University of the Basque Country, Donostia-San Sebastián, Spain, 2022).
61. Li, J. *et al.* Nature Communications 10, 200 (2019).
62. Li, J. *et al.* Physical Review Letters 124, 177201 (2020).
63. Sanz, S. *et al.* Journal of Physics: Condensed Matter 35, 374001 (2023).
64. Sanz Wuhl, S. *et al. Hubbard: V0.1.0* version v0.1.0. Zenodo, 2021.
65. Fernández Torrente, I. *et al.* Journal of Physics: Condensed Matter 20, 184001 (2008).
66. Crispin, X. *et al.* Journal of the American Chemical Society 124, 8131–8141 (2002).
67. Lu, X. *et al.* Physical Review B 70, 115418 (2004).
68. Repp, J. *et al.* Physical Review Letters 94, 026803 (2005).
69. Wang, T. *et al.* Journal of the American Chemical Society 144, 4522–4529 (2022).
70. Willenbockel, M. *et al.* Physical Chemistry Chemical Physics 17, 1530–1548 (2015).
71. Kondo, J. Progress of Theoretical Physics 32, 37–49 (1964).
72. Appelbaum, J. Physical Review Letters 17, 91–95 (1966).
73. Anderson, P. W. Physical Review Letters 17, 95–97 (1966).
74. Appelbaum, J. A. *et al.* Physical Review Letters 19, 906–908 (1967).
75. Ternes, M. New Journal of Physics 17, 063016 (2015).
76. Ternes, M. Progress in Surface Science 92, 83–115 (2017).
77. Suhl, H. Physical Review 138, A515–A523 (2A 1965).
78. Abrikosov, A. A. Physics Physique Fizika 2, 5–20 (1965).
79. Wilson, K. G. Reviews of Modern Physics 47, 773–840 (1975).
80. Hewson, A. C. The Kondo Problem to Heavy Fermions (Cambridge University Press, Cambridge, 1993).
81. Phillips, P. Advanced Solid State Physics 2nd ed. (Cambridge University Press, 2012).
82. Grosso, G. *et al.* Solid State Physics 2. ed. 857 pp. (Elsevier, Acad. Press, Amsterdam, 2014).
83. Frota, H. O. Physical Review B 45, 1096–1099 (1992).
84. Turco, E. *et al. Demonstrating Kondo Behavior by Temperature-Dependent Scanning Tunneling Spectroscopy* arXiv: `2310.09326 [cond-mat]`. Pre-published.

85. Costi, T. A. Physical Review Letters 85, 1504–1507 (2000).
86. Voigtländer, B. Scanning Probe Microscopy: Atomic Force Microscopy and Scanning Tunneling Microscopy (Springer Berlin Heidelberg, Berlin, Heidelberg, 2015).
87. Chen, C. J. Introduction to Scanning Tunneling Microscopy 3rd ed. (Oxford University Press, 2021).
88. Stipe, B. C. *et al.* Science 280, 1732–1735 (1998).
89. Appelbaum, J. A. Physical Review 154, 633–643 (1967).
90. Appelbaum, J. A. *et al.* Physical Review 160, 554–561 (1967).
91. Loth, S. *et al.* New Journal of Physics 12, 125021 (2010).
92. Wiesendanger, R. *et al.* Physical Review Letters 65, 247–250 (1990).
93. Wiesendanger, R. Reviews of Modern Physics 81, 1495–1550 (2009).
94. Loth, S. *et al.* Nature Physics 6, 340–344 (5 2010).
95. Rolf-Pissarczyk, S. *et al.* Physical Review Letters 119, 217201 (2017).
96. Kreuzer, H. J. Nonequilibrium Thermodynamics and Its Statistical Foundations. xx, 438 (Clarendon Press, Oxford, New York, 1981).
97. Delgado, F. *et al.* Progress in Surface Science 92, 40–82 (2017).
98. Natterer, F. D. *et al.* Nature 543, 226+ (2017).
99. Loss, D. *et al.* Physical Review A 57, 120–126 (1998).
100. Szátay, C. *et al.* Concepts in Magnetic Resonance 3, 161–170 (1991).
101. Baumann, S. *et al.* Science 350, 417–420 (2015).
102. Delgado, F. *et al.* Progress in Surface Science, 100625 (2021).
103. Chen, Y. *et al.* Advanced Materials n/a, 2107534.
104. Wang, Y. *et al.* Science 382, 87–92 (2023).
105. Budakian, R. *et al.* Nanotechnology 35, 412001 (2024).
106. Willke, P. *et al.* Science 362, 336+ (2018).
107. Bae, Y. *et al.* Science Advances 4 (2018).
108. Yang, K. *et al.* Physical Review Letters 122 (2019).
109. Willke, P. *et al.* Nature Physics 15, 1005–1010 (2019).
110. Yang, K. *et al.* Science 366, 509–512 (2019).
111. Van Weerdenburg, W. M. J. *et al.* Review of Scientific Instruments 92, 033906 (2021).
112. Veldman, L. M. *et al.* Science 372, 964–968 (2021).
113. Seifert, T. S. *et al.* Physical Review Research 3, 043185 (2021).
114. Phark, S.-h. *et al.* ACS Nano 17, 14144–14151 (2023).
115. Phark, S.-h. *et al.* Advanced Science 10, 2302033 (2023).
116. Veldman, L. M. *et al. Coherent Spin Dynamics between Electron and Nucleus within a Single Atom* arXiv: 2309.03749 [cond-mat]. Pre-published.
117. Zhang, X. *et al.* ACS Nano 17, 16935–16942 (2023).
118. Bui, H. T. *et al.* ACS Nano 18, 12187–12193 (2024).
119. Reale, S. *et al.* Nature Communications 15, 5289 (2024).
120. Seifert, T. S. *et al.* Science Advances 6, eabc5511 (2020).
121. Berggren, P. *et al.* Scientific Reports 6 (2016).
122. Dalidchik, F. I. *et al.* JETP LETTERS 105, 314–318 (2017).
123. Lado, J. L. *et al.* Physical Review B 96 (2017).
124. Shakirov, A. M. *et al.* Physical Review B 99 (2019).
125. Gálvez, J. R. *et al.* Physical Review B 100, 035411 (2019).
126. Ferron, A. *et al.* Physical Review Research 1 (2019).
127. Reina-Gálvez, J. *et al. From Non-Equilibrium Green's Functions to Floquet Quantum Master Equations: An Application to All-Electrical Electron Spin Resonance* 2021. arXiv: 2108.01011 [cond-mat].
128. Ast, C. R. *et al.* Physical Review Research 6, 023126 (2024).
129. Yan, S. *et al.* Nature Nanotechnology 10, 40–45 (1 2015).
130. Choi, D.-J. *et al.* Nano Letters 16, 6298–6302 (2016).
131. Sellies, L. *et al.* Nature 624, 64–68 (2023).
132. Herve, M. *et al.* Nanomaterials 9 (2019).
133. Kim, J. *et al.* Physical Review B 104, 174408 (2021).
134. Giessibl, F. J. Review of Scientific Instruments 90, 011101 (2019).

135. Gross, L. *et al.* Angewandte Chemie-International Edition 57, 3888–3908 (2018).
136. Gross, L. *et al.* Science 324, 1428–1431 (2009).
137. Lüth, H. Solid Surfaces, Interfaces and Thin Films 6th edition (Springer International Pub, New York, NY, 2015).
138. Smentkowski, V. S. Progress in Surface Science 64, 1–58 (2000).
139. Zangwill, A. Physics at Surfaces (Cambridge University Press, Cambridge, 1988).
140. Corso, M. *et al.* ACS Nano 4, 1603–1611 (2010).
141. Schintke, S. *et al.* Physical Review Letters 87, 276801 (2001).
142. Valeri, S. *et al.* Physical Review B 65, 245410 (2002).
143. Gallagher, M. C. *et al.* Thin Solid Films 445, 90–95 (2003).
144. Schintke, S. *et al.* Journal of Physics: Condensed Matter 16, R49–R81 (2004).
145. Heyde, M. *et al.* Applied Physics Letters 87, 083104 (2005).
146. Sterrer, M. *et al.* The Journal of Physical Chemistry B 110, 46–49 (2006).
147. Yulikov, M. *et al.* Physical Review Letters 96, 146804 (2006).
148. Sterrer, M. *et al.* Physical Review Letters 98, 096107 (2007).
149. Sterrer, M. *et al.* Physical Review Letters 98, 206103 (2007).
150. Ouvrard, A. *et al.* The Journal of Physical Chemistry C 115, 8034–8041 (2011).
151. Pal, J. *et al.* The Journal of Physical Chemistry C 118, 26091–26102 (2014).
152. Baumann, S. *et al.* ACS Nano 8, 1739–1744 (2014).
153. Pal, J. *et al.* Physical Review Letters 112, 126102 (2014).
154. Fernandes, E. *et al.* Physical Review B 96 (2017).
155. Xu, C. *et al.* Journal of Physical Chemistry C 123, 19619–19624 (2019).
156. Domínguez-Celorrio, A. *On-Surface Synthesis of Functional Organic Nanostructures* PhD thesis (University of Zaragoza, 2022).
157. Brune, H. Annalen der Physik 521, 675–698 (2009).
158. Zhang, L. *et al.* Review of Scientific Instruments 82, 103702 (2011).
159. Vieyra-Eusebio, M. T. *et al.* Journal of Chemical & Engineering Data 56, 5008–5018 (2011).
160. Garnier, L. *et al.* Nano Letters (2020).
161. Cai, J. *et al.* Nature 466, 470–473 (7305 2010).
162. Eigler, D. M. *et al.* Nature 344, 524–526 (6266 1990).
163. Morgenstern, K. *et al.* physica status solidi (b) 250, 1671–1751 (2013).
164. Pascual, J. I. *et al.* Nature 423, 525–528 (2003).
165. Jacobse, P. H. *et al.* ACS Nano 12, 7048–7056 (2018).
166. Esat, T. *et al. Electron Spin Secluded inside a Bottom-up Assembled Standing Metal-Molecule Nanostructure* arXiv: `2301.11762 [cond-mat]`. Pre-published.
167. Schwenk, J. *et al.* The Review of scientific instruments 91, 071101 (2020).
168. Hervé, M. *et al.* Applied Physics Letters 107, 093101 (2015).
169. Peter, M. *Towards Magnetic Resonance in Scanning Tunneling Microscopy Using Heterodyne Detection* PhD thesis (Karlsruhe Institute for Technology, Karlsruhe, 2015).
170. Xu, C. *et al.* Review of Scientific Instruments 90, 103706 (2019).
171. Natterer, F. D. *et al.* Review of Scientific Instruments 90, 013706 (2019).
172. Friedlein, J. *et al.* Review of Scientific Instruments 90 (2019).
173. Peters, O. *Transport Processes through Superconducting Junctions at the Atomic Scale: Implementation of a High-Frequency Circuit into a Scanning Tunneling Microscope* PhD thesis (Berlin, 2021).
174. Hwang, J. *et al.* Review of Scientific Instruments 93, 093703 (2022).
175. Pozar, D. M. Microwave Engineering 4th ed. 732 pp. (Wiley, Hoboken, NJ, 2012).
176. Peters, O. *et al.* Nature Physics 16, 1222–1226 (2020).
177. Kushino, A. *et al.* Journal of Low Temperature Physics 151, 650–654 (2008).
178. Uher, C. Journal of Superconductivity 3, 337–389 (1990).
179. Paul, W. *et al.* Review of Scientific Instruments 87 (2016).
180. Balanis, C. A. Antenna Theory: Analysis and Design Fourth edition. 1072 pp. (Wiley, Hoboken, New Jersey, 2016).
181. Tinkham, M. Introduction to Superconductivity 2. ed. 454 pp. (Dover Publ, Mineola, NY, 2004).
182. Physics and Applications of the Josephson Effect (eds Barone, A. *et al.*) (Wiley, New York, 1982).

183. Likharev, K. K. Dynamics of Josephson Junctions and Circuits. 614 pp. (Gordon and Breach Science Publishers, New York, 1986).
184. Rowell, J. M. *et al.* Physical Review 137, A907–A916 (3A 1965).
185. Ruby, M. *et al.* Physical Review Letters 114, 157001 (2015).
186. Giaever, I. Physical Review Letters 5, 464–466 (1960).
187. Tien, P. K. *et al.* Physical Review 129, 647–651 (1963).
188. Roychowdhury, A. *et al.* Physical Review Applied 4, 034011 (2015).
189. Ast, C. R. *et al.* Nature Communications 7, 13009 (1 2016).
190. Kot, P. *et al.* Physical Review B 101, 134507 (2020).
191. Swartzentruber, B. S. Physical Review Letters 76, 459–462 (1996).
192. Kovarik, S. *et al.* Nano Letters 22, 4176–4181 (2022).
193. Corso, M. *et al.* Nanomaterials 11, 3303 (12 2021).
194. Domínguez-Celorrio, A. *et al. Engineering Open-Shell Extended Edge States in Chiral Graphene Nanoribbons on MgO* arXiv: 2406.03927 [cond-mat, physics:quant-ph]. Pre-published.
195. Que, Y. *et al.* The Journal of Physical Chemistry Letters 11, 4107–4112 (2020).
196. Que, Y. *et al.* The Journal of Physical Chemistry Letters 11, 5044–5050 (2020).
197. Brede, J. *et al.* Nature Communications 14, 6677 (2023).
198. Martínez-Blanco, J. *et al.* Nature Physics 11, 640–644 (2015).
199. Mohn, F. *et al.* Nature Nanotechnology 7, 227–231 (2012).
200. Schuler, B. *et al.* Nano Letters 14, 3342–3346 (2014).
201. Albrecht, F. *et al.* Physical Review Letters 115, 076101 (2015).
202. Jelínek, P. Journal of Physics: Condensed Matter 29, 343002 (2017).
203. Nistor, C. *et al.* Physical Review B 92, 184402 (2015).
204. Ormaza, M. *et al.* Nano Letters 16, 4230–4235 (2016).
205. Bazarnik, M. *et al.* Physical Review B 99, 174419 (2019).
206. Heersche, H. B. *et al.* Physical Review Letters 96, 017205 (2006).
207. Spinelli, A. *et al.* Nature Communications 6, 10046 (2015).
208. Loth, S. *et al.* Science 335, 196–199 (2012).
209. Cheng, Y.-C. *et al.* Physica B+C 85, 299–304 (1976).
210. Ortiz, R. *et al.* Physical Review B 97, 195425 (2018).
211. Ormaza, M. *et al.* Nature Communications 8, 1974 (1 2017).
212. Verlhac, B. *et al.* Science 366, 623–627 (2019).
213. Bachellier, N. *et al.* Nature Communications 11, 1619 (1 2020).
214. Ormaza, M. *et al.* Nano Letters 16, 588–593 (2016).
215. Czap, G. *et al.* Science 364, 670+ (2019).
216. Song, S. *et al. Designer Magnetic Topological Graphene Nanoribbons* arXiv: 2204.12880 [cond-mat]. Pre-published.
217. Zhuang, Q. *et al.* Chemical Physics Letters 830, 140813 (2023).
218. Aguirre, A. *et al.* Advanced Materials, 2402723 (2024).
219. Song, S. *et al.* Nature Chemistry 16, 938–944 (2024).
220. Fétida, A. *et al.* ACS Nano 18, 13829–13835 (2024).
221. Hapala, P. *et al.* Physical Review B 90, 085421 (2014).
222. Parks, J. J. *et al.* Science 328, 1370–1373 (2010).
223. Drost, R. *et al.* Physical Review Letters 131, 086701 (2023).
224. Feenstra, R. M. *et al.* in *Physics of Solid Surfaces* (eds Chiarotti, G. *et al.*) 15–15 (Springer Berlin Heidelberg, Berlin, Heidelberg, 2015).
225. Chikazumi, S. *et al.* Physics of Ferromagnetism (Oxford University Press, 1997).
226. Kashuba, A. B. *et al.* Physical Review B 48, 10335–10344 (1993).
227. Cavallin, A. *et al.* Physical Review B 90, 235419 (2014).
228. Mohr, M. *et al.* Physical Review B 101, 075414 (2020).
229. Kröger, J. *et al.* Journal of Physics: Condensed Matter 20, 223001 (2008).
230. Jacob, D. Physical Review B 108, L161109 (2023).
231. Kögler, M. *et al.* Nano Letters 24, 14355–14362 (2024).
232. Zuo, L. *et al.* The Journal of Physical Chemistry Letters 13, 11262–11270 (2022).

233. Liu, X. *et al.* The Journal of Physical Chemistry C 126, 4577–4583 (2022).
234. Blesio, G. G. *et al.* SciPost Physics 14, 042 (2023).
235. Žitko, R. *et al.* Physical Review B 78, 224404 (2008).
236. Otte, A. F. *et al.* Nature Physics 4, 847–850 (11 2008).
237. Oberg, J. C. *et al.* Nature Nanotechnology 9, 64–68 (2014).
238. Jacobson, P. *et al.* Nature Communications 6, 8536 (2015).
239. Roch, N. *et al.* Physical Review Letters 103, 197202 (2009).
240. Blesio, G. G. *et al.* Physical Review B 100, 075434 (2019).
241. Van Der Wiel, W. G. *et al.* Physical Review Letters 88, 126803 (2002).
242. Žitko, R. *et al.* New Journal of Physics 11, 053003 (2009).
243. Weymann, I. *et al.* Physical Review B 81, 115445 (2010).
244. Misiorny, M. *et al.* Physical Review B 86, 245415 (2012).
245. Pasupathy, A. N. *et al.* Science 306, 86–89 (2004).
246. Hamaya, K. *et al.* Applied Physics Letters 91, 232105 (2007).
247. Hauptmann, J. R. *et al.* Nature Physics 4, 373–376 (2008).
248. Delgado, F. *et al.* Surface Science 630, 337–342 (2014).
249. Rajasekharan, M. V. *et al.* Journal of the American Chemical Society 105, 7516–7522 (1983).
250. Esat, T. *et al.* Nature Nanotechnology 19, 1466–1471 (2024).
251. Münzfeld, L. *et al.* Nature Communications 10, 3135 (2019).
252. Dearman, H. H. *et al.* The Journal of Chemical Physics 34, 696–697 (1961).
253. Camarasa-Gómez, M. *et al.* The Journal of Physical Chemistry Letters 15, 5747–5753 (2024).
254. Braun, K.-F. *et al.* Physical Review Letters 96, 246102 (2006).
255. Llinas, J. P. *et al.* Nature Communications 8, 633 (2017).
256. Deniz, O. *et al.* Nano Letters 17, 2197–2203 (2017).
257. Kinikar, A. *et al.* ACS Nano 18, 16622–16631 (2024).
258. Ruffieux, P. *et al.* Nature 531, 489–492 (2016).
259. Kolmer, M. *et al.* Science 369, 571–575 (2020).
260. Steurer, W. *et al.* Applied Physics Letters 104, 231606 (2014).
261. Repp, J. *et al.* Physical Review Letters 95, 225503 (2005).
262. Krane, N. *et al.* ACS Nano 12, 11698–11703 (2018).
263. Krane, N. *et al.* Physical Review B 100, 035410 (2019).
264. Reecht, G. *et al.* Physical Review Letters 124, 116804 (2020).
265. Reecht, G. *et al.* ACS Nano 13, 7031–7035 (2019).
266. Zheng, D. *et al.* Physical Review B 104, 085430 (2021).
267. Franke, K. J. *et al.* Journal of Physics: Condensed Matter 24, 394002 (2012).
268. Kaiser, K. *et al.* Nature Communications 14, 4988 (2023).
269. Wu, S. W. *et al.* Physical Review B 77, 205430 (2008).
270. Repp, J. *et al.* Chimia International Journal for Chemistry 64, 370–375 (2010).
271. Derry, G. N. *et al.* Journal of Vacuum Science & Technology A 33, 060801 (2015).
272. Giordano, L. *et al.* Physical Review B 73, 045414 (2006).
273. Prada, S. *et al.* Physical Review B 78, 235423 (2008).
274. Hollerer, M. *et al.* ACS Nano 11, 6252–6260 (2017).
275. Takahashi, T. *et al.* Physical Review B 32, 8317–8324 (1985).
276. Yan, R. *et al.* Applied Physics Letters 101, 022105 (2012).
277. Merino-Díez, N. *et al.* ACS Nano 11, 11661–11668 (2017).
278. Nazin, G. V. *et al.* Proceedings of the National Academy of Sciences 102, 8832–8837 (2005).
279. Pathria, R. K. Statistical Mechanics (Butterworth-Heinemann, Oxford; Boston, 1996).
280. Hurdax, P. *et al.* Advanced Materials Interfaces 7, 2000592 (2020).
281. Krupka, J. *et al.* IEEE Transactions on Microwave Theory and Techniques 42, 1886–1890 (1994).
282. Imai-Imada, M. *et al.* Physical Review B 98, 201403 (2018).
283. Caplins, B. W. *et al.* The Journal of Physical Chemistry Letters 5, 1679–1684 (2014).
284. Kamiński, W. *et al.* The Journal of Physical Chemistry C 126, 16767–16776 (2022).
285. Jaouen, T. *et al.* Physical Review B 90, 125433 (2014).
286. Wehrle, B. *et al.* Chemical Physics 136, 223–247 (1989).

287. Kügel, J. *et al.* The Journal of Physical Chemistry C 121, 28204–28210 (2017).
288. Rosławska, A. *et al.* Nature Nanotechnology, 1–6 (2024).
289. Grewal, A. *et al.* ACS Nano 18, 12158–12167 (2024).
290. Tsukahara, N. *et al.* Physical Review Letters 102, 167203 (2009).
291. Minamitani, E. *et al.* Physical Review Letters 109, 086602 (2012).
292. Rubio-Verdú, C. *et al.* Communications Physics 1, 15 (2018).
293. Vaxevani, K. *et al.* Nano Letters 22, 6075–6082 (2022).
294. Trivini, S. *et al.* Physical Review Letters 130, 136004 (2023).
295. Mugarza, A. *et al.* Physical Review B 85, 155437 (2012).
296. Harris, R. K. *et al.* Pure and Applied Chemistry 73, 1795–1818 (2001).
297. Vincent, R. *et al.* Nature 488, 357–360 (2012).
298. Thiele, S. *et al.* Science 344, 1135–1138 (2014).
299. Yang, K. *et al.* Nature Nanotechnology 13, 1120+ (2018).
300. Stolte, E. W. *et al. Single-Shot Readout of the Nuclear Spin of an on-Surface Atom* arXiv: 2410.08704. Pre-published.
301. Fernández de Fuentes, I. *et al.* Nature Communications 15, 1380 (2024).
302. Pla, J. J. *et al.* Nature 496, 334–338 (2013).
303. Solomon, I. Physical Review 99, 559–565 (1955).
304. Steinbrecher, M. *et al. Quantifying the Interplay between Fine Structure and Geometry of an Individual Molecule on a Surface* 2020. arXiv: 2007.01928.
305. Stone, N. J. Atomic Data and Nuclear Data Tables 90, 75–176 (2005).
306. Hieulle, J. *et al.* Angewandte Chemie International Edition 60, 25224–25229 (2021).
307. Zhao, C. *et al.* Physical Review Letters 132, 046201 (2024).
308. Sengupta, S. *et al.* Physical Review B 107, 224433 (2023).
309. Pivetta, M. *et al.* Physical Review X 10, 031054 (2020).
310. Hsieh, M.-F. *et al.* The Journal of Chemical Physics 131, 174709 (2009).
311. Matlak, M. *et al.* Annalen der Physik 515, 304–319 (2003).
312. Jafari, S. A. Iranian Journal of Physics Research 8, 116 (2008).
313. Stroscio, J. A. *et al.* Science 306, 242–247 (2004).
314. Miyagawa, I. *et al.* Journal of Magnetic Resonance (1969) 25, 183–195 (1977).